Switchable molecules on metallic surfaces studied by core-level spectroscopies

Im Fachbereich Physik der Freien Universität Berlin
eingereichte Dissertation von

Marten Piantek

Berlin 2009

Erstgutachter: Prof. Dr. Wolfgang Kuch
Zweitgutachter: Prof. Dr. José Ignacio Pascual

Tag der mündlichen Prüfung:
27. Januar 2010

Abstract

The scope of this work is the investigation of the interactions that appear in molecular switches on noble metal surfaces. The adsorption of two different types of switching molecules is studied by means of near edge X-ray absorption fine structure (NEXAFS) and X-ray photoelectron spectroscopy (XPS). Samples of molecular powders and evaporated molecular multilayers are used as references in which the molecules are decoupled from the surface. The interpretation of the measured data is supported by quantum-chemical calculations based on density-functional theory (DFT), resulting in a deep understanding of the interaction mechanisms.

In the first part of this work dimetacyano azobenzene and dimetacarboxymethylester azobenzene are chosen as simple model systems representing the class of conformal switches. These two compounds exhibit the same adsorption behavior and provide complementary information about the adsorption state. Au(111) and Cu(001) are used as substrates with different surface reactivities. On Au(111) at room temperature, azobenzene physisorbs flat in its *trans* configuration up to a saturation coverage of one monolayer, while the electronic structure of the adsorbate resembles the one calculated for the free molecule.

In contrast, on Cu(001) we find that the substrate temperature and the molecule coverage have an influence on the adsorption state. Below half a monolayer evaporated on Cu(001) at 150 K, the majority of azobenzene molecules are found to be in the same physisorbed state as on Au(111). After annealing the substrate above 250 K most of the molecules chemisorb via their azobenzene center, where the frontier orbitals at the azo bridge rehybridize with the substrate orbitals. This interaction forces the molecule to a butterfly-like bent molecular geometry in which the outer aromatic groups are tilted out of the surface plane. In this conformation the lone-pair electrons can participate in the chemical binding, leading to a higher stabilization of the bent structure. The structural reorientation is accompanied by the deoccupation of the bonding and the occupation of the antibonding molecular orbital, which

is described by the Dewar-Chatt-Duncanson model. At higher coverages the increased intermolecular interaction provokes a larger tilt, which increases the stronger lone-pair – surface interactions and finally leads to the dissociation at the central N–N azo bond.

The second part examines the adsorption of nitro-spiropyran (SP) as a member of the class of ring-opening/ring-closing switches in multi- and monolayers on Au(111). In multilayered films, the SP molecules order in a crystalline structure. UV irradiation causes half of the amount of molecules to undergo the ring-opening reaction. The resulting merocyanine (MC) is stabilized in the crystalline confinement such that a back reaction is not possible. For monolayer coverages, the molecule adsorbs on the substrate at 150 K with its nitro moiety flat on the surface. Annealing the substrate to 330 K provokes the ring-opening reaction. The resulting planar merocyanine molecule lies flat on the surface arranged in dimers that are liked by hydrogen bonds. The latter stabilize the ring-opened form and prevent the back reaction.

Kurzfassung

Ziel dieser Arbeit ist es, die Wechselwirkungen molekularer Schalter auf und mit verschiedenen Edelmetalloberflächen zu untersuchen. Zu diesem Zweck wird das unterschiedliche Adsorptionsverhalten von zwei Typen schaltbarer Moleküle mit Hilfe von Röntgen-Nahkanten-Absorptionsspektroskopie (NEXAFS) und Röntgen-Photoelektronenspektroskopie (XPS) charakterisiert. Proben der Moleküle in Pulverform und adsorbiert in Multilagen dienen als Referenz zu den an die Oberfläche gekoppelten Adsorbaten. Quantenchemische Berechnungen auf Basis von Dichtefunktionaltheorie (DFT) ermöglich dabei eine Interpretation der experimentellen Daten in Hinsicht auf ein grundlegendes Verständnis der auftreteneden Wechselwirkungen.

Im ersten Teil der Arbeit werden Dimetacyano- and Dimetacarboxymethylesterazobenzol als prototypische Vertreter der Klasse konformeller Schalter untersucht. Beide Verbindingen zeigen dasselbe Adsorptionsverhalten und liefern dennoch unterschiedliche, sich ergänzende Informationen über ihren chemischen Zustand auf der Oberfläche. Au(111) und Cu(001) dienen als Oberflächen mit unterschiedlicher Reaktivität. Die Azobenzole physisorbieren auf Au(111) bei Raumtemperatur, wobei die Moleküle in ihrer planaren *trans*-Form parallel zur Oberfläche ausgerichtet sind.

Im Gegensatz dazu ist ein Teil der Moleküle auf Cu(001) für Bedeckungen unterhalb einer halben Monolage schon bei Temperaturen von 150 K chemisorbiert. Oberhalb von 250 K ist die Chemisorption der gesamten Submonolage annähernd vollständig abgeschlossen. In diesem Zustand rehybridisieren die π-Orbitale der Azo-Brücke mit denen des Substrats. Diese Wechselwirkung verursacht eine leichte Deformation der planaren Struktur des *trans*-Azobenzols, bei der sich die äußeren aromatischen Einheiten von der Oberfläche wegbiegen. In dieser Geometrie können sich die freien Elektronenpaare der Stickstoffatome an der Bindung zum Substrat beteiligen, was zu einer erhöhten Stabilität der Struktur führt. Die Ausbildung der Bindungen zur Oberfläche wird begleitet von einer teilweisen Entvölkerung des bindenden π-Orbitals und einer teilweisen Besetzung des antibindenden π^*-Orbitals, so wie es im Rahmen des

Dewar-Chatt-Duncanson-Modells beschrieben wird. Für höhere Bedeckungen nahe einer Monolage nehmen die zwischenmolekularen Wechselwirkungen an Bedeutung zu und bewirken eine noch stärkere Verbiegung der adsorbierten Moleküle. Dies führt zu einer teilweisen Dissoziation der Adsorbatmoleküle.

Der zweite Teil der Arbeit behandelt die Adsorption von Nitro-Spiropyran (SP), einem Mitglied der Klasse der Ringöffnungs-/Ringschlussschalter, in Multi- und Monolagen auf Au(111). In Multilagen ordnen sich die SP-Moleküle zu einkristallinen Strukturen. Die Beleuchtung dieser Ensembles führt bei etwa der Hälfte der Moleküle zur Ringöffnung. Das entstandene Merocyanin ist so in den Kristall eingebunden, dass eine Rückreaktion nicht möglich ist. Auch hier kann ein temperaturabhängiges Verhalten beobachtet werden. Nach der Adsorption auf einer Au(111)-Oberfläche bei 150 K ist die Nitrogruppe des Moleküls parallel zur Oberfläche orientiert. Durch Erhöhung der Substrattemperatur auf 330 K öffnet sich der Pyranring und das resultierende planare Merocyanin adsorbiert flach auf der Oberfläche. Dabei formen sich Dimere, die durch Wasserstoffbrücken stabilisiert sind. Letzteres ist unter anderem verantwortlich für die Unterdrückung der entgegengesetzten Ringschlussreaktion.

Contents

Chapter 1

Introduction

The creation of surfaces with well-defined properties has always been one of the most important issues in materials science and technology. The possibility, *e.g.*, to tune at will properties such as the surfaces reactivity has an obvious impact on the development of anticorrosive coatings or catalyzer technologies. Beyond this scope, surfaces with tailored physical properties have been created in modern applications, like photovoltaic cells, self-cleaning surfaces based on the Lotus effect [1], or wavelength-selective mirrors. The development of those exotic macroscopic properties demands more and more often the modification of the surface at the nano- and subnanometer scales requiring a material structuring in the range of the size of atoms and molecules. The magnetic bit that represents the smallest information unit on a hard disk can occupy the area of about 1000 nm^2 [2]. Transistors that are embedded in a novel processor architecture on a silicon wafer have gate lengths of about 30 nm [3]. In view of future technologies, the question arises about methods that can be used in the generation of such structures of decreasing size. Current technologies are mainly based on so-called *top-down* techniques. In this case the structure is written into a material matrix that is much bigger than the resulting elementary structures, as is the case for lithographic methods. The lateral resolution of these techniques is limited by the wavelength of the radiation that is used in the lithography.

A different attempt uses the self-assembling and -organizing properties of atoms and molecules on surfaces. This principle is called *bottom-up*, since the structures are produced by the adsorption of molecular building blocks. In this case, the size of the resulting structures is only limited by the size of the building blocks. These molecular building blocks are usually produced by chemical synthesis. In principle, this method offers the same or even higher flexibility in producing novel functionalities than found in biologic systems.

Those functionalities can be further entailed from the molecular building block to the structure, and thus to the surface.

The class of organic compounds provides an enormous variety of functionalities that can be applied to surfaces. Simple microscopic features like hydrophilic or hydrophobic behavior, aromaticity, or electron transfer reactions result in macroscopic phenomena like wettability, (semi)conductivity, and electroluminescence. In particular the family of switchable molecules offers the possibility to reversibly control these properties by external inducements like photons, electrons, or protons. The controllable reversible changes might include variations of conformation and chemical bond configurations, leading to different so-called isomeric states. This allows the post-preparative control of the surface properties. The implementation of those functionalities into surface structures as inhibit properties of the molecular building blocks is only possible in the absence of adsorbate–surface interactions, wich might disturb the switching mechanism. Thus a common attempt is to decouple the molecular switch from the surface by spacer groups. This was realized in self-assembled monolayers (SAMs) [4, 5] or by attaching bulky rest groups that keep the functional unit at a distance from the surface [6–9].

The modification of metallic surfaces might be important, considering its role as a conductive interface. Here, requests about the molecular state could be addressed electronically. This is a preferable method, since competing techniques, like optical read-out, are restricted in resolution by the diffraction limit. In contrast, the direct electric contact to single molecules has been realized in the case of tips of scanning tunneling microscopes (STM), and at metallic break junctions [10]. In this sense the direct adsorption of molecular switches on metallic surfaces is an interesting field in the ongoing development of *bottom-up* technologies.

It was recently shown that molecular switches can preserve their functionality in the presence of metallic ions in solution [11], and even directly adsorbed on a metallic Au(111) surface [12]. However, it was demonstrated that only a slight variation in chemical structure can lead to the suppression of the isomerization process on the surface [13]. Obviously, the chemical and electronic adsorbate–substrate interactions play an important role and are a key aspect in understanding the mechanisms that influence the isomerization process. An example is the optically induced isomerization on metallic surfaces. It was demonstrated that the excited molecular states can be quenched due to adsorbate–dipole – (induced)-metallic-dipole coupling [14]. In this case, the excitation energy possibly dissipates into the substrate before the isomerization process is initiated. However, the dipole coupling strongly depends on

the orientation of the adsorbate dipole on the surface, such that an optical switching is still possible for certain adsorbate orientations. Further influences might originate from different chemical adsorbate-substrate interactions like ionic, coordinative, and covalent bond formation. The presence of the latter has been demonstrated by using a scanning tunneling microscope (STM) tip to switch a single *trans* azobenzene molecule on a Cu(001) surface at 5 K, where the resulting *cis* isomer was stabilized by chemisorption to the substrate, preventing the reverse transformation [15].

While most of the related research on switchable molecules adsorbed at metallic surfaces has been performed by STM [6, 7, 9, 12, 13, 15–18], the present study provides complementary information that leads to a more detailed picture of the involved adsorption mechanisms. In this work angle-dependent near edge X-ray absorption fine structure (NEXAFS) is used to study the adsorption geometry, while both NEXAFS and X-ray photo electron spectroscopy (XPS) data yield information concerning the electronic properties of the adsorbed molecules. In addition, a detailed interpretation of the experimental NEXAFS data requires strong theoretical support, which is provided in the present study by model spectra based on density functional theory (DFT) calculations.

Two different types of molecular switches have been chosen in this work in order to attain a deeper insight on how their switching properties are influenced in the vicinity of metallic surfaces. They are shortly introduced here and described in more detail in the beginning of the corresponding chapters. The first system is azobenzene, which represents the group of smallest and thus simplest molecular switches. It consists of two benzene rings that are linked by a N=N azo unit. Azobenzene is known to change between a planar and a non-planar conformation due to light irradiation and/or thermal activation. Two meta-substituted azobenzene derivatives that differ only by their rest groups are used as model systems. While those rest groups are attached in a way such that the central functional azo unit is not influenced, they are expected to deliver complementary information about the adsorbate state. The first candidate of the used azobenzenes derivatives is dimetacyano azobenzene (DMC) and exhibits C≡N cyano rest groups, each carrying two orthogonal π orbital systems. These can be used to get more detailed information about the molecular orientation from the angle dependence of the cyano N K-shell NEXAFS. Since for DMC the N K-shell NEXAFS and the N 1s XPS contain the convoluted contributions of both, the central azo nitrogen and the cyano rest group, a second derivative with carboxymethylester rest groups (CMA) is used as a reference system, since here nitrogen is only present in the center of

the molecule.

In order to study the effect of different adsorbate–substrate interactions, the adsorption on the more inert Au(111) surface is compared with the one on the comparatively more reactive Cu(001) surface. For the latter, a transition from the physisorbed to the chemisorbed state is evidenced by means of temperature-dependent XPS and NEXAFS measurements. For chemisorbed DMC molecules on Cu(001) at room temperature the influence of the intermolecular interactions on the adsorption state is demonstrated by coverage-dependent NEXAFS and interpreted with the help of DFT calculations.

The second species is a spiropyran derivative, which offers a completely different quality. The isomerization process is much more complex, including a bond cleavage and a conformational change in the molecular structure. It was shown that the ring-opened isomer can interact with metallic ions coordinatively without losing the switching capabilities [11]. The same interaction might occur at metallic surfaces, depending on their reactivity. Furthermore the possible coordinative bond might force the molecule into an orientation perpendicular to the surface, in which the excitation-quenching dipole–dipole coupling to the surface is suppressed. Spiropyran is thus a promising candidate as single molecular switch attached to a metallic substrate.

Chapter 2

Core-level spectroscopies

A general approach to characterize an unknown physical (probed) object is to study its interaction with a well known (probing) object that is preferably easy to handle. The term "well-known" refers to the dependence of the probing particle's possible physical states (given by a minimal set of observables) on the interaction with its environment. With spectroscopic methods in a narrower sense, for example, the change of a certain physical property of the probing object in dependence of its initial energy is measured in order to infer the physical qualities of the probed object. Due to their fundamental character elementary particles like photons, electrons, or neutrons are best candidates to be probing objects where the former two are comparatively easy to handle. Thus, and in order to fulfill the term "well-known" for photons, Fig. 2.1 shows the cross sections of several possible processes as functions of the photon energy.

Inelastic scattering with matter, *e.g.*, appears for photons with a reasonable probability at photon energies above 10 keV. This effect is the so-called *Compton effect* and is based on the scattering between photons and quasi-free valence electrons. For electrons, in contrast, inelastic scattering in solid matter occurs with a maximum probability already for energies of about 50 to 100 eV. For photon energies lower than 10 keV photons can either be absorbed completely by using an inner degree of freedom of the involved matter or be scattered elastically with a much smaller probability, so that no energy is passed to the scattering matter.

The absorption process of a photon by matter dominates for particle energies less than $E_{ph} = h\nu < 10$ keV. It can be described in terms of quantum mechanics by the transition from an initial state $|\Psi_i\rangle$ to a final state $|\Psi_f\rangle$ where the difference in total energy of the two states has to be equal to the

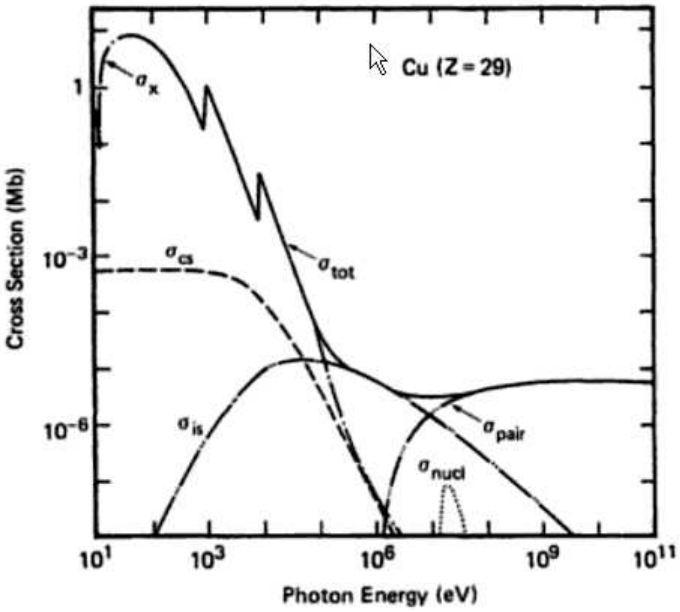

Figure 2.1: *Total σ_{tot} and partial cross sections for light in matter the from 10 eV to 10^{11} eV shown exemplarily for Cu (Z=29). The partial cross sections are given for photoemission σ_x, elastic scattering (Rayleigh) σ_{cs}, inelastic scattering (Compton) σ_{is}, γ absorption σ_{nucl}, and pair production σ_{pair}.*

photon energy:

$$E_{ph} \;=\; \underbrace{\langle \Psi_f | \hat{H} | \Phi_f \rangle}_{=E_f} - \underbrace{\langle \Psi_i | \hat{H} | \Psi_i \rangle}_{=E_i} \tag{2.1}$$

Here $\hat{H}$ is the Hamiltonian that describes the system. The transition probability is usually calculated by quantum-mechanical time-dependent perturbation theory resulting in *Fermi's Golden Rule*:

$$W \;=\; \frac{2\pi}{\hbar} \, |\langle \Psi_f | V_0 | \Psi_i \rangle|^2 \, \delta(E_f - E_i - \hbar\omega) \tag{2.2}$$

Here V_0 is the amplitude of the harmonic time-dependent external potential $V(t) = V_0 \; cos(\omega t)$, contributing as the perturbation term to the complete Hamiltonian. $|\Phi_i\rangle$ and $|\Phi_f\rangle$ are usually the eigenstates of the Hamiltonian of the unperturbed system. The corresponding perturbation potential for an incident light wave can be written with the help of the vector potential $\mathbf{A}(\mathbf{r}, t)$ in the form of a plane wave:

$$\mathbf{A}(\mathbf{r}, t) = A_0 \, \mathbf{n}_p \, \cos(\mathbf{k} \cdot \mathbf{r} - \omega t), \tag{2.3}$$

with the unit vector $\mathbf{n}_p$ giving the direction of the light polarization, the wave vector $\mathbf{k}$, and the angular velocity ω. Furthermore the electric field $\mathbf{E}$ and the

magnetic field $\mathbf{B}$ are represented by $\mathbf{A}(\mathbf{r},t)$:

$$\begin{aligned}\mathbf{E}(\mathbf{r},t) &= -\frac{1}{c}\frac{\partial}{\partial t}\mathbf{A}(\mathbf{r},t)\\ \mathbf{B}(\mathbf{r},t) &= \nabla\times\mathbf{A}(\mathbf{r},t).\end{aligned}$$

In the case that the wavelength is much larger than the size of the light-absorbing object[1], $\mathbf{A}(\mathbf{r},t)$ can be regarded as constant in space. This assumption is called *electric dipole approximation* since consequently $\mathbf{E}(\mathbf{r},t)$ will be constant in space, too, and $\mathbf{B}(\mathbf{r},t)$ will disappear. Thus the light wave is just given by an oscillating electric field in which an electron will have the potential energy:

$$V(\mathbf{r},t) = e\mathbf{E}(t)\mathbf{r} = e\,A_0\frac{\omega}{c}\,\mathbf{n}_p\mathbf{r}\,\cos(\omega t) \tag{2.4}$$

Now one can easily apply this to Equation (2.2) from which we get the following transition probability:

$$W \;=\; \frac{2\pi}{\hbar}\frac{\omega^2}{c^2}A_0^2\,|\mathbf{n}_p\cdot\langle\Psi_f|e\mathbf{r}|\Psi_i\rangle|^2\,\delta(E_f-E_i-\hbar\omega), \tag{2.5}$$

where $\boldsymbol{\mu} = e\mathbf{r}$ is the so-called dipole operator. The corresponding absorption cross section scales linear with the transition probability W.

2.1 Photoemission

An example of light absorption processes is the photon-induced ionization of matter, where an electron is released from the material using the energy of an incident photon. In this simple picture of a one-electron-excitation process, the initial state is the ground state of the participating electronic system, and the final state is the electronic state in the ionized matter plus the free electron. The negative value of the minimum photon energy that is needed for the transition from the ground state into the continuum of final vacuum states is referred to as the binding energy E_B of the released electron. Although this is the correct definition, which we will keep this in the present chapter, in chapter 4 and 5 the corresponding binding energy are given as positiv values.

By the absorption of a photon with an energy $E_{ph} > |E_B|$ the photon energy E_{ph} is passed completely to the electron. This was described first by

[1]This is the case for soft X rays interacting with the core level electrons in solid state systems and molecules. The magnitude of $\mathbf{r}$ for an object is then given by the Bohr radius 0.5 Å and the wavelength is 50 Å.

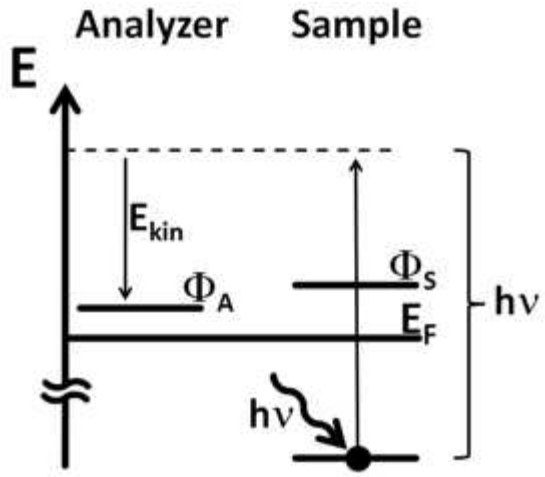

Figure 2.2: *The energy level diagram with relevant values for the measurement of the binding energy by photo emission spectroscopy. E_F is the Fermi energy. Φ_A and Φ_S are the work functions of the analyzer and the substrate, respectively. On the side of the sample an electron (black filled circle) is exited by a photon with the energy $h\nu$, whereas its kinetic energy is measured the analyzer.*

Einstein [19] and is well known as the photoelectric effect. From an isolated atom or molecule the electron will leave the ion with a final kinetic energy:

$$E_{kin} = E_{ph} + E_B. \tag{2.6}$$

The kinetic energy of an electron can be easily detected with a standard photoelectron analyzer, which works as an energy dispersive detector. An experimental problem arises from the fact that both the ionization position r_I where the ionization takes place (without ion) and the position of the analyzer r_A need not to be at the same electric potential. Thus the initial kinetic energy in Eq. (2.6) will be changed by the potential difference $\Delta\Phi_{IA} = \Phi(r_I) - \Phi(r_A)$ between the ionization point and the analyzer:

$$E_{kin} = E_{ph} + E_B - \Delta\Phi_{IA}. \tag{2.7}$$

This makes the absolute energy calibration a crucial point, since $\Delta\Phi_{IA}$ has to be determined. A different situation is given for measurements at a metallic surface. In this case the Fermi levels of the substrate and the analyzer are fixed to each other by an electrical contact, and the energy is measured with respect to the vacuum energy of the analyzer, as it is shown in Fig. 2.2. In any case the work function Φ_A of the analyzer can be assumed as one of its

properties, and we can measure the kinetic energy with respect to the Fermi level:

$$E'_{kin} = E_{ph} + E_B + \Phi_A. \tag{2.8}$$

In order to reference this measured value to the vacuum level in Eq (2.6) , we have to take into account the work function Φ_S of the sample as follows:

$$E_{kin} = E'_{kin} - \Phi_S. \tag{2.9}$$

While the measured values E'_{kin} are obviously referenced to the Fermi level of the substrate, E_{kin} was defined more generally as relative to the vacuum level. The latter definition is useful if we want to understand the ionization process as they were already introduced as a transition between an initial neutral state with the energy E_i and a final state of the ionized species E_f in which the exited electron is promoted to the vacuum level. Here we can write the binding energy as

$$E_B = E_{kin} - h\nu = E_i - E_f. \tag{2.10}$$

The initial and the final state can be regarded as equilibrium states long before and far after the ionization, respectively, where no other process has taken place at any time. In order to get these values from theoretical considerations, one has to calculate both the initial and the final state in terms of quantum mechanics. While the initial state can be considered as the ground state of the system, the final state is an excited state with a missing electron so that the remaining electrons will change their configuration due to the presence of the remaining hole[2]. In a first approximation one can assume that the remaining electrons keep their initial configuration after the electron is removed. This is known as the Koopmans' theorem. In this case the binding energy equals the initial-orbital energy of the released electron.

2.1.1 Primary XPS peaks

The photoelectron signal that is related to a direct transition of a corelevelelectron into the vacuum is in literature often referred as to *primary* XPS peak. Depending on the binding energy of the excited electron promoted, different light wavelengths have to be used to initiate the ionization process. For binding energies $|E_B| < 100$ eV the method is referred to as ultra-violet photoelectron spectroscopy (UPS), whereas for $|E_B| > 100$ eV it is called X-ray photoelectron spectroscopy (XPS). For second-row elements

[2]Due to the presence of this hole the final state is thus far away from equilibrium, but metastable.

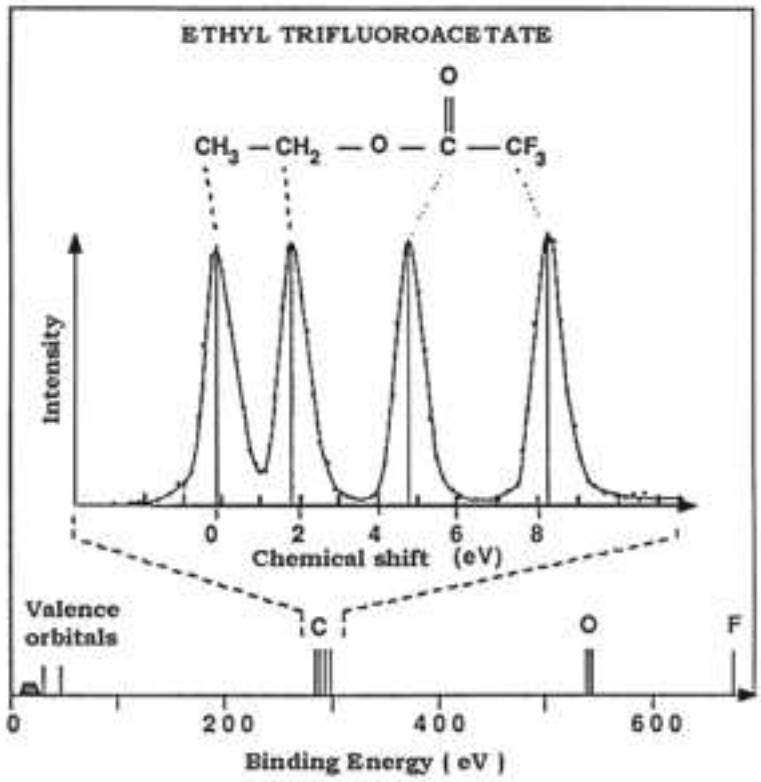

Figure 2.3: *Demonstration of the chemical shift of different carbon atom sites due to the different chemical environment [20].*

(except Li) XPS is used to excite the 1s core electrons, since their binding energies range between 111 eV for Be and 863 eV for Ne (values taken from http://www.lasurface.com/tableau/spectros.php), where the binding energy increases stepwise by more than 80 eV due to the increasing atomic number. In contrast, the energy distribution of the photo-emission signal from the specific 1s core level is usually in the range between a few tenths of 1 eV and 2 eV, so that the signals of the different elements are well-separated in energy. For the investigation of organic molecules one can thus determine the chemical composition on the surface by analyzing the 1s XPS intensities of the contributing elements.

As discussed before, the binding energy of a core electron depends on the electronic configurations of both the initial and the final state. The initial state contributions can be described in terms of Koopmans' theorem where E_B corresponds to the 1s orbital energy of the ground state. This energy raises not

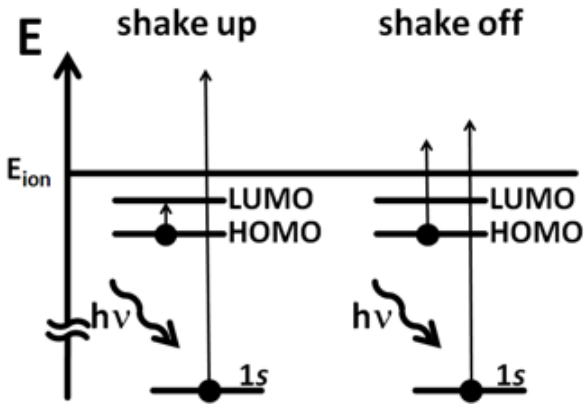

Figure 2.4: *Schematic description of the shake-up/-off processes as coupled multi-transition excitations.*

only from the core induced electrostatic potential, but also from the repulsive electron-electron interaction, and the energy of the electronic exchange and correlation interaction. All these components strongly depend on the chemical environment of the individual excitation centers. Thus the ground-state $1s$ orbital energy can vary for the same element in different chemical compounds.

The final state, on the other hand, is given by the relaxed electron configuration in the presence of a $1s$ core hole. Depending on this configuration, the core-hole screening will vary for the removed electron, since the relaxation process is influenced as well by the chemical environment. Taking both the initial and final state effects into account, the XPS is not only element specific, but also sensitive to the presence of different chemical states. The most prominent example was presented by Siegbahn *et al.* for ethyl-trifluoroacetate shown in Fig. 2.3.

2.1.2 XPS satellites

An interesting side effect that might accompany the photoemission process is the electronic excitation from valence states. This results in additional energy consumption for the secondary process at the expense of the kinetic energy of the photoelectron. That is the reason for the apparently higher binding energy for the participating photoelectron comared to those of the uncoupled transition. The additional excitation can be a HOMO$-x$ $\rightarrow$LUMO$+y$ transition, as well as charge- or energy- transfer processes. In this case the additional resonance in the XPS is called 'shake-up'. Furthermore, there exists the possibility that an additional electron is promoted above the vacuum level. The corresponding resonance is called 'shake-off'. Finally, also vibrational modes can be excited in molecules and solids during the ionization process. Since

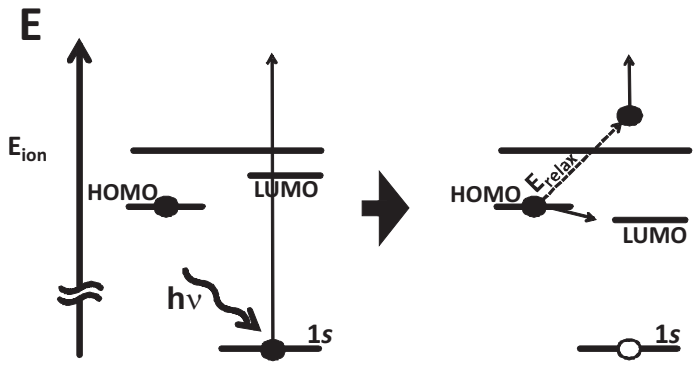

Figure 2.5: *Schematic drawing of a shake-down process. After ionization, the LUMO (HOMO) shifts down (up) in the presence of the core hole. Thus the valence electron relaxes and gives the relaxation energy to the ionized electron.*

the energy for vibronic excitations is rather small compared to the line width of the photoemission peak, this will lead to an asymmetric broadening of the XPS signal.

HOMO-LUMO excitations have been observed in many organic molecules. For mono-substituted benzenes they appear as shake-ups at several eV higher binding energy than the primary peak.

The intensity is rather small for the coupling of allowed optically electric dipole transition to another electric dipole transition from the core hole due to the dipole selection rules [21]. In the cases of a homo-nuclear diatomic molecules the transition between an occupied π-ungerade to an unoccupied π-gerade state is not allowed to couple to a core-leve transition. The fact that a valence optical dipole transition can be still visible as coupled to the core-electron dipole excitation stems from a correlated electron picture that is always more realistic and goes beyond the description of the model of coupled *single electron transitions*. In the theory this is accounted for by the so-called **C**onfiguration **I**nteraction (**CI**), where more than one occupation scheme is considered for in the form of a linear combination of different Slater determinants (cf. Sec. 3.2.2). The electron correlation is included, regarding two configurations, namely one of the dipole excited core hole and one of a dipole excited valence electron that are interfering after photonic excitation. The smaller intensity of the satellite is then approximately given by the lower probability of the valence excitation.

Charge transfer is another mechanism that can couple to the core-electron excitation. In a conjugated molecular structure the generated core hole can cause a redistribution of the remaining charges in order to compensate partially the higher local charge density at the core hole side. This screening effect would simply lead to a chemical shift in the main XPS feature. The compensation by charge transfer can be further influenced by the presence of electron-donor/-acceptor groups since they cause a polarization in the charge distribution. Polarization in this sense refers to that the partial localization of certain molecular orbitals is not compensated mutually in order to get a homogeneously distributed electron cloud. In this case the appearance of a core hole further increases the polarization. For paranitroaniline the increase of the polarization can even cause a change in the energetic order of the HOMO and the LUMO states, which has been demonstrated by Domcke and co-workers [22]. In this case the occupation of the LUMO can compensate the charge of the NO_2 N $1s$ core hole much more effectively than the HOMO occupation. Since the energy gain of the relaxation process in the occupied LUMO is much bigger than the HOMO–LUMO splitting, the corresponding transition gives a positive energy balance, which leads to an even higher kinetic energy for the coupled transition than for the main XPS peak. This would give a satellite at lower binding energy which is thus called 'negative shake-up' or 'shake-down'.

2.1.3 Photoelectron cross section

Returning to the beginning of this chapter and regarding the different types of interaction of photons and electrons with matter, two aspects have to be considered for an astimation of the expectable intensities in XPS measurements. First of all, the X-ray photons have to be absorbed in order to induce the photoelectron emission process, and secondly, the emitted electrons should not be scattered inelastically on the way to the detector.

X-ray photon absorption In general, the reduction in intensity of electromagnetic irradiation in matter as a fuction of the covered distance d is given by:

$$I(d) = I_0 e^{-\mu d}, \tag{2.11}$$

where I_0 is the initial intensity, and μ is the so called absorption coefficient. The latter depends on the mechanism that is responsible for the reduction of the intensity. In the case of X rays with photon energies between 100 eV and 250 keV, possible processes are photoemission and elastic photon scattering, where the former dominates by at least two orders of magnitude (cf. Fig. 2.1).

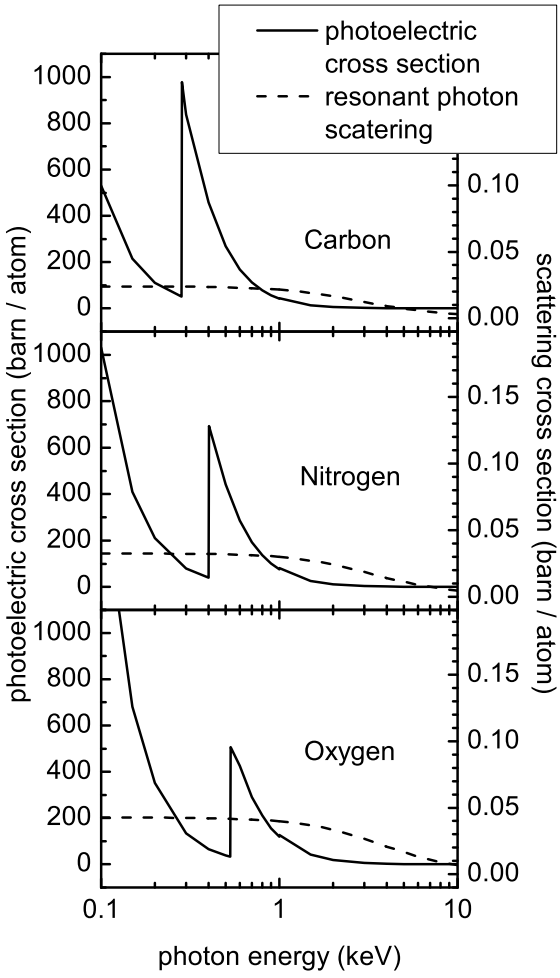

Figure 2.6: *Energy-dependent cross section for X-ray photonelectric (solid line) and coherent photon scattering (dashed line) processes in carbon, nitrogen and oxygen. Data are taken from Ref. [23].*

In the case of photoelectron emission, the cross section, and thus the absorption coefficient σ, depend on the atomic number Z of the absorbing element and on the X-ray photon energy E_{ph}. Since they are the most relevant for this thesis, the photoelectric cross sections for carbon, nitrogen, and oxygen are presented in Fig. 2.6. At this point it is interesting to discuss the relative difference between, *e.g.* the N 1*s* XPS signal measured with synchrotron radiation, where one tune the excitation energy to 500 eV, and that yield by a standard lab Mg Kα X-ray source with a fixed photon energy of 1286 eV. Assuming the same photon flux for both experiments, the cross section of the latter is six times smaller.

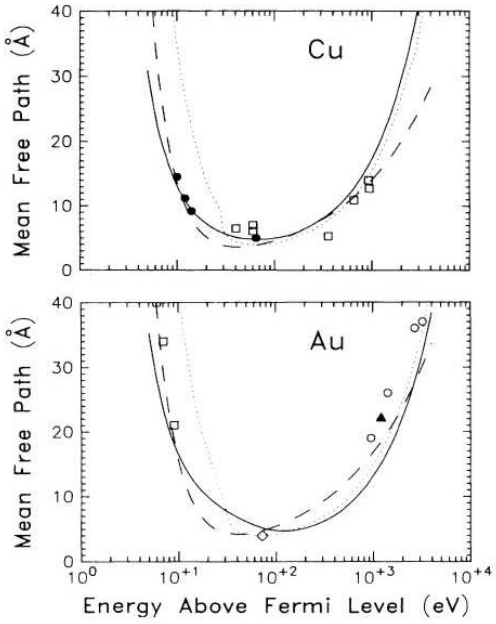

Figure 2.7: *Mean free paths for the inelastic electron scattering process in solid copper and gold where solid and dashed lines are from theory, whereas triangular, circular, and squared symbols represent corresponding experimental data [24]*

Inelastic electron-electron scattering appears due to the interaction of a photo-excited (primary) electron with valence electrons of the surrounding matter. This results either in a plasmonic or in a single-electron excitation, where the latter can lead to the emission of the a secondary electron if the transferred energy is sufficiently large. The kinetic energy of those secondary electrons ranges typically between 0 and 50 eV. Due to the high contribution of secondary electrons to the total photoemission signal, the excitation energy has to be sufficiently high to avoid the overlap of the core electron signal with that of the secondary electrons. Regarding this, and the photon-energy dependence of the photoelectric cross section given in Fig. 2.6, we found the excitation energies of 500 eV for the N 1*s* and 650 eV for the O 1*s* XPS as appropriate values.

Furthermore the energy loss caused by the inelastic scattering processes restricts the length of the electron's traveling path. Analogous to the intensity of the X-ray beam, we can describe the absorption of the photoelectrons by the Beer-Lambert law (Eq. (2.11)), where the corresponding $\mu = \frac{1}{L}$ is much bigger for low energy electrons than for X-ray photons. The mean free paths L for electrons in Cu and Au substrates are shown in Fig. 2.7 as a function of their initial kinetic energy with a minimum of L = 2 Å at arround 100 eV. Thus of all the X-ray photoelectrons produced in the bulk material only those coming from outer substrate layers will escape from the sample without energy

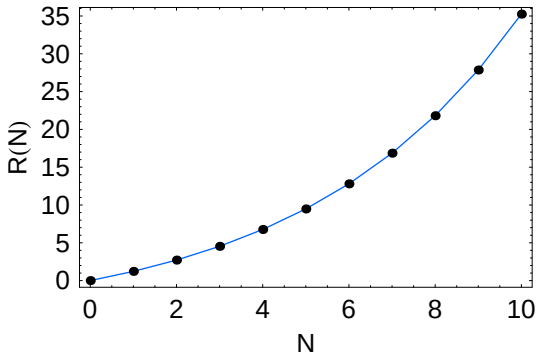

Figure 2.8: *Coverage dependent ratio between adsorbate and substrate XPS intensity as a function of the number of monolayers N, assuming that the XPS intensities for 1 ML adsorbate and for the clean substrate are equal ($I_{a0}/I_{s0} = 1$) and that the ratio between the layer thickness and the inelastic electron mean free path in the adsorbate is $\frac{d}{L} = 0.2$.*

loss and contribute to the photoemission signal. Furthermore a adsorbate film will attenuate the XPS signal of the substrate with increasing film thickness. Assuming the simple case of a layer-by-layer growth, for N closed layers with monolayer thickness d and an adsorbate mean free path L, the intensity of the substrate XPS signal will decrease exponentially:

$$I_{subst}(N) \;=\; I_{s0}\, e^{-\frac{Nd}{L}},$$

with the XPS intensity of the clean substrate $I_{s0} = I_{subst}(N = 0)$, while the intensity of the adsorbate XPS signal increases with N:

$$\begin{aligned} I_{ads}(N) \;&= I_{a0} \sum_{i=1}^{N} e^{-\frac{(i-1)d}{L}} \\ &= I_{a0}\, \frac{e^{\frac{d}{L}}(e^{\frac{d}{L}N} - 1)}{e^{\frac{d}{L}N}(e^{\frac{d}{L}} - 1)} \end{aligned}$$

with a 1 ML photoemission intensity $I_{a0} = I_{ads}(N = 1)$. Since both intensities are proportional to the intensity I_{xray} of the incident X-ray light, their ratio

$$R(N) \;=\; \frac{I_{ads}}{I_{subst}} \;=\; \frac{I_{a0}}{I_{s0}}\, \frac{e^{\frac{d}{L}}(e^{(N+1)\frac{d}{L}} - 1)}{e^{\frac{d}{L}} - 1} \tag{2.12}$$

will be independent of I_{xray}. This makes the thickness calibration insensitive i.e. to the characteristic change of X-ray emission intensity of a synchrotron radiation source over time due to the typical loss of electrons in the storage ring. An example for the coverage dependence of R is given in Fig. 2.8.

For the formation of the Nth single layer (corresponding to the interspace between two consecutive data points in Fig. 2.8), the intensities I_{ads} and I_{subst}

will increase and decrease linearly, respectively:

$$I_{ads}^{1ML}(x) \;=\; (I_{ads}(N) - I_{ads}(N-1))x + I_{ads}(N-1)$$

$$I_{subst}^{1ML}(x) \;=\; I_{subst}(N) - (I_{subst}(N) - I_{subst}(N-1))x$$

where x is the fraction of the already formed monolayer. For the first monolayer $I_{ads}(N-1) = 0$ so that the ratio R(x) can be written:

$$R(x) \;=\; \frac{I_{a0}\; x}{I_{subst}(1) - (I_{subst}(1) - I_{s0})x}. \tag{2.13}$$

2.2 Near edge X-ray absorption fine structure

In the case that the excitation energy of the incident photon E_{ph} is close to the binding energy E_B of a core-level electron, the excitation into an unoccupied molecular orbital can be induced, instead of the direct photoelectron emission. The X-ray absorption spectrum around the ionization barrier thus exhibits a specific **N**ear **E**dge **X**-ray **A**bsorption **F**ine **S**tructure (**NEXAFS**), shown in the upper left inset of Fig. 2.9 (compare to Sec. 2.1.3, where the edges are just edge jumps). The appearance of the contributing resonances as narrow features around the well-separated absorption edges allows an element-specific probing of the electronic and chemical properties around the different excitation centers. In the electron configuration scheme that reproduces the arrangement of electronic states in a fictive multiple atomic-core potential, all allowed $1s$ transitions are indicated by the horizontal arrows. A possible localization of the final unoccupied molecular orbitals ($4\pi^*$, $5\pi^*$, and $6\pi^*$ levels) is denoted by the distribution of the corresponding iso-energy lines. Only selected transitions are possible regarding the localization of both, the initial core hole and the final molecular orbital. This leads a to characteristic shape in the NEXAFS spectra of the different edges visible in the upper right part of Fig 2.9.

Depending on E_{ph} the excited electron either remains in a bonded state of the molecule or leaves the excitation center with a relatively small energy. Both cases together result in different features in the NEXAFS that will be discussed below.

2.2.1 Spectral structure

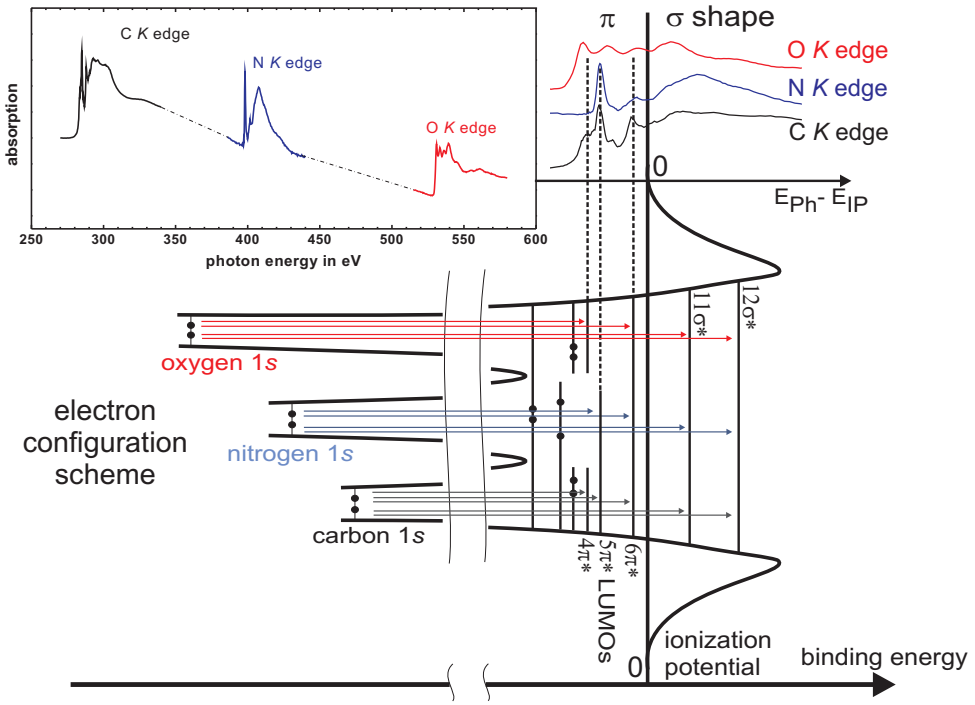

Figure 2.9: *Simple schematic drawing of a core-level excitation in a fictive molecule containing three different atomic sites. Near X-ray absorption fine structure is given as a survey in the inset at the left upper corner whereas the detailed peak assignment to the final states can be seen in the right upper corner. The terms E_{ph}, and E_{IP} denote the photon energy and the ionization potential, respectively.*

pi resonances For $E_{ph} < E_B$, the electron can be promoted from the core level into an unoccupied molecular orbital below the ionization barrier where the corresponding *Feshbach resonances* are referred to as π^* *resonances*. In this case the electron remains in the molecular confinement. The electronic excitation can subsequently decay either by fluorescence or by an Auger process. In the latter case the core hole is refilled by an electron from an atomic shell above the core level, and the relaxation energy is used for the emission of a third electron. For the second-row elements the Auger process is much faster than the fluorescent relaxation of the core-excited electron and thus restricts the life time of the excitation and the line width of the corresponding resonance. For carbon, nitrogen, and oxygen, the natural line widths are below 0.1 eV [25]. Thus for a sufficiently high experimental resolution it was shown that even the vibrational fine structure can be observed for certain π^* resonances [26, 27].

sigma resonances Photonic excitations up to around 15 eV beyond the ionization barrier will provide enough energy to induce a photoemission process, but due to the small difference between excitation and binding energies, the electron will escape only slowly from the influence of the remaining molecular ion. Therefore, the escaping electron can be assumed as reacting instantaneously on changes in the remaining electron ensemble, so that the interaction can be regarded as adiabatic. Two models have been suggested in order to describe the excitation process. In a quantum chemical picture, the electron is excited via one of the higher virtual molecular orbitals above the ionization threshold, which interferes with the continuum of vacuum states. Another attempt that assumes the electron temporarily trapped in a potential barrier that arises from attractive (Coulomb) and repulsive (centrifugal, electron screening) forces. In this case the electron is allowed to tunnel through this barrier. Both descriptions result consistently in fair agreement with experimental observations [28] where a partly enhanced ionization rate is visible as a broad resonance in the X-ray absorption spectrum[3]. The excitation of the core-level electron in the continuum is followed by an Auger process. Since the primary ionized core electron is only slowly removed from the atom it can interact with the subsequently released Auger electron [29]. Thus both, excitation (by photoemission) and deexcitation (by an Auger process), have to be regarded as one process (*intra-channel decay*), which makes a theoretical description and a reasonable interpretation of experimental data much more complicated.

Shake-up resonances As discussed in Sec. 2.1.2, core level excitations can be accompanied by secondary electron transitions from valence states. In Chapter 2.5.3 of Ref. [30] it was further reported that the possibility of such transition is predicted by theoretical considerations to vanish in the adiabatic regime in which NEXAFS is measured. However, for CO the existence of such double excitations has been demonstrated by means of angle-resolved photoemission [31]. Since the energy consumption of such a process is increased by the transition energy of the contributing valence state excitation (compared to the single core excitation), the corresponding resonance appears above the ionization energy although no ionization takes place. Unavoidably the corresponding resonances appear convoluted with the (single excitation) σ resonances in the NEXAFS spectra. Assuming that the final state of the

[3]In contrast, for the common XPS measurements with kinetic electron energies of more than 50 eV, the XPS signal does not depend on E_{ph} but indirectly via the monotonic long-range decrease of the photo emission cross section shown in Fig. 2.6.

shake-up transition does not have the same symmetry as the final state of the competing σ resonance, the convoluted features will contibute with different angle dependeces to the same spectral region. This makes the analysis of the orientation of the corresponding bond orbitals a bold venture if no adequate theoretical simulation of the NEXAFS spectra is employed (compare withnext section).

2.2.2 Angle dependence

From Eq. (2.5) we see that the absorption cross section depends on the relative orientation of the polarization of the light and the transition dipole moment $\langle \boldsymbol{\mu} \rangle = \langle \psi_f | e\mathbf{r} | \psi_i \rangle$. For the C, N, and O K-shell NEXAFS the initial state is an s orbital of radial symmetry, whereas the final bond orbital can be considered as a linear combination of atomic p orbitals with the same symmetryas the p orbitals. For this linear combination $\langle \boldsymbol{\mu} \rangle$ will have the same orientation as the rotation symmetry axis of the contributing atomic p orbitals. In the case of σ bonds, the orientations of $\langle \boldsymbol{\mu} \rangle$ and the bond axis are parallel, whereas for π bonds, they are perpendicular. For the X-ray absorption by a single molecule, the two vectors $\mathbf{n}_p$ and $\boldsymbol{\mu}$ can be written in spherical coordinates:

$$\mathbf{n}_p(\vartheta, \phi) = \begin{pmatrix} \cos\varphi \ \sin\vartheta \\ \sin\varphi \ \sin\vartheta \\ \cos\vartheta \end{pmatrix} \quad \text{and} \quad \langle \boldsymbol{\mu}(\Theta, \Phi) \rangle = e|\langle \mathbf{r} \rangle| \begin{pmatrix} \cos\Phi \ \sin\Theta \\ \sin\Phi \ \sin\Theta \\ \cos\Theta \end{pmatrix}$$

Here the angles φ and ϑ define the azimuthal and polar (here referred to as *zenithal*) orientation of the polarization vector, respectively, whereas the alignment of the final state orbital is given by Φ and Θ. The angle dependence of the absorption cross section σ_{xray} is then given solely by the projection of the polarization vector on the symmetry axis of the final state orbital:

$$\sigma_{xray}(\vartheta, \varphi, \Theta, \Phi) \ \sim \ |\mathbf{n}_p(\vartheta, \varphi) \cdot \langle \mathbf{r}(\Theta, \Phi) \rangle|^2 \tag{2.14}$$

Considering the adsorption of molecules on a surface and stipulating that the surface corresponds to the $x - y$ plane of our coordinate system, the azimuthal orientations of the polarization vector and the dipole moment are given by φ and Φ, respectively. Then ϑ and Θ describe the zenithal angles between the corresponding vectors and the surface normal. Assuming that the adsorption of the molecules occurs in an azimuthal N-fold symmetry on the surface, N azimuthal orientations are possible and have to be considered for

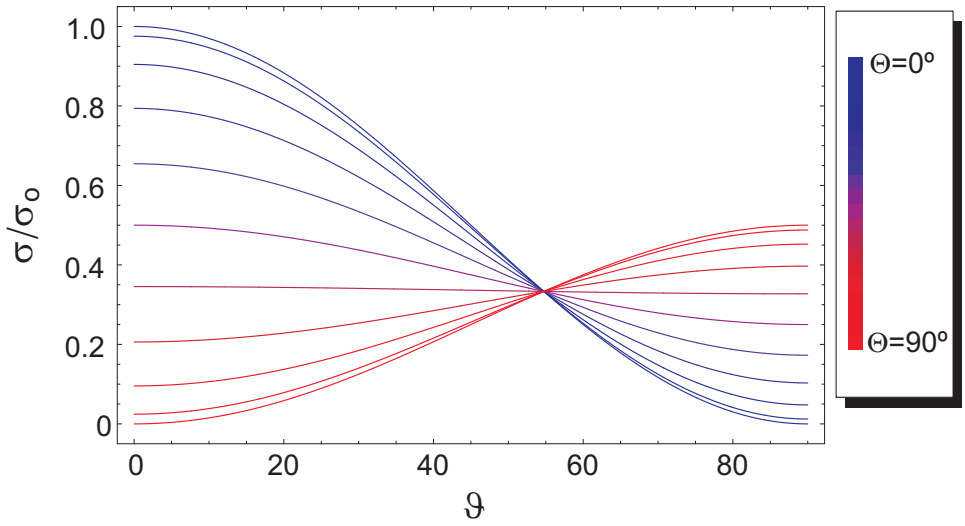

Figure 2.10: *Dependence of the relative absorption cross section on the zenithal angle of the polarization ϑ for different orbital orientations Θ. σ_0 is the largest possible cross section and is obtained with both orbital and polarization oriented parallel to the surface normal.*

the calculation of the cross section:

$$\begin{aligned}\sigma_{xray} &\sim \frac{1}{N}\sum_{i=1}^{N} |\mathbf{n}(\vartheta,\varphi)\cdot\langle\mathbf{r}(\Theta,\frac{2\pi}{N}i)\rangle|^2 \\ &= \frac{1}{N}\sum_{i=1}^{N} |\cos\vartheta\,\cos\Theta + \sin\vartheta\,\sin\Theta\,\cos(\frac{2\pi}{N}i-\varphi))|^2\end{aligned}$$

The sum gives two solutions depending on the degree of symmetry:

$$\sigma_{xray} \sim \begin{cases}(\cos\vartheta\,\cos\Theta)^2 + \frac{1}{2}(\sin\vartheta\,\sin\Theta)^2(1-\cos 2\varphi) & \text{if } N<3\\ (\cos\vartheta\,\cos\Theta)^2 + \frac{1}{2}(\sin\vartheta\,\sin\Theta)^2 & \text{if } N\geq 3.\end{cases}$$

For an N-fold symmetry with $N \geq 3$ the absorption cross section does not exhibit any azimuthal angle dependence. This includes the case that the azimuthal orientation of the adsorbate is random (in other words for the highest azimuthal symmetry). Then N has to be set to ∞, and the cross section only depends on ϑ and Θ. For this case Fig. 2.10 shows the zenithal angle dependence of the photon absorption cross section. Since it is difficult to determine experimentally the absolute cross section for a certain transition, one usually takes the ratio of the different intensities measured for two different ϑ. Typical

values in this work are $\vartheta = 90°$ normal incidence and variable angle $\vartheta_{grazing}$ for grazing incidence:

$$R \;=\; \frac{\sigma_{xray}(\vartheta_{grazing})}{\sigma_{xray}(\vartheta = 90°)} \;=\; 2\cot^2(\Theta)\cos^2(\vartheta_{grazing}) \;+\; \sin^2(\vartheta_{grazing}) \qquad (2.15)$$

From this ratio the orientation of the π^* orbitals can be concluded and detailed information about the adsorption geometry of the molecules becomes avaliable.

2.2.3 Data acquisition

In this work, all NEXAFS data have been taken in the so-called **T**otal **E**lectron **Y**ield (**TEY**) mode, where the total current between the isolated sample and the electric ground potential is measured. These current arises from secondary electrons that are generated after core electron excitation by the subsequent Auger decay. The advantage of this method is given by the comparably easy set-up consisting of an isolated sample holder and a picoampere meter. The disadvantage is the background signal that originates for low coverages mostly from the metallic substrates, and may dominate the whole electron signal. The contribution, e.g., from a monolayer of organic adsorbate is, for C-, N-, and O-K edges, usually in the range of 0.1 % – 1 %, depending on the partial density of the different elements. Given a noise-to-signal ratio of the beam line of about 0.03 %, the resulting ratio in the adsorbate signal is around 3 % to 30 %. Thus, the beam lines were equipped with a Au grid that in front of the sample in order to monitor the short-term intensity fluctuations of the beamline during data aquisition. In order to eliminate artefacts that come from spectral feartures of the substrate in the regions of the C-, N-, and O-K edges, the clean substrate spectra have been measured in addition. All data have been treated by the subsequent data processing procedure to extract the pure low-noise adsorbate signal by the following formula:

$$I = \frac{I_{Sample}/I_{Grid}^{Sample}}{I_{Substrate}/I_{Grid}^{Substrate}}. \qquad (2.16)$$

Here I_{Sample} is the TEY signal of the adsorbate plus substrate and I_{grid}^{Sample} the corresponding signal taken simultaneously from the Au grid. $I_{Substrate}$ is the TEY signal of the clean substrate and $I_{grid}^{Substrate}$ the corresponding Au grid current. Finally, all spectra have been divided by their pre-edge intensity so that the displayed spectra show the relative contribution of the adsorbate to the entire signal.

2.3 X-ray sources

In order to initiate an electronic transition from the C, N, and O 1s core levels into an unoccupied molecular orbital or a vacuum level, X-ray photons of adequate energies have to be generated. For XPS the photon energy can be fixed above the ionization threshold, as it is provided by an X-ray gun. In contrast, for NEXAFS a tunable light source is needed to measure the energy-dependent absorption. Such a tunable light source can be built up by combining any X-ray emitter with a continuous spectrum with a monochromator. In priciple one could use the Bremsstrahlung of an X-ray gun but in practice the intensity and thus the signal-to-noise ratio of the resulting monochromatized components are too low to be used in standard NEXAFS experiments. This is correlated to the fact that the emitting area and the divergence of the X-ray gun are far too big, so that an adaptive optics coupling the X rays to the monochromator would even sizeably decrease the mentioned signal-to-noise ratio and limit the resolution of the set-up. Therefore synchrotron radiation, with an incomparably higher brilliance, is normally used for X-ray absorption studies and for excitation-energy dependent XPS.

2.3.1 X-ray gun

The X-ray gun is a comparably easy to handle X-ray source that can be advantageously used in small laboratory set-ups. The working set-up is well known from applications in materials and medical science. Electrons are accelerated by an electric field from a cathodic filament onto an anode that is covered with a thin layer of suitable metallic material. The incident electrons, with a kinetic energy higher than the binding energy of the target's electrons, ionize the anode material. The produced electron holes are subsequently filled by target electrons from higher atomic shells under the emission of photons. The choice of the material that covers the anode and thus emits the fluorescence photons depends on the excitation energy that is needed for the photo emission experiments. Aluminum and magnesium anodes are among the most common targets. In both cases electrons from the second inner atomic shell decay into the 1s core hole, leading to the so-called characteristic Kα emission. The corresponding photon energies for Mg and Al are 1253 eV and 1487 eV, respectively.

The natural line width of the $2p \rightarrow 1s$ transitions are 0.61 eV and 0.83 eV for Mg and Al, respectively [32, 33]. Thus the experimental energy resolution is restricted to around 0.8-1.0 eV, assuming resolution of the electron analyzer of 0.6 eV. Furthermore, the light emitting spot is around 0.5 cm in diameter

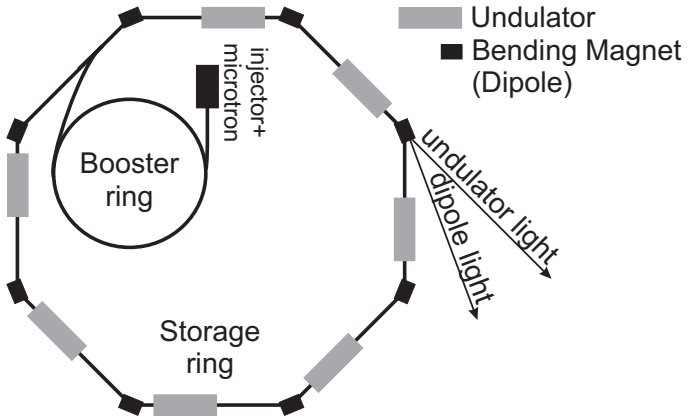

Figure 2.11: *Schematic draw of a synchrotron set-up.*

and the typical divergence is in the order of 1 rad. Without any additional X-ray optics the sample has to be prepared homogeneously over an area of about 1 cm^2 in order to optimally exploit the emitted intensity.

2.3.2 Synchrotron radiation

X-ray light of variable photon energy is provided by synchrotron radiation facilities. The experiments presented here were carried out at the **B**erlin **E**lectron **S**torage ring for **Sy**nchrotron radiation (BESSY), a rough schematic drawing of which is shown in Fig. 2.11. As derived from Maxwell's equations, accelerated charges emit electromagnetic radiation, as it is observed in dipole antennas. For an electron that goes along a circular path, the emission direction is along a two-lobe parallel to the velocity vector. As the velocity approaches the speed of light, the relativistic description of the electrons reveals that the emission folds toward the velocity vector, so that the emitted X-ray beam becomes more collimated.

In order to get such a relativistic electron beam, in modern synchrotron radiation facilities a three step-acceleration set-up is used. In the first step the electrons are linearly accelerated by a static electric field. The second stage can be a so called microtron, in which the electrons are forced on a circular path by magnetic forces and alternately accelerated by an oscillating electric field as known from other cyclotrons. The third stage is the so-called booster (synchrotron) ring in which the electrons pass several rounds through a linear accelerator until they reach a final energy (1.7 GeV in the case of BESSY of).

The high-energy electron beam is then injected into a storage ring (cf. Fig. 2.11). The ring consists of linear segments connected by bending magnet

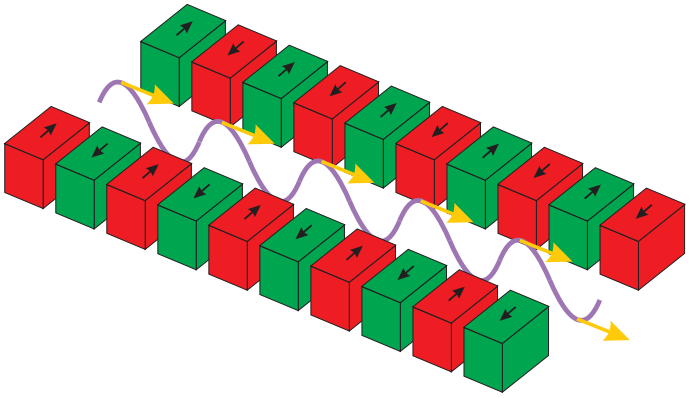

Figure 2.12: *Schematic drawing of an insertion device. Red and green cubes represent the permanent-magnet units, while the black arrows indicate their magnetization. The pink line shows the trajectory of the electron beam in the present magnetic field. The orange arrows symbolize the emmitted light.*

dipoles that force the electron on a circular trajectory insight the magnet. This deflection causes the electrons to emit a collimated X-ray beam. Furthermore the linear segments of third generation synchrotrons are equipped with insertion devices (**ID**) that, in the simplest case, consist of a sequence of permanent magnetic dipoles of opposite magnetization direction, as shown in Fig. 2.12. In the field of this sequence the electron's trajectory is undulating wave-like. Due to the resulting acceleration, the electrons emit a maximum number of photons along the axis of the ID, at the undulating path's extrema. In the case the magnetic field is adjusted such that the emission points are a multiple of the wave length of the emitted light so that constructive interference appears, the X-ray intensity will be further enhanced. Such devices are called undulator. The energy loss due to all the radiation is reinduced to the electrons by an additional linear accelerator that is mounted at the storage ring.

All present data were taken either at the dipole beamline PM3 or the undulator beamlines UE56-2/PGM1 and PGM2. PGM here means plane grating monochromator and denotes the type of monochromator that is used in all three beamlines to further monochromize the X-ray light to resolutions of around $E/\Delta E$ =2500 up to 500 eV, for a reasonable signal-to-noise ratio at the undulator beamlines and half of this value for the PM3 dipole station.

Since for all electrons the acceleration is approximately the same through the dipole devices.[4], the generated dipole radiation is highly polarized in the

[4]The electrons which are compressed into moving bunches are of course spatially distributed and find thus slightly different ways through the magnetic fields.

plane of the electron's two-dimensional circular path. In the case that the configuration of the IDs causes a similar planar path, the polarization will be linear in the trajectory plane. In the UE56/2 beamlines this orientation can be switched from in the synchrotron-ring plane to out-of-the plane by the rearrangement of the permanent magnets. The obtained degree of polarization was 90 % for the used undulator used, as well as for the dipole.

Chapter 3

Simulation of NEXAFS

One of the most crucial parts in experimental science is of course the interpretation of the measured data. A reductive method has been developed in order to interpret NEXAFS spectra of complex molecules on the base of data measured for smaller constituents. This empirical method is called *building block analysis*. While the use of intuition and experience helps the experimentalist to get a more quantitative understanding, the application of physical simulations based on theoretical models can provide a more detailed view into the investigated systems.

In this sense, the data obtained by the experimental methods introduced in Chapter 2 can be fully understood only with the help of theoretical calculations. NEXAFS measured for chemical compounds, in particular, provides us with a set of information, namely the energetic positions of the resonances, their intensities, and line shape that are connected to the energy, the probability, and the type of observed electronic transitions, respectively. All three quantities depend on the electronic configuration and thus on the chemical state of the molecule. On the other hand, such a chemical state can be simulated by quantum chemical calculations. From the output one can then further derive a whole set of theoretical data. The comparison of those with the measured data can help to understand the experimental results and to improve the applied model.

In this chapter, a brief introduction will be given into the theoretical description of molecular states and the calculation of the corresponding intertransitions. It will be explained how one can derive a certain set of spectral information from the calculation output. All the facts will be explained related to the molecules that have been investigated in this work.

3.1 Molecular states

Since the physical quantities of molecules are in the range where Heisenberg's uncertainty principle is valid, one has to treat those objects in terms of quantum mechanics (**QM**). In general, a quantum-mechanical system can be sufficiently well described by Schrödinger's equation as it is given in many text books:

$$i\hbar\frac{\partial}{\partial t}\,\Psi(t) \;=\; \hat{\mathcal{H}}\,\Psi(t), \tag{3.1}$$

with the Hamilton operator:

$$\hat{\mathcal{H}} \;=\; \hat{T} \;+\; \hat{V}.$$

Here $\hat{T}$ and $\hat{V}$ are the operators for kinetic and potential energy, respectively. The function $\Psi(t)$ represents the molecular quantum-mechanical state at every time t involving all contributing particles, namely all nuclei and electrons. Assuming that there is no external time-dependent distortion, the total energy E is constant in time and thus an observable, whereas Eq. (3.1) can be written as:

$$E\;\Psi(\mathbf{R},\mathbf{r}) \;=\; \hat{\mathcal{H}}\;\Psi(\mathbf{R},\mathbf{r}). \tag{3.2}$$

$\mathbf{R}$ and $\mathbf{r}$ are the coordinates of the nuclei and electrons, respectively. The corresponding Hamilton operator consists of the two contributions of the electronic and the atomic-nucleus system:

$$\hat{\mathcal{H}} \;=\; \hat{T}_e \;+\; \hat{T}_n \;+\; \hat{V} \tag{3.3}$$

with

$$\begin{aligned}
\hat{T}_e \;&=\; -\frac{\hbar^2}{2m_e}\sum_{i=1}^{N}\Delta_i \qquad\qquad \text{electron kinetic energy}\\
\hat{T}_n \;&=\; -\frac{\hbar^2}{2}\sum_{n=1}^{A}\frac{1}{m_n}\Delta_n \qquad\qquad \text{core kinetic energy}\\
\hat{V} \;&=\; \underbrace{\sum_{k=1}^{A}\sum_{l>k}^{A}\frac{Z_k Z_l e^2}{|\mathbf{R}_k-\mathbf{R}_l|}}_{\text{core-core repulsion}} \;-\; \underbrace{\sum_{i=1}^{N}\sum_{k=1}^{A}\frac{Z_k e^2}{|\mathbf{R}_k-\mathbf{r}_i|}}_{\text{core-electron attraction}} \;+\; \underbrace{\sum_{i=1}^{N}\sum_{j>i}^{N}\frac{e^2}{|\mathbf{r}_i-\mathbf{r}_j|}}_{\text{electron-electron repulsion}}.
\end{aligned}$$

N and A are the numbers of electrons and nuclei, respectively. $\hat{V}$ represents the entire electronic potential energy of all the individual particles in the field of the neighboring charges. For simplicity, m_e and $\hbar$ will be set to one in the following formulars.

The Hamilton operator $\hat{\mathcal{H}}$, applied to Eq. (3.2), gives an expression that describes the molecule exactly, but unfortunately it cannot be solved analytically. For molecules that consist of more than three particles, a numerical treatment is the only access to a theoretical description.

3.2 Quantum-chemical methods

The general assumption is that for an arbitrary wave function $\Psi(\mathbf{R}, \mathbf{r})$ describing a physical system the corresponding total energy E cannot be lower than the total energy E_0 of the ground state of the system. Thus one has minimize the system's total energy by the variation of the corresponding wave function in order to get the function of the electronic ground state. Therefore one has to find an adequate initial wave function $\Psi_{start}(\mathbf{R}, \mathbf{r})$ which can be varied by a set of parameters. A further problem arises from the shape of the Hamiltonian given in Eq. (3.3). Since several summands in $\hat{\mathcal{H}}$ contain coordinates of more than one particle, all solutions $\Psi(\mathbf{R}, \mathbf{r})$ of Eq. (3.2) are functions, representing a system of correlated particle dynamics. In this case the application of Ritz' method is difficult. Thus, the usual approach is to perform a separation of variables on the partial differential equation (3.2) in order to get a solution $\Psi_{Start}(\mathbf{R}, \mathbf{r})$ that can be written as a function of the single-particle functions by using the two following simplifications.

3.2.1 Born-Oppenheimer approximation

The Born-Oppenheimer approximation assumes that the dynamic of the atomic nuclei is much slower than that of the electrons meaning that the electron configuration responds instantaneously to the change of the nuclei coordinates. Thus, for each nuclei configuration one can calculate the corresponding relaxed electron configuration represented by $\phi(\mathbf{R}, \mathbf{r})$, while the nuclei configuration is given by a fixed potential $\hat{V}_{ne}(\mathbf{r})$ for the nucleus-electron attraction term of $\hat{V}$ in the Hamiltonian. In this case, $\mathbf{R}$ is only a parametric variable. This leads finally to the separation of nuclear and electron Hamiltonian so that we can write $\Psi_{start}(\mathbf{R}, \mathbf{r}) = \chi(\mathbf{R})\phi(\mathbf{R}, \mathbf{r})$ with the nuclear wave function $\chi(\mathbf{R})$. Treating only the electron dynamics, $\hat{T}_n$ disappears and the nucleus-nucleus repulsion contributes as a constant V_n to $\hat{V}$ in the Hamiltonian given

in Eq. (3.3):

$$\begin{aligned}\hat{\mathcal{H}} &= \hat{T}_e + \hat{V} \\ &= \hat{T}_e + V_n + \sum_{i=1}^{N} \hat{V}_{ne}(\mathbf{r}_i) + \sum_{i=1}^{N}\sum_{j>i}^{N} \hat{V}_{ee}(\mathbf{r}_i, \mathbf{r}_j),\end{aligned} \tag{3.4}$$

where the operator $\hat{V}_{ee}$ represents the electron–electron repulsion. In this case $\phi(\mathbf{r})$ is only a function of the electron coordinates.

3.2.2 Hartree-Fock approximation

A further step to elude the multi-particle problem, which is still present in the operator $\hat{V}_{ee}(\mathbf{r}_i, \mathbf{r}_j)$ in (3.4), is done by describing the all-electron system by the Slater determinant in form of a product function:

$$\phi(\mathbf{r_1}, ..., \mathbf{r}_N) \;=\; \frac{1}{\sqrt{N!}} \begin{vmatrix} \varphi_1(\mathbf{r}_1) & \cdots & \varphi_1(\mathbf{r}_N) \\ \vdots & \ddots & \vdots \\ \varphi_N(\mathbf{r}_1) & \cdots & \varphi_N(\mathbf{r}_N) \end{vmatrix} \tag{3.5}$$

where N is the number of electrons. Φ a fermionic wave functions. It obeys Pauli's exclusion principle, in which the exchange of two electrons causes a change of the sign of ϕ. If one now claims that the single-electron functions φ_i represent an orthonormal basis set, one can apply the Hamiltonian (3.4) as follows:

$$E \;=\; \langle\phi|\hat{\mathcal{H}}|\phi\rangle \tag{3.6}$$

$$\;=\; \underbrace{\langle\phi|\hat{T}_e|\phi\rangle}_{=E_{kin}} + V_n \;+\; \underbrace{\langle\phi|\hat{V}_{ne}|\phi\rangle}_{=E_{ne}} \;+\; \underbrace{\langle\phi|\hat{V}_{ee}|\phi\rangle}_{=E_{ee}}\,, \tag{3.7}$$

with

$$E_{kin} \;=\; -\frac{1}{2}\sum_{i=1}^{N}\langle\phi|\Delta_i|\phi\rangle, \tag{3.8}$$

$$E_{ne} \;=\; -\sum_{i=1}^{N}\langle\phi|\sum_{k=1}^{A}\frac{Z_k e^2}{|\mathbf{R}_k - \mathbf{r}_i|}|\phi\rangle, \tag{3.9}$$

$$E_{ee} \;=\; \sum_{i=1}^{N}\sum_{j\rangle i}^{N}\langle\phi|\frac{e^2}{|\mathbf{r}_i - \mathbf{r}_j|}|\phi\rangle. \tag{3.10}$$

Since the involved operators are all linear and the one-electron states build an orthonormal basis it can be shown, that E_{kin} and E_{ne} can be calculated by the one-electron integrals

$$E_{kin} = -\frac{1}{2\sqrt{N!}} \sum_{i=1}^{N}\sum_{j=1}^{N} \langle\varphi_j(\mathbf{r}_i)|\Delta_i|\varphi_j(\mathbf{r}_i)\rangle, \tag{3.11}$$

$$E_{ne} = -\frac{1}{\sqrt{N!}} \sum_{i=1}^{N}\sum_{j=1}^{N} \langle\varphi_j(\mathbf{r}_i)| \sum_{k=1}^{A} \frac{Z_k e^2}{|\mathbf{R}_k - \mathbf{r}_i|}|\varphi_j(\mathbf{r}_i)\rangle. \tag{3.12}$$

For the electron-electron term E_{ee} one obtains the two-electron integral

$$E_{ee} = \frac{1}{2\sqrt{N!}} \sum_{i=1}^{N}\sum_{j=1}^{N}(J_{ij} - K_{ij}), \tag{3.13}$$

with

$$J_{ij} = \sum_{k=1}^{N}\sum_{l=1}^{N}\langle\varphi_i(\mathbf{r}_k)\varphi_j(\mathbf{r}_l)|\frac{e^2}{|\mathbf{r}_k - \mathbf{r}_l|}|\varphi_i(\mathbf{r}_k)\varphi_j(\mathbf{r}_l)\rangle, \tag{3.14}$$

$$K_{ij} = \sum_{k=1}^{N}\sum_{l=1}^{N}\langle\varphi_i(\mathbf{r}_k)\varphi_j(\mathbf{r}_l)|\frac{e^2}{|\mathbf{r}_k - \mathbf{r}_l|}|\varphi_i(\mathbf{r}_l)\varphi_j(\mathbf{r}_k)\rangle. \tag{3.15}$$

Here J_{ij} and K_{ij} are the coulomb and the exchange integrals, respectively. In order to calculate the ground state of the system one has to minimize the functional $E(\phi)$ by variation of the electronic wave functions. Applying the *method of Lagrange multipliers* θ_{ij}, the additional constraint to the energy variation is the orthonormal character of the electronic wave functions $\langle\varphi_i|\varphi_j\rangle = \delta_{ij}$, leads to the so called *Hartree-Fock equation*:

$$\hat{f}|\varphi_i(\mathbf{r}_1)\rangle = \sum_j \theta_{ij}|\varphi_j(\mathbf{r}_1)\rangle \tag{3.16}$$

with

$$\hat{f} = -\frac{1}{2}\nabla^2 + V(\mathbf{r}) + \sum_j \hat{\mathcal{J}}_j + \sum_j \hat{\mathcal{K}}_j$$

and

$$\hat{\mathcal{J}}_j|\varphi_i(\mathbf{r}_1)\rangle = \sum_j \langle\varphi_j(\mathbf{r}_2)|\frac{1}{r_{12}}|\varphi_j(\mathbf{r}_2)\rangle|\varphi_i(\mathbf{r}_1)\rangle$$

$$\hat{\mathcal{K}}_j|\varphi_i(\mathbf{r}_1)\rangle = \sum_j \langle\varphi_j(\mathbf{r}_2)|\frac{1}{r_{12}}|\varphi_i(\mathbf{r}_2)\rangle|\varphi_i(\mathbf{r}_1)\rangle.$$

$\mathbf{r}_1$ and $\mathbf{r}_2$ are the electron coordinates and r_{12} the distance between the interacting electrons. Since the Fock operator $\hat{f}$ is hermitian, one can find a suitable

transformation $\{\varphi_1, ..., \varphi_N\} \rightarrow \{\varphi'_1, ..., \varphi'_N\}$ so that Eq. (3.16) can be written as the so-called *canonical Hartree-Fock equation* in form of a (pseudo)-eigenvalue equation:

$$\hat{f}|\varphi'_i\rangle = \epsilon_i|\varphi'_i\rangle. \tag{3.17}$$

Here the diagonal matrix elements ϵ_i can be regarded as single orbital energies. $\hat{f}$ depends on φ_i so that Eq. (3.17) has to be solved (iteratively) in a self-consistent way (SCF-method). Usually a linear combination of atomic orbitals are taken as a representation of the single $\varphi_i(\mathbf{r}_j)$, leading to the *Roothaan-Hall* equation. For the minimization of the total energy the corresponding linear coefficients are varied in this case.

Since we started from a wave function which does not consider any electron correlation this aspect is completely neglected here. The electron correlation leads to a lowering of the total energy, so that the algorithm presented above, will give an energy above the exact ground state energy. This limit for the approximation of the ground state is referred to as the *Hartree-Fock* limit. The deviation of the calculated energies from the exact ones is about 1 eV. To account for the correlation effects, effort has been made to develope so called *post-Hartree-Fock* methods, using, *e.g.*, the extension of the wave function (Configuration Interaction) or an extendet Hamilton operator (Coupled Cluster or Møller-Plesset perturbation theory). All these methods require extensive calculation effort.

3.2.3 Density functional theory

A more versatile method is based on describing an ensemble of N electrons by its charge density, while regarding two theorems formulated by and named after Walter Kohn and Pierre Hohenberg [34].

(1) It was shown that the electronic state Φ and the charge density n are coupled by a bijective function:

$$f \circ \Phi(\mathbf{r}_1, ..., \mathbf{r}_N) \rightarrow n(\mathbf{r}). \tag{3.18}$$

Thus the expectation value of the Hamilton operator and its summands (except the kinetic energy) can be written as functionals of n so that equation (3.6)

can be rewritten as:

$$\begin{aligned} E = E_{KS}(n) =& \langle \Phi(n) | \hat{\mathcal{H}} | \Phi(n) \rangle \\ =& \sum_i \langle \varphi_i | -\frac{1}{2}\nabla^2 | \varphi_i \rangle \\ &+ \int n(\mathbf{r}) V_K(\mathbf{r}) d\mathbf{r} + \iint \frac{n(\mathbf{r}) n(\mathbf{r}')}{|\mathbf{r}-\mathbf{r}'|} d\mathbf{r} d\mathbf{r}' + E_{XC}(n(\mathbf{r})) \end{aligned} \tag{3.19}$$

with

$$n(\mathbf{r}) := \sum_i \varphi_i^*(\mathbf{r}) \varphi_i(\mathbf{r}), \tag{3.20}$$

where $E(n)$ is the total energy and $V_K(\mathbf{r})$ the nuclear potential. An additional term E_{XC} appears, which describes the contribution of exchange and correlation effects to the total energy.

(2) It was proven that the charge density of the ground state can be calculated by the minimization of the system's total energy. The variation $\delta E_{KS}(n)$ of this total energy functional leads in analogy to Eq (3.17) to the so-called *Kohn-Sham equation*:

$$[-\frac{1}{2}\nabla^2 + V_{eff}(\mathbf{r})]\varphi_i(\mathbf{r}) = \epsilon_i \varphi_i(\mathbf{r}) \tag{3.21}$$

with

$$V_{eff}(\mathbf{r}) = V_K(\mathbf{r}) + \int \frac{n(\mathbf{r}')}{|\mathbf{r}-\mathbf{r}'|} d\mathbf{r}' + \underbrace{\frac{\delta E_{XC}}{\delta n}}_{V_{XC}}, \tag{3.22}$$

which has to be solved again self-consistently. Here V_{eff} depends only on the entire electron density. The two-electron integrals used for solving the Hartree-Fock equation are eliminated, which leads to a more efficient solution of the quantum-chemical problem. The influence of exchange and correlation effects on the electron density are contained in E_X and E_C, respectively. Since those fuctionals are not know, adequate assumptions have to be made.

Descriptively spoken the exchange correlation term introduces a *Coulomb hole* into the effective potential energy term that affects each electronic state φ_i in Eq. (3.20) by attractive forces. Becke used empirical parameters to fit the exchange term in order to get the right correction for the exchange interactions. The calculations presented in this work, are based on density-functional theory (DFT) in combination with gradient-corrected exchange/correlation functionals due to Perdew, Burke, and Ernzerhof (RPBE) [35, 36]. The corresponding

algorithm is implemented in the StoBe code, that was used for all quantumquemical calculations, including the simulation of NEXAFS spectrac as explained in Sec. 3.3.

3.2.4 Molecular orbital representation

A question of fundamental importance is how to choose the proper basis set for $|\varphi_i\rangle$ in order to describe the electronic ensemble. In a general approach that was suggested by Clemens C. Roothaan [37] and George G. Hall the single-electron wave functions are generated by a linear combination of all contributing atomic orbitals χ_j:

$$|\varphi_i\rangle = \sum_j \alpha_{ij} |\chi_j\rangle. \tag{3.23}$$

The variation of $E(n(\Phi))$ is then carried out by variing the expansion coefficients α_{ij}, and the non-linear (pseudo)-eigenvalue equation (3.20) is transformed into a system of linear equations.

Since the handling of pure atomic orbital functions χ_j is rather complicated, a simplification is commonly used in the community of quantum chemistry. It is given by the representation of the atomic wave functions χ_j by linear combinations of a set of **p**rimitive **G**aussian **T**ype **F**unctions (**pGTF**):

$$\chi_j(\mathbf{r}) = \sum_k \beta_{jk} r_x^l r_y^m r_z^n e^{-\alpha_k \mathbf{r}^2} \; with \; \mathbf{r} = (r_x, r_y, r_z). \tag{3.24}$$

Here β_{jk} and α_k are the parameters that form the individual pGTFs. The sum $l + m + n$ corresponds to the azimuthal quantum number (or quantum number of the angular momentum) of the orbital that is being constructed, and assigns the number of orbital nodes. Of course, a single pGTF hardly resembles the shape of an individual atomic orbital. Thus a set of pGTFs is usually combined to represent the corresponding electronic state. These sets are called **C**ontracted GTF (**CGTF**). In this sense one still follows the idea of constructing molecular orbitals from a **L**inaer **C**ombination of **A**tomic **O**rbitals (**LCAO**) while AOs now just means CGTFs.

In the easiest case, all CGTF sets are given by a minimal number of pGTFs needed to describe the atomic orbital (minimal basis set). The electronic valence states and thus their representation by the corresponding valence orbitals are pivotal for the description of the chemical state. Thus, the contributing outer atomic orbitals are generated separately each with an own set of GTFs. The resulting so called *split-valence* basis sets provide a more versatile modeling of the molecular orbitals. In order to further account for the properties

of molecular orbitals like polarization and diffusive shape, the CGTFs that represent the atomic orbitals are supplemented by additional pGTFs. For the polarization, *e.g.*, a GTF with a higher value $l + m + n$ is used to deform the atomic orbital in a certain direction. The delocalized character of a wave function is described by including terms with smaller α_k values in order to form a specific tail.

In the present work sets of CGTFs are use to represent ground states as well as final states for carbon and nitrogen core electron excitations. The so-called all-electron triple-zeta valence plus polarization (TZVP) basis sets can be applied to all second-row elements [38]. Here the designation of the CGTF's configuration is usually given in the notation of Huzinaga:

$$(n(s1)\ n(s2)\ ...\ n(sK)\ |\ n(p2)\ n(p3)\ ...\ n(pL)\ |\ n(3d)\ n(4p)\ ...\ n(Md)).$$

The n signify the number of pGTFs that represent the atomic orbitals. K, L, and M give the quantum number of the highest s, p, and d orbital orbitals, respectively. For carbon, nitrogen, and oxygen orbitals sets of (7111|411|1) configuration were used, and a smaller (3111|111) basis set (double-zeta plus polarization) is used for hydrogen in order to evaluate electronic ground states.

For the simulation of the NEXAFS spectra additional basis set configurations are used. The calculations of the core excited states are carried out using a basis set of all-electron individual gauge for localized orbitals (IGLO-III) quality [39] to represent the excitation center, while the remaining equivalent atomic centers are described by effective core potentials (ECP) [40] approximating the 1s core and corresponding valence basis sets. In addition, a large diffuse even-tempered [19s,19p,19d] basis set was included at the excitation center in order to comprise the unbound states in the core region of the excited atom [41].

3.3 Simulated NEXAFS

Quite often NEXAFS spectra are analyzed by using the so-called building block picture, in which one tries to decompose the entire spectrum and to assign the single contributions to different chemical substructures of the molecule. This, of course, is only valid, if the electronic systems of those substructures are decoupled enough. A more general attempt is based on quantum-chemical calculations which were introduced in the previous chapter. From this we get the initial and the state's total energies and further the transition energies of the core excitations. A key tool for the simulation of NEXAFS spectra is given by equation (2.5) that needs the initial and the final state as an input

and affords the transition intensities. Some technical notes are given in this section.

3.3.1 Ionization potentials

As explained in Sec. 2.1, the electron binding energy is the negative energy needed to separate the electron from the remaining ion or, in other words, the energy that is needed to overcome the potential energy barrier of the ion in which the electron is trapped initially. This ionization energy is given by the difference in total energy between the initial neutral and the final charged state. For both states the total energy can be calculated by applying Slater's determinant with the corresponding occupation schemes to the Kohn-Sham equation. The difference in total energy is thus called ΔKohn-Sham energy.

3.3.2 Transition energies

The transition energy $E_T = E_f - E_i$ (cf. Sec. 2.1) can, in principle, be obtained from the calculation of the total energies E_i and E_f (analog to the determination of the ionization potential with the ΔKohn-Sham method). Consequently, two calculation steps for each electronic transition are needed. A more efficient approach is given by the so called *transition state method* introduced by Slater [42, 43]:

Recalling Koopmans' theorem (introduced in Sec. 2.1) the (initial) orbital energy of the excited electron would correspond to the binding energy E_B if all the non excited electrons remain frozen in the ground state configuration after a single electron excitation. This energy is achieved for all involved orbitals by a (single step!) ground state calculation. The question is now, whether one can get the relaxation effects included in this single step calculation. Following this idea one can expand the total energy as a function of a partial occupation n of the corresponding orbital in a Taylor series and interrupt the expansion after the second order term. This has to be done for both, the initial and the final occupation n_0 and n_1:

$$E(n_0) = E + \frac{\partial E(n)}{\partial n}(n_0 - n) + \frac{\partial^2 E(n)}{\partial n^2}(n_0 - n)^2 + ...$$
$$E(n_1) = E + \frac{\partial E(n)}{\partial n}(n_1 - n) + \frac{\partial^2 E(n)}{\partial n^2}(n_1 - n)^2 + ...$$

The binding energy is then given by the difference $E_B = E(n_1) - E(n_0)$.

Choosing $n = 1/2(n_1 + n_0)$ results in:

$$E_B = \frac{\partial E(n)}{\partial n}\Big|_{n=\frac{n_1-n_0}{2}} (n_1 - n_0). \tag{3.25}$$

With $n_1 = 1$ and $n_0 = 0$ we obtain the binging energy of the corresponding electron by the energy of the half occupied orbital, which can be calculated in a single Kohn-Sham calculation step.

For the calculation of a transition energy one additionally has to occupy the final state orbital in order to get the relaxation effect in the presence of the excited electron in a valence state. Consequently, one has to do a single step calculation of each transition for the entire spectrum (which already reduces the number of steps needed for the ΔKohn-Sham calculation by a factor of two). In order to further reduce the computational effort, one renounces the half occupied valence state and uses the output of the single step Kohn-Sham calculation for the semi occupied core level. The transition energies are then calculated approximately by the difference between the final and the initial orbital energies. The relative energetic distance of the features in the individually simulated NEXAFS spectra of the different core level electrons are found to be in very good agreement with the experimental spectra of various organic molecules. In contrast the absorption spectra for different excitation centers are shifted with respect to each other. The calcuated energy of the unoccupied transition-state orbitals are all affected by the same energy shift, which is corrected by the allignment of the transition state core level to the ΔKohn-Sham ionisation potential. Due to its success in reproducing experimental data, this method is a standard tool to simulate NEXAFS spectra.

3.3.3 Transition intensities

The transition intensities are calculated by assuming a single electron excitation picture and determining the dipole transition matrix elements by *Fermi's golden rule* (Eq. (2.2)) from the intertransitions between the solutions of the transition state calculation. The discrete excitation spectrum obtained by this calculation is processed by a Gaussian convolution of energy-dependent broadening in order to compare the theoretical results with those of the experiment. For transitions below the ionization potential a full width at half maximum (**FWHM**) of 0.6 and 0.8 eV for N and O is applied, respectively, while the FWHM is increased linearly up to 4.5 eV at 10 eV above the IP. Further details of the methods are described in Ref. [44, 45]. The angle-dependence of the NEXAFS simulated evaluating the transition-dipole matrix. For the

angle-averaged spectra the absorption of three orthogonal orientations of the light-polarization vector has to be averaged. It is found that the grazing incidence spectra, measured under 20° X-ray incidence are in best agreement with the calculated spectra for 30°. This may be explained by Fresnel diffraction that appears due to the interaction of the incoming X-ray wave with the electron density at the surface [46].

Chapter 4

Azobenzene on noble metal surfaces

It was already mentioned in the introduction that there are several classes of photoactive chemical compounds that are able to undergo reversible transformations between two or more stable molecular states. These states usually differ, *e.g.*, in their chemical and/or geometric structure. Molecules for which the reversible process is given by a change between different stable geometries while the bond order of each atom is mainly preserved, are referred as to *conformational* switches. The smallest members of this class of molecules are stilbene, diphenylimine, and azobenzene, which simply consist of two benzene rings connected by a C=C, C=N or N=N bridge, respectively (see Fig. 4.1). The involvement of structural changes makes them suitable for the development of, *e.g.*, molecular motors [47], or for the mechanical manipulation of secondary molecules [48, 49]. Conversely, such applications bring the molecular switch into a confinement, where the isomerization process is strongly influenced, not only by mechanical coupling, but also by electronic interaction of the molecule with the environment. This is also the case for molecular switches that are attached to a surface. Several strategies have been attempted in order to incorporate the molecular functionalities to the surface. Recently, the realization of a photoswitchable ensemble of azobenzene molecules fixed via linker/spacer groups to a glass surface has been successfully demonstrated [5]. In contrast, the direct adsorption of conformational switches on a surface can be rather complex. In contrast to gas phase and solution, the degree of freedom is reduced due to adsorbate–adsorbate [50] and adsorbate–surface interactions [12, 16, 51]. Furthermore the latter might lead to a reconfiguration of the electronic system due, e.g., to the hybridization of adsorbate orbitals with those of the surface.

However, it has been demonstrated that for different azobenzene derivatives the isomerization can be triggered by currents induced with a scanning tunneling microscope (STM) tip reversibly on Au(111) [12] and irreversibly on Au(111) [13] and Cu(001) [15]. This is a strong indication, that the isomerization process can still be initiated while the adsorbate interacts with the surface. On Cu(001) the reverse transformation was prevented by the formation of stronger bonds between the azo lone-pair electrons and the substrate. A similar irreversible process including photocyclization was reported for azobenzene in microporous aluminiumphosphate [52]. In both cases the lone-pair electrons at the center of the molecule are more exposed in the bent *cis* geometry and thus easier to access for chemical bond formations. The initial appearance of a stable chemisorbed *trans* state on Cu(001) on the other hand implies the existence of an additional antagonistic interaction that prevents the immediate change to the *cis* conformation during adsorption. An understanding of the interplay of the differend mechanisms might lead to a picture that can help to the concerted manipulation of the adsorbate-substrate system so that the contrary mechanisms might be more balanced.

A complementary study based on x-ray spectroscopic methods in combination with DFT based simlations can help to give a more detailed picture about the interactions in the adsorbate-substrate system. Therefore the influence of the different typs of interactions is studied here by going from the decopled molecules in crystalline powders and evaporated thick films to weakly bonded organic systems on Au(111) and further to chemisorbed molecules on Cu(001). The determination of the adsorbate geometries might help to identify the different adsorbtion states experimatially. Furthermore the extracted electronic structure is espected to give a deeper understanding of the involved bonding mechanisms.

4.1 Photoisomerization of azobenzene

The three biphenylic compounds given in Fig. 4.1 can exist in two different conformational states. The planar *trans* conformation is the most stable one, since only here all the non-hybridized atomic p orbitals can contribute to a fully conjugated molecular π system that is oriented perpendicular to the molecular plane. In contrast, the distance of the two benzene rings in the *cis* conformation is so small that they are forced to tilt against each other. In the resulting non-planar geometry an optimal mixing of the non-hybridized atomic p orbitals is not possible due to symmetry reasons. Thus the *cis* state is higher in total energy and for diphenylimine, and azobenzene metastable at room

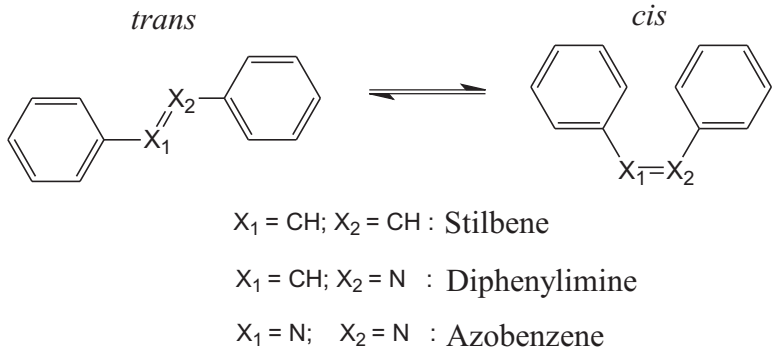

Figure 4.1: *Geometric structure of stilbene, diphenylimine, and azobenzene.*

temperature. The different degree of conjugation causes *inter alia* different physical properties for *trans* and *cis* isomers like, for example, permanent electric dipole moments, polarizability, and conductivity. For all three compounds the different conformers exhibit strikingly different optical absorption spectra. Finally stilbene even changes its aggregate state from the solid (crystalline) *trans* to the liquid *cis* phase due to the suppressed π-stacking capabilities of the *cis* isomer.

The photoisomerization of all three compounds can be understood by looking at the electronic structure of their planar *trans* isomers and using the assumption that the molecular orbitals are formed by the **L**inear **C**ombination of (contributing) **A**tomic **O**rbitals (**LCAO**) as it is shown in Fig. 4.3. The discussion is given exemplarily for azobenzene and can be adopted to the other two compounds.

The entire orbital system of the planar *trans* isomer is described suffi-

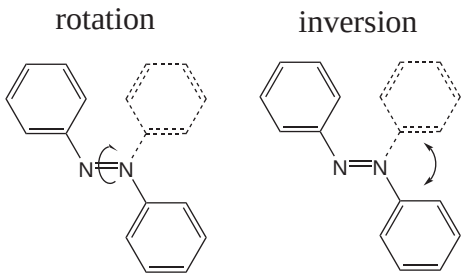

Figure 4.2: *Different transformation pathways for the isomerisation of azobenzene. While the inversion is a quasi-in-plane transformation, for the rotational isomerization the benzene is tilted out of the molecular plane, so that more space is needed for the latter.*

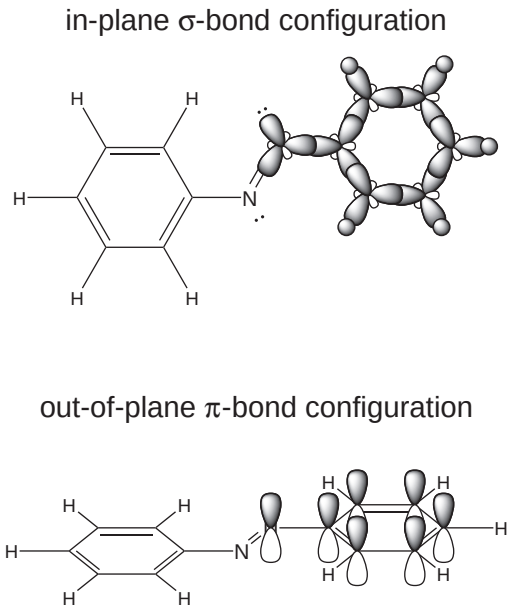

Figure 4.3: *Demonstation of the linear combination of atomic orbitals in trans azobenzene. The sp^2 hybridized carbon and nitrogen atoms form an in-plane σ-bond system (upper panel), while the non-hybridized atomic p-orbitals combine to the out-of-plane π-orbital system (lower panel).*

ciently using *Hückel's* aproximation, in which no interaction between the σ- and the π-bond system is assumed. Here, the orbital systems of all nitrogen and carbon atoms exhibit an sp^2-hybridized character of their valence orbitals where the hybridization lies in the molecular plane. Two sp^2 hybrid orbitals of each atom contribute to the C–C, N–C, and the N–N σ bonds. The third sp^2 hybrid orbital of each carbon atom is saturated by a hydrogen atom whereas the two nitrogen atoms merge theirs to a non-bonding orbital containing two lone pairs of electrons and constituting the **H**ighest **O**ccupied **M**olecular **O**rbital (**HOMO**), as it is shown in Fig. 4.4.

The remaining non-hybridized atomic p orbitals have all the same symmetry and merge to one complete π system containing seven occupied π orbitals and seven empty π^* orbitals. The π^* orbital with the lowest orbital energy is the **L**owest **U**noccupied **M**olecular **O**rbital (**LUMO**) which is also given in Fig. 4.4. These orbitals, usually referred to as *frontier orbitals*, are located around the Fermi level with a comparably small energetic distance so that optical excitations are possible.

For azobenzene the frontier orbitals have a sizable contribution at the center of the molecule, where the chemical bonds are strongly involved in the isomerization processes (compare Fig. 4.2). For the rotation, *e.g.*, the HOMO-1 π orbital has to be separated into the two contributing atomic nitrogen p orbitals until they can mix again after a rotation of 180°. Furthermore, the two atomic sp^2 contributions of the non-bonding HOMO orbital have to decouple

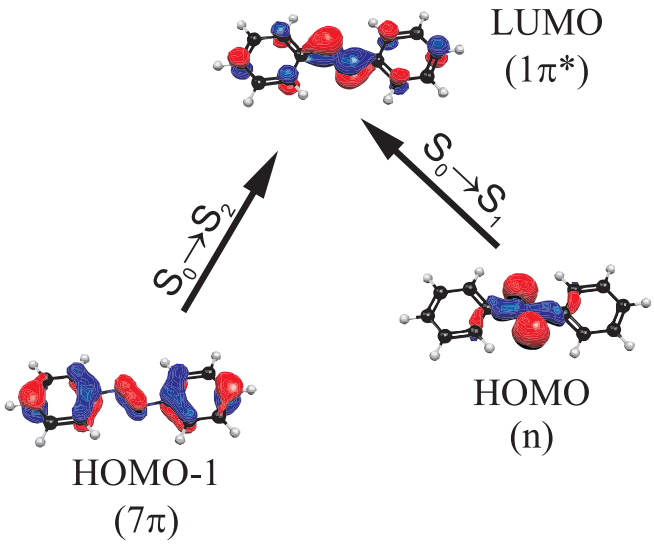

Figure 4.4: *Frontier orbitals of azobenzene. The excitation from the HOMOs into the LUMO are represented by the black arrows, where the excitation from HOMO to LUMO gives the first excited state S_1 and the transition from the HOMO-1 to the LUMO results in the second excited state S_2. S_0 indicates the initial ground state.*

for the same reason. This bond segregation process cost energy of about 1.6 eV for the *trans* state and 1 eV for the *cis* conformer [53]. The total energy of the molecular ground state S_0 is given as the lowest **P**otential **E**nergy **S**urface (**PES**) in dependence on all the N=N rotation and N=N-C inversion angles in Fig. 4.5, Ref. [54]. The minima in the corners of the S_0 PES correspond to the *trans* and *cis* conformations. Both pathways, the N=N rotation for a N=N–C inversion angle of 120° and the N=N–C inversion for a N=N rotation angle of 0° are marked with the straight lines at to bottom of the figure. In the S_0 state a maximum separates the two isomeric states on both reaction paths.

The electronic excitation from the HOMO to the LUMO results in the first excited singlet state S_1 for which the PES is given as the middle one in Fig. 4.5. For this excitation the non-bonding HOMO donates an electron to the antibonding LUMO. The resulting LUMO occupation leads to the destabilization of the central N=N double bond, since the contributing atomic N p_z orbitals repulse each other. As can be seen in the S_1 PES, both, the *trans* and *cis* isomer, have an unstable geometry, while the global minimum of the PES is at a rotation angle of 90° around the azo N–N bond. This global minimum is also the point in the phase diagram with the smallest distance between the PES of S_0 an S_1. The electronic decay form the S_1 state will start at this global minimum for a fixed geometry to a local energy maximum in the S_0-PES at the rotation path between the *trans* and *cis* geometries. The subsequent vibronic decay starts from this energy maximum between the local minima of *trans* and *cis* conformations, it can go toward both states. For an S_1 excitation wave length of 316 nm the isomerization yield is around 25% starting from the *trans*

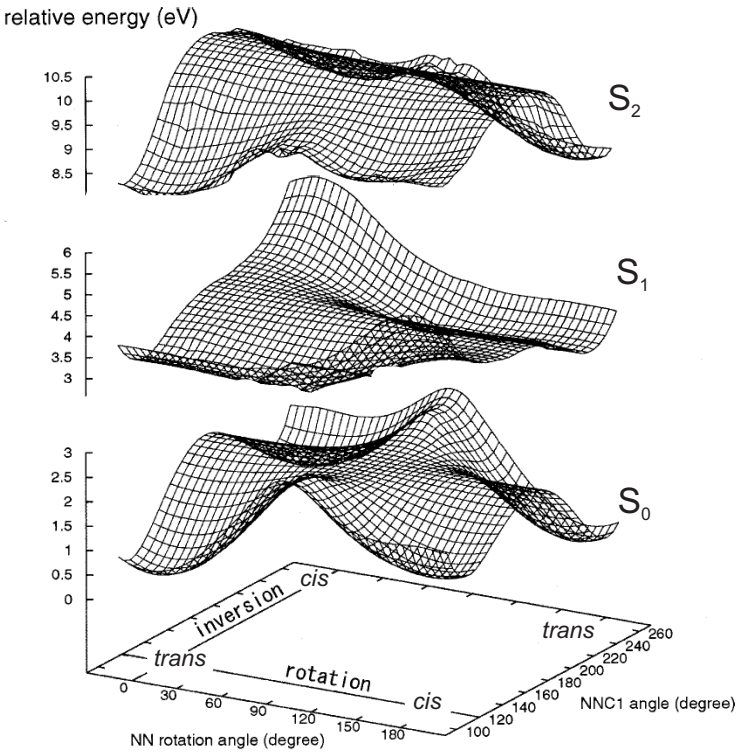

Figure 4.5: *Calculated potential energy surfaces for the trans ⇌ cis transformation for the two different pathways (inversion, rotation) for the ground (S_0) and the two lowest excited states (S_1 and S_2), taken from Ref. [54].*

isomer and around 50% from the *cis* state [55]. For the excitation into the second singlet state S_2 the isomerization yields differ from those of S_1, which is in contradiction to Kasha's rule[1] [56]. There is an ongoing discussion about whther the decay mechanisms are explaind by so called phantom states [57] or by the decay via a concerted-inversion pathway [58]. In view of the higher extinction for the S_2 excitation, this exotic transformation behaviour might open a different way to tune switching probabilities and to further use them for new functional materials.

However, the isomerization strongly depends on the electronic configuration at the center of the azobenzene molecule. Although at a first glance, the *trans* and the *cis* conformations of stilbene, diphenylimine, and azobenzene appear to be quite similar, the electronic structures vary due to the different valences of carbon and nitrogen at the molecular centers. While for nitrogen a lone pair is present in the non bonding sp^2 orbital, for carbon the spare unpaired electron has to be saturated by an additional hydrogen. This imparts on the molecular centers a different reactivity regarding specially the

[1]Kasha's rule predicts the an optical deexcitation always starts from a lowest excited electronic state

possibility of coodinative bond formation. Nevertheless the different chemical environment influences also the internal electron distribution, finally leading to different transformation behaviors, to different light absorption in the UV-vis regime and further to the fact that only stilbene is thermally stable in both conformations at room temperature. In contrast, diphenylimine and azobenzene *cis* isomers reverse by thermal activation into the *trans* state with typical life times in the range of seconds and hours, respectively. Furthermore, from the two isomerization pathways (sketched in Fig. 4.2) that were observed for azobenzene [59], stilbene can only follow the rotation path due to the presence of the saturating hydrogen [57]. The adsorption of unsubstituted stilbene on semiconductor and metallic surfaces was recently reported two years ago, where the molecules turned out to rather physisorb on the Cu(110) surface [51]. In contrast, azobenezene was found to undergo a current-induced irreversible *trans* $\rightarrow$ *cis* transformation on Cu(001), leading to a coordinative bond formation via the lone pair electrons of the azo center to the substrate [15]. It is obvious that there exists a high flexibility already due to small changes in the system *organic switch – metallic substrate* in tuning the corresponding interactions and thus the photoactive properties. In the following sections a spectroscopic study of azobenzene is presented and discussed in the light of those previous results.

4.2 Azobenzene derivatives

Azobenzene has been synthesized the first time already in the early 19th century by E. Mitscherlich [60]. At the latest from the discovery of its photochromic properties there has been a concentrated effort in organic chemistry to produce innumerable derivatives for most diverse purposes. This was motivated, *e.g.*, by the attempt to tune the isomerization process, either electronically by adding electron donor and acceptor groups or mechanically as it was achieved for azobenzenophanes or azobenzene-chrownethers in polymer matrices. Another demand of customized derivatives comes from the integration of the molecular switch into a certain chemical environment like organic polymers and crystals [61], Langmuir-Blodgett films [62] or on surfaces [63] in order to produce novel functionalized materials.

In chemical physics the functional groups can serve as indicators for certain chemical states. In thissense two different azobenzene derivatives are used in this work in order to obtain information about the adsorption behavior of azobenzene on metallic surfaces. Therefore, the functional groups should not disturb the central frontier orbital system in order to preserve the original prop-

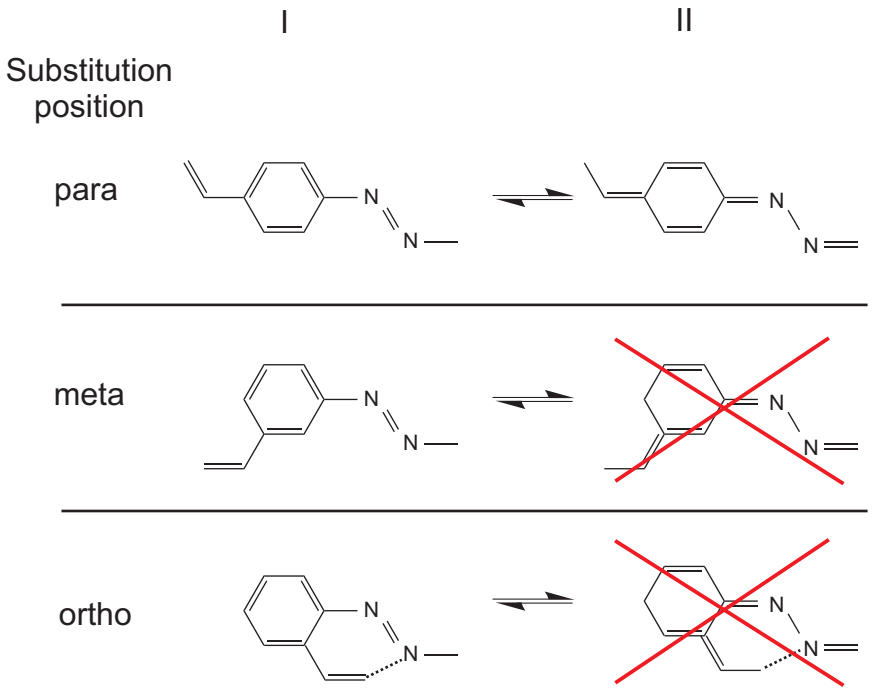

Figure 4.6: *Mesomerism of azobenzene with substituent in para, meta, and ortho position. The different resonance contribution are labeled as I and II. The red crosses indicate that the formation of structure II is forbidden for meta and ortho position. The dotted line between the sustituent and one azo nitrogen in the ortho substituted structure indicates a possible interaction between both.*

erties of the azobenzene unit. This can be achieved by attaching rest groups in *meta* or *ortho* positions. In this case mesomeric effects in the frontier π orbital system are suppressed [64] in the way as it is illustrated in Fig. 4.6. A coupling to the π orbitals of the azo center to the substituent is thus impossible. Depending on the character of the rest group, in *ortho* position there may appear repulsive forces (indicated as a dotted line in Fig. 4.6) from the azo center that push the benzene out of the molecular plane. Thus the *meta* position is the preferred substitution place. 3,3'-cyano-azobenzene (dimetacyano azobenzene (DMC)) and 3,3'-carboxymethylester (CMA) azobenzene are chosen. Both compounds were synthesized in the group of Prof. Rück-Braun [65]. They are expected to yield complementary information by X-ray absorption and photoelectron spectroscopy from the azo center and the rest groups about the adsorption state on metallic surfaces, as it will be discussed in the following two sections.

4.2.1 Dimetacyano azobenzene

The chemical structure of dimetacyano azobenzene (DMC) is given in Fig. 4.7. Two benzonitrile subunits are connected via a N=N azo bridge such that the corresponding C≡N cyano rest groups are found in *meta* position. Since the frontier orbital systems of the azo center and of the rest groups can be regarded as decoupled, a short introduction will be given into the electronic system of the cyano and benzonitrile subunits in addition to the one of azobenzene (*cf.* Sec. 4.1).

The orbital configuration of the cyano group is given in Fig. 4.8. Assuming the C≡N bond axis along z direction, the two p_z orbitals will overlap to a large extend and form a the bonding 5σ and the anti-bonding $6\sigma^*$ orbitals. Due to the rotational $C_{\infty v}$ symmetry around the bond axes, the p_x and p_y states are degenerate and together form a bonding 1π and an anti-bonding $2\pi^*$ state that consist each of two orthogonal orbitals. A vacant electronic state in the HOMO causes the cyano group to be a radical which exhibits a strong electron-accepting character. Since the original N $2p$ orbital is lower in energy than the one of carbon, the electronic charge shifts toward the nitrogen side, causing a permanent dipole moment.

When considering the benzonitrile moiety, the rotational $C_{\infty v}$ symmetry of the C≡N group as well as the C_{6h} symmetry of the six-membered carbon ring are reduced, so that the irreducible representation of the corresponding orbitals has to be rewritten in terms of the C_{2v} point group as given in Fig. 4.9. In the C_{2v} notation, the two degenerate HOMOs of the benzene are of different symmetry in the same manner as those of the cyano group. Since for the coupling of two orbitals their symmetry has to be the same, only the benzene B_2 and the cyano π_x orbital can mix and form the bonding $2B_2$ and the antibonding $3B_2$ benzonitrile orbitals. The other two orbitals remain in their original form. The same happens to the LUMO configuration as shown in the top part of Fig. 4.9. Consequently, benzonitrile exhibits two orthogonal frontier π^* orbitals ($6\pi^*$ and $8\pi^*$) located at the cyano nitrogen atom where the $6\pi^*$ stands perpendicular to the benzene plane and the $8\pi^*$ is parallel to

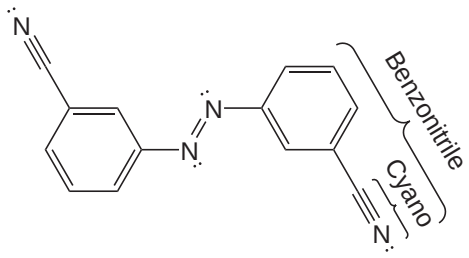

Figure 4.7: *Chemical structure of dimetacyano azobenzene (DMC) with labeled subunits as they are referred to as in the text.*

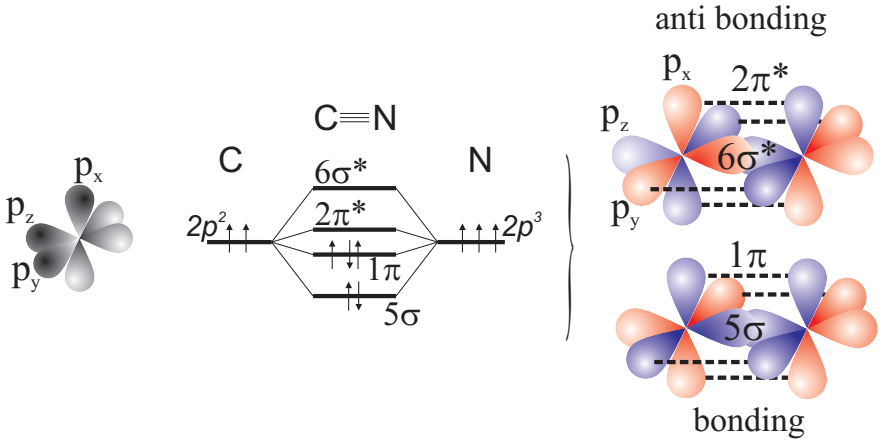

Figure 4.8: *Bond configuration of the cyano group with the C≡N bond axis defined along the z axis. The left hand side shows the configuration in the valance state picture where the three atomic 2p states of carbon and nitrogen split into two bonding and two antibonding states. At the right hand side the development of the molecular orbitals is given by the interaction of atomic π orbitals.*

it. Both orbitals are separated in energy, as it was observed by NEXAFS spectroscopy [66] where the corresonding resonances have been found to differ by 1 eV. Thus, by means of angle dependent X-ray absorption studies, the orientation of both molecular orbitals can be determined easily. As will be shown in detail in Sect. 4.3.2.6, these orientations can be used to gain detailed information about the adsorption geometry of azobenzene.

atom		partial el. charge	nuclear charge	ionicity
cyano	N	-7.226	7.000	-0.226
	C(≡N)	-5.998	6.000	0.002
phenyl	C_1(-C≡N)	-5.862	6.000	0.138
	C_2	-6.163	6.000	-0.163
	C_3	-6.163	6.000	-0.163
	C_4	-6.147	6.000	-0.147
	C_5	-6.163	6.000	-0.163
	C_6	-6.163	6.000	-0.163

Table 4.1: *Atom ionicity of benzonitrile from Mulliken population analysis based on DFT. All numbers are given in units of the elementary charge e.*

In benzonitrile the vacant electronic state of the cyano moiety is partially

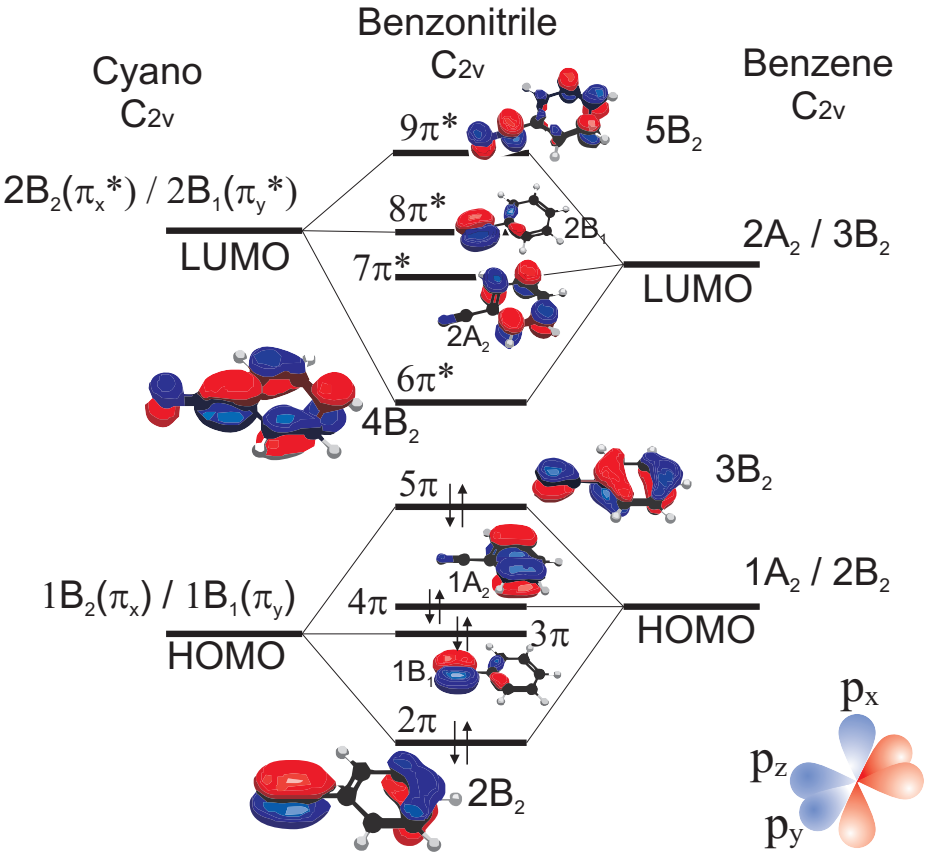

Figure 4.9: *Bond configuration of benzonitrile resulting from the orbital overlap of the HOMOs and LUMOs of benzene and the C≡N cyano group. All orbitals are given in the irreducible representation of the C_{2v} symmetry group in order to understand the specific combination of selected orbitals. Blue and red colors indicate the negative and positive contributions of the atomic wave functions, respectively.*

filled by contributions from the benzene ring. Thus the cyano carbon is almost neutral, while the benzene carbon at the substitution position is charged positively. This can be seen from the *Mulliken* population analysis which is based on DFT calculations and shown in Tab. 4.1. Here, the cyano nitrogen is found to be the most negatively charged atomic site with almost one quarter of an elementary charge. The calculated charges of the remaining phenylic carbon sides are close to -0.146 e, calculated for the carbon atom of unsubstituted benzene with the same computational method. In the latter case, the negative charge is donated by the neighboring hydrogen.

For DMC, two benzonitrile subunits are connected via an azo bridge. The

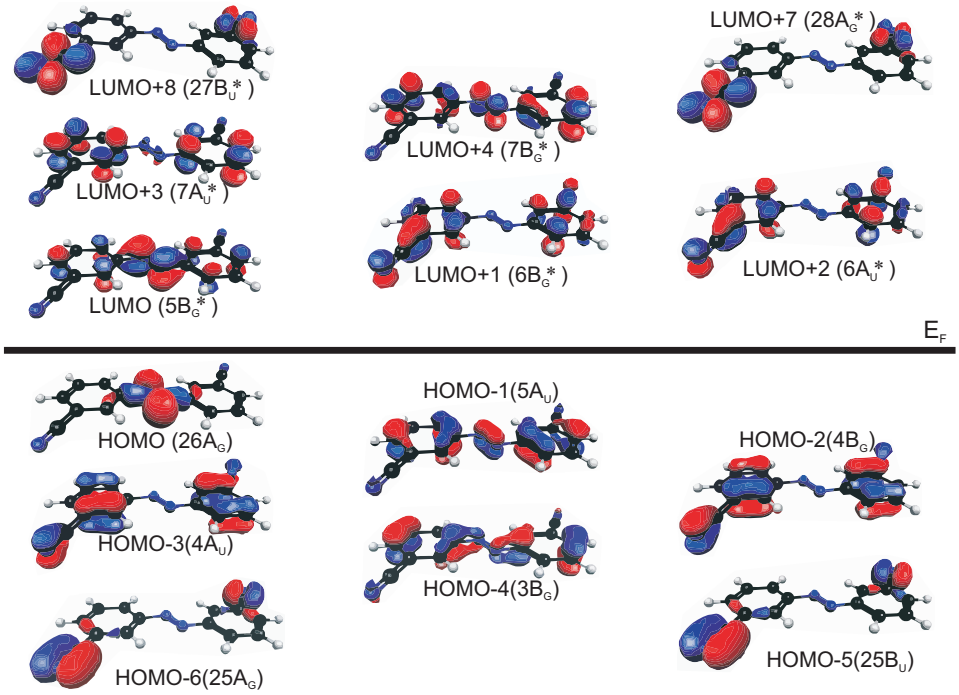

Figure 4.10: *Selected frontier orbitals from the ground state calculation of the trans DMC molecule. The horizontal position denotes the energetic position of the orbital. The labels are given by the order of appearance with their HOMO/LUMO index as well as in the irreducible representation of C_{2h} symmetry in brackets.*

corresponding population analysis gives almost the same charge distribution for the cyano rest groups as in the isolated benzonitrile. In the center of the molecule only a slight charge transfer of -0.070 e toward the azo nitrogen is observed while the neighboring carbon atoms carry only a small positive charge of 0.096 e. The same values are found for unsubstituted azobenzene. The different chemical environments at the center and the outer regions of DMC are expected to cause a different chemical shift in XPS as it was discussed in Sec. 2.1.1.

The eighteen contributing atomic $2p_x$ orbitals in *trans* DMC form a π_x system of nine occupied and nine unoccupied molecular orbitals that are perpendicular to the molecular plane. Additionally four atomic p_y orbitals (two of each rest group) form an in-(molecular-)plane π_y orbital system that is only located at the rest groups. A selection of the important molecular orbitals is given in Fig. 4.10. Since the structure of *trans* DMC exhibits C_{2h} symmetry, the out-of-plane π_x orbitals are either A_u for those that have no orbital node in the center of the molecule, or B_g for the orbitals that are inversion-invariant.

The π_y orbitals and the orbitals that form the σ network are of the same type of symmetry and share the indexing in the irreducible representation. The shape of the DMC HOMO and of the HOMO-1 as well as the one of the LUMO are the same as those of the LUMO of azobenzene (*cf.* Fig. 4.4). Since they all have a node a the *meta* position, the cyano π system cannot couple to the azo frontier orbitals. Thus the formation of new pairs of bonding/antibonding molecular orbitals at different energy positions is suppressed, and the original LUMOs of azobenzene and benzonitrile remain unchanged in the presence of intra-molecular bond formation.

Since at the azo center neither a charge transfer nor a change of the electronic configuration is found to be caused by the cyano rest groups, the switching mechanism which depends on the frontier orbital configuration should not be influenced by the substituted rest groups either. This is consistent with the predicted effect of the suppression of mesomerism that was discussed in the frame of valence bond theory earlier in this section (*cf.* Fig. 4.6).

Concerning the investigation of the interaction of DMC with its chemical environment, the resulting localization of the decoupled frontier orbitals can help to answer the question of which part of the molecule is involved in possible chemical processes. For this purpose one has to use measurement techniques that are able to probe separately the different orbitals. Core-level spectroscopies (XPS, NEXAFS) offer this possibility, since the direct transition from localized core excitation centers are scanned by this method. XPS in particular is sensitive to changes of the local chemical environment around the excitation center (*cf.* Sec. 2.1.1) including variations of the localized frontier orbitals. Angle dependent NEXAFS gives further information about the orientation of the LUMOs and their energetic positions, since the corresponding electronic states are probed by this technique (*cf.* Sec. 2.2.2).

The N K-shell NEXAFS of a DMC powder sample pressed on an indium foil is shown as the upper spectrum in Fig. 4.11. Due to the thickness of the powder film of about 0.1 mm no absorption signal is expected from the molecule-metal interface, since the penetration depth of soft X rays is less than 500 nm. Since the molecular orientation in the powder is random so that the total cross sections of all present transitions in this spectrum can be compared, even though the probing x-ray light was linearly polarized parallel to the plane of the indium foil. In the region between 386 eV and 402 eV two pronounced features are visible. Both can be assigned to electronic transitions from the N 1s core level to the DMC LUMOs. Since the azo and the cyano LUMOs are not interfering, one would expect the convolution of a pure azobenzene NEXAFS spectrum with that of benzonitrile. The NEXAFS that was measured for

benzonitrile shows resonances at about the same energetic positions as the ones in the present spectrum, where the resonance at lower energies was found to be narrower [66]. Thus the broad resonance at 398.8 eV can be regarded as containing two transitions, one from the azo N 1s level to the azo LUMO, and the second from the cyano N 1s level to the cyano LUMO. The corresponding transitions-state orbitals are plotted in Fig. 4.11.

At photon energies above 400 eV, broader features appear in the experimental NEXAFS. These resonances are due to transitions from the core levels into unbound states beyond the ionization barrier. Since those states are only trespassed during the ionization process, the corresponding occupation life time is much shorter compared to that of the binding π^* states. Thus the full width half maximum (FWHM) of the related so-called σ shape resonance is much bigger (*cf.* Sec. 2.2.1).

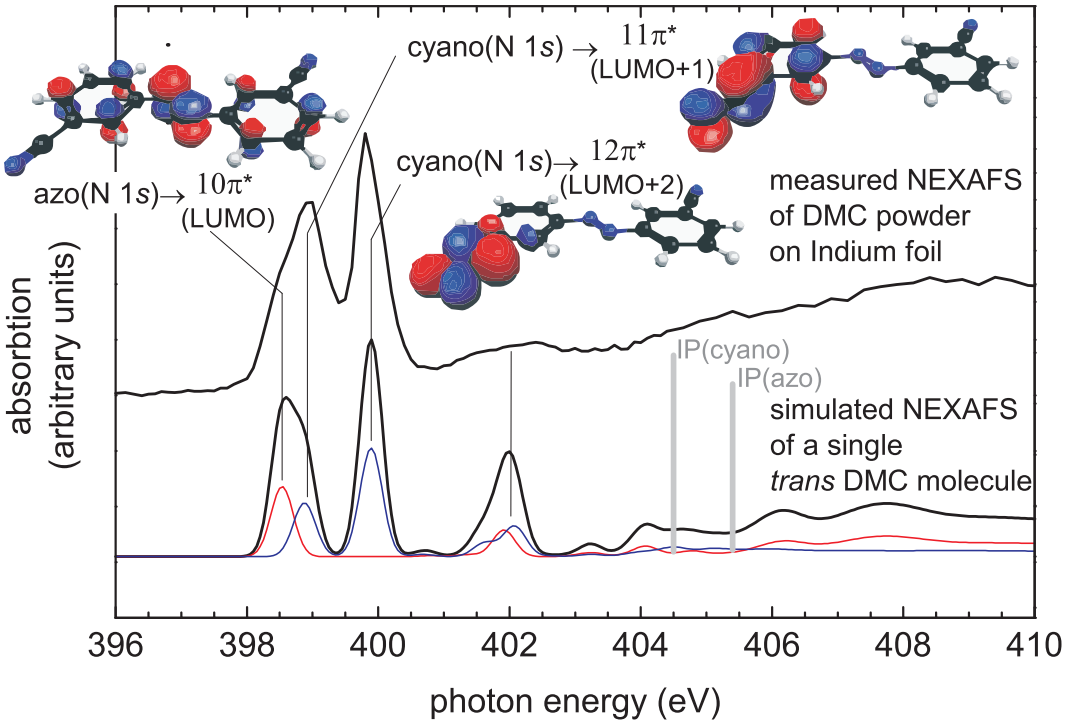

Figure 4.11: *Upper spectrum: N K-shell NEXAFS of DMC powder pressed on an indium foil. Lower spectrum: simulated N K-shell NEXAFS of a single free trans DMC molecule. Red and blue components belong to the partial absorption at the azo and the cyano N 1s excitation centers, respectively. The two gray vertical lines mark the corresponding ionization potentials. The given orbitals belong to the calculated transition states.*

Theoretical considerations are further used in order to support the experimental findings. Assuming that the molecules are only weakly bond in the crystalline confinement, mainly by π stacking/physisorption, an isolated DMC molecule can be taken as a model system. All single calculation steps are based on DFT. A preliminary geometry optimization of DMC was carried out starting from the coordinates that were found for azobenzene and benzonitrile in literature [67, 68]. Thereby the resulting bond lengths vary only less than 0.02 Å from the given data. The calculated geometry was thus used as an input for all subsequent calculations as, *e.g*, for the simulation of the NEXAFS spectrum that was carried out on the base of the transition state method described in Sec. 3.3.2. The discrete excitation spectrum obtained by these calculations was processed by a Gaussian convolution of energy-dependent broadening in order to compare the theoretical results with those of the experiment (further details see below in the text).

The corresponding calculated N K-shell NEXAFS spectrum of a single DMC molecule is shown as the lower black graph in Fig. 4.11, and exhibiting a good agreement with the experimental data. The red and the blue spectra correspond to the partial absorption of the azo and the cyano N 1s excitation centers, respectively. Three π^* resonances are visible below 400 eV. Since all frontier orbitals are localized either around the azo or the cyano N 1s excitation centers, each of the three resonances corresponds to a different final state orbital given as insets in Fig. 4.11. The first is related to the transition of the azo N 1s core level electrons into the DMC LUMO as it was presumed from the order of orbitals found in the ground state calculations. The second transition state orbital is located only at the rest group at which the excitation takes place. Thus it is different to all orbitals found for the ground state calculation (*cf.* Fig. 4.10). The latter are either of A_U or B_G symmetry in the C_{2h} notation. For the transition state the core hole breaks this symmetry and shifts the orbital energy at the excitation center such that the contributing benzonitrile orbitals segregate. Additionally the splitting of the energy levels in the bonding and antibonding states is suppressed. All together this leads to the energetic reordering of electronic states. As an example, the DMC ground state LUMO+7/8 is shifted to lower energies and positioned closer to the cyano N 1s transition state LUMO+2/3.

A general remark should be included here, since it concerns a prevalent problem of the correct assignment of the individual spectral features in NEXAFS spectrocopy to the transitions into corresponding final state orbitals. In the case that the frontier orbitals have a localized character, as for meta-substituted azobenzenes, the core-hole-induced shift in energy will be stronger

for those orbitals that are more concentrated around the excitation center. A sufficiently different shift will furthermore cause a change of the energetic order as it has been seen, *e.g.*, for the N 1*s* core level excitation at the cyano rest group. This effect is even stronger for the C=O oxygen core level excitation in CMA (*cf.* Sec. 4.2.2). The applied transition state method takes this effect appropriately into account and is therefore suitable as theoretical description. In contrast, an interpretation of experimental NEXAFS spectra on the base of ground state calculations has to be conducted with care.

An artificial broadening (*cf.* Sec. 3.3.3) with a **F**ull **W**idth at **H**alf **M**aximum (**FWHM**) of 0.35 eV was applied to the discrete transitions in the simulated NEXAFS below the ionization barrier, since the experimental resolution was estimated to 0.3 eV and the natural line width for a N 1*s* core level excitation is know from literature to be around 0.1 eV [25]. Despite this broadenings, the resonances appear to be much broader in the experimental data. A closer inspection of the LUMO+2 resonance reveals its asymmetric shape. This is caused by a vibrational broadening of the main transition lines of benzonitrile [69] which is not considered in the present calculations. While only one pronounced vibrational mode was found that modulates the resonance coupled to the LUMO+2 transition, the LUMO+1 transition splits into several resonances. Thus a single-peak fit for each transition will not be sufficient, since the regime of vibrational resolution is already reached in the present experiment.

The two different ionization potentials of the azo and the cyano N 1*s* core levels are found at 404.5 eV and 405.5 eV for the azo and the cyano N 1*s* core electrons, respectively. Thus the region of the σ shape resonances does not include the broad feature that is visible at around 402 eV. From the calculation these resonances can rather be assigned to the N $1s \rightarrow \pi^*$ transitions, *i.e.* into a bonded state. Hence the broadening is not caused by the unbonded character of the final state. It might be the quenching of the electronic state with spatially extended orbitals of higher energy that interact with the electronic system of the neighboring molecules or the surface. Simmilar effects are known to happen to the *Rydberg* states of atoms adsorbed on surfaces [70].

The difference of the ionization potentials of azo and cyano N 1*s* core-level electrons was already explained. Beside the chemical shift of the cyano N 1*s* core level to higher binding energies, there is an opposing mechanism originating from the electron relaxation in the presence of the core holes. The lower two graphs of Fig. 4.12 show the calculated change of electron density going from the ground state to the core ionized molecule for different core excitation centers. The atom number corresponds to the index of the atoms

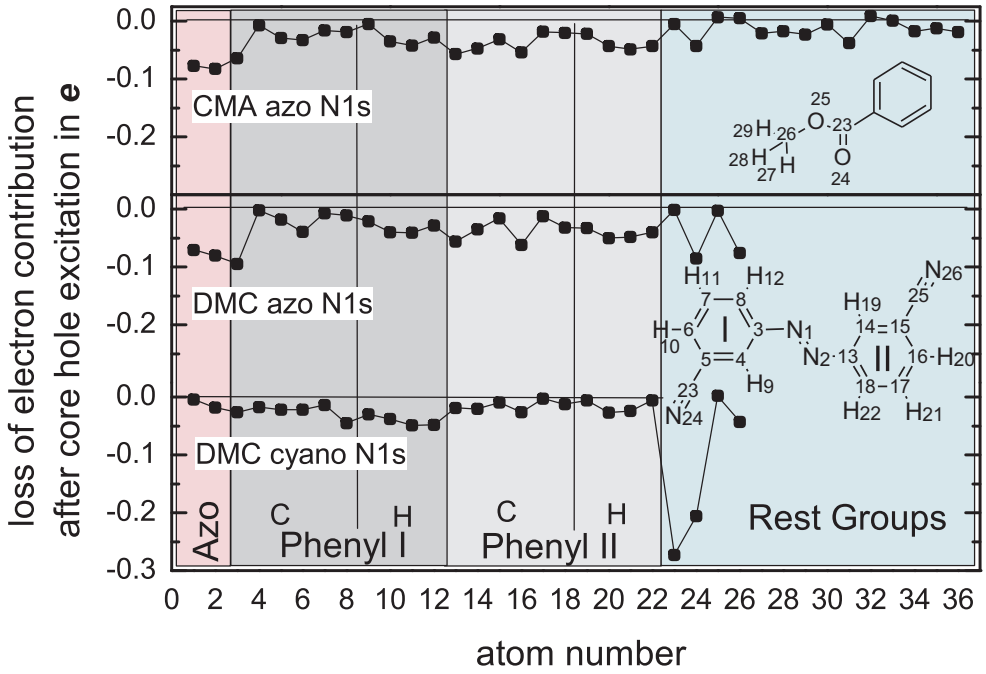

Figure 4.12: *Calculated change of the electron contribution at the different atomic sites due to the N 1s core ionization for the CMA azo (N1), the DMC azo (N1), and the DMC cyano (N24) nitrogen excitation center in the upper, middle, and lower panel, respectively. Negative values denote electron loss. The atom number corresponds to the numbers given in the ploted structures.*

int the plotted structures. The core ionization of the azo nitrogen atom (atom N1) causes a total electron loss of less then 0.2 e at the two azo nitrogens atoms. In contrast the cyano N 1s (atom N24) core ionization provokes an electron loss of more than -0.5 e at the C≡N moiety (-0.3 e for the N24 atom, and -0.2 e at the C23 site). This is due to the fact that compensating electrons can flow from both halves of the molecule into the azo center whereas for the cyano group the electrons are only supplied by the neighboring benzene ring. Thus the screening effect is supposingly higher at the azo center. In spite of this competing effects the binding energy is still remarkably high.

Beyond the ionization potentials σ shape resonances appear mainly from the azo core electron excitation. In the simulated NEXAFS above the IP the FWHM was increased linearly up to 4.5 eV at 10 eV beyond the IP. due to the typical decrease of life time of the unbound final states toward higher energy. Here the broadening was kept below the experimental findings in order to distinguish between the different features.

4.2.2 Carboxymethylester azobenzene

A second azobenzene derivative, used in this work, is functionalized with carboxymethylester rest groups in *meta* positions. It carries only one nitrogen species in the azo center, as it can be seen in the structure in Fig. 4.13. Thus, this compound can be used as reference to identify the different contributions of the inequivalent nitrogen excitation centers that are present in N K-shell NEXAFS as well as in the N 1s XPS of DMC. Since also the ester rest groups are attached in *meta* position, the central azo frontier orbitals are not affected by the substituted electronic system. This is confirmed by ground state calculations in analogy to the considerations of DMC. The resulting LUMOs are given in Fig. 4.14. The electronic distribution of the LUMO is equal to that of DMC. The π^* orbitals that are related to the methylbenzoate moiety are at higher energy positions.

The corresponding N K-shell NEXAFS is shown in Fig. 4.11. The upper spectrum shows the NEXAFS measured for a CMA powder sample pressed on an indium foil. The only pronounced π^* resonance visible at 398.5 eV originates from the transition of the N 1s core level into the LUMO. For the sake of comparison, the corresponding data for DMC are included. The π^* resonance in the CMA spectrum fits perfectly with the component at lower energies that was found as a shoulder in the broad peak of the DMC NEXAFS at around 398.8 eV. The fact that the azo(N 1s)→LUMO resonance is found at the same energy position for DMC and CMA does not imply that the excitation centers are embedded in the same chemical environment, but the dicussion about the chemical state can be reduced to two cases: either no chemical shift is caused by the rest goups or both, initial and final states are shifted equally in energy with respect to the ionization potential in DMC and CMA.

More information can be extracted from the calculated data. The sim-

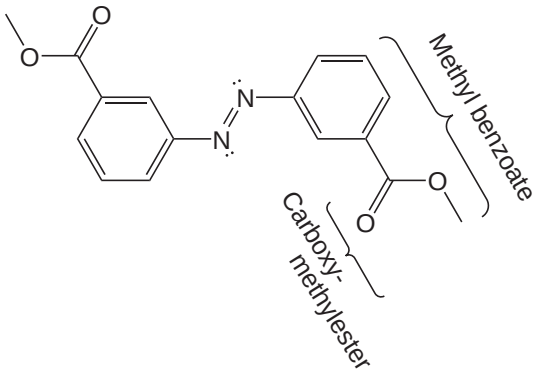

Figure 4.13: *Geometric structure of Dimetacarboxymethyl azobenzene with the labeled molecular sub umits as they are used in the text.*

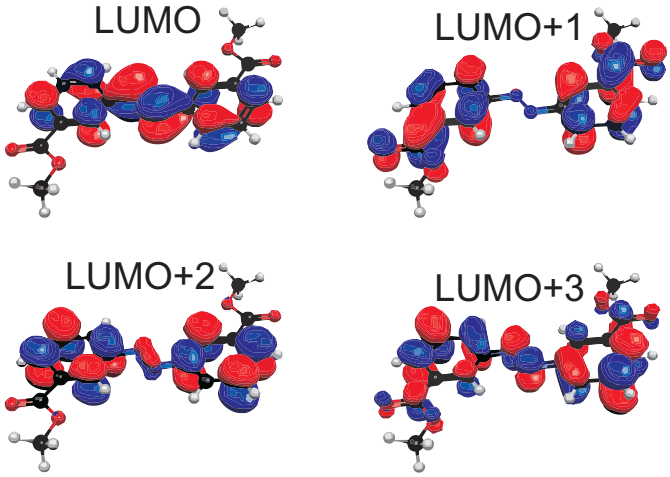

Figure 4.14: *LUMOs for the ground state of dimetacarboxymethyl azobenzene (CMA).*

ulated NEXAFS of CMA, shown as the lower black spectrum in Fig. 4.15, has its resonance at the same position as the spectrum of the simulated partial absorption of the N 1*s* azo center of DMC. This is in accordance with the experimental result. The calculated ionization potentials of the azo N 1*s* core electrons of CMA and DMC are different. Thus a different chemical shift due to the cyano and ester rest groups exists and affects the energies of both electronic states involved in the azo(N 1*s*)→LUMO transition.

The lower ionization potential for the CMA N 1*s* core level electrons can be explained by analyzing the chemical character of the methyl benzoate moieties by means of valence bond theory and by comparing this to what is found for benzonitrile (*cf.* Sec. 4.2.1). The methyl ester group exhibits a strong electron-accepting character due to the two branches that contain oxygen with a higher electron negativity than the surrounding carbon. In contrast to the cyano group, the methyl ester is not a radical in the sense of carriyng a vacant electronic state. Thus no electron can be transferred from the benzene ring to the ester rest group in the ground state configuration so that the phenylic carbon at the substitution position remains uncharged. In other words, the phenyl rings of CMA do not mediate the electron-accepting character of the rest groups to the azo center as in the case for DMC. However, the charge distribution at the C–N=N–C azo center is found to be identical to the one of DMC. Differences are only visible in the aromatic environment. Furthermore the calculated relaxation effect presented in the upper panel of Fig. 4.12 fits supprisingly well to the one of the DMC N1 1*s* core excitation. Thus the difference of the N 1*s* ionization potentials of DMC and CMA can only be caused by the phenylic surrounding.

In methyl benzoate, the π system of the ester rest group links to that of the

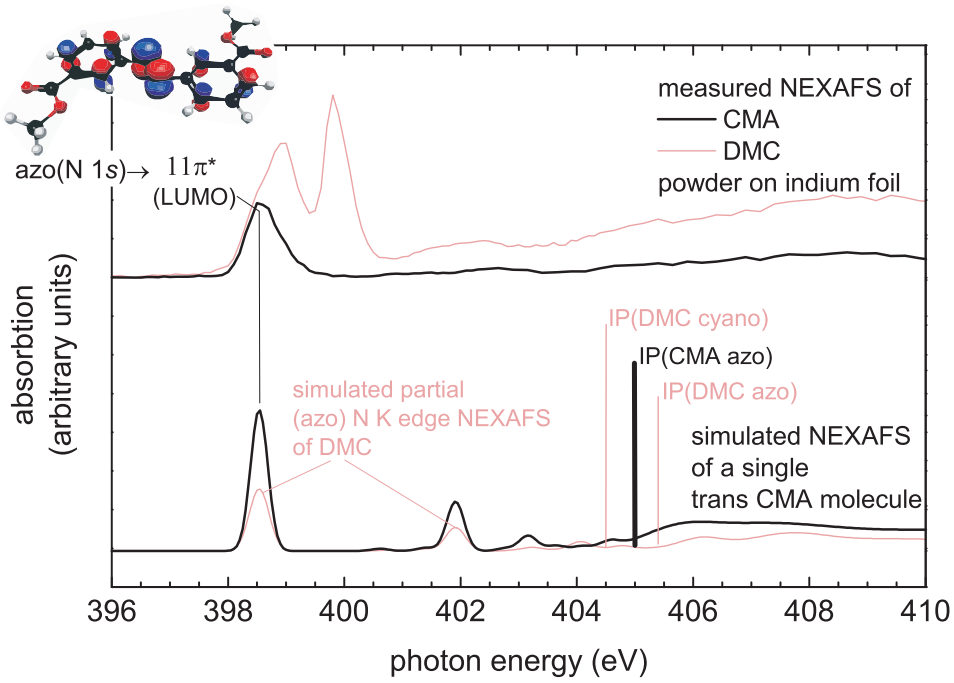

Figure 4.15: *Upper black spectrum represents the measured N K-shell NEXAFS of CMA powder pressed on an indium foil. The pink line is the corresponding spectrum of DMC. The lower black spectrum is the simulated N K-shell NEXAFS of a single trans CMA molecule, while the pink line gives the calculated partial absorption of the azo nitrogen of DMC. The N 1s ionization potentials of CMA and DMC are given by the vertical black and pink lines, respectively. The orbital shown as an inset is the LUMO of the corresponding transition state.*

benzene ring as one can see for the LUMO+1 and LUMO+3 in Fig. 4.14. Thus the conformation with the lowest total energy is the one with the O=C-O-C moiety in same plane as the benzene ring due to the maximum overlap of the two contributing π orbital systems in the configuration. The rotational energy barrier was found to be 26 kJ/mol [71]. Hence the orientation of the methyl ester in the ground state geometry is strongly aligned to the one of the benzene ring. In contrast to the cyano group of benzonitrile, for methyl benzoate the two dimensional-structure of the ester rest group might be forced to rotate around the bond between the phenyl ring and the substituted rest group. It has been shown that this can happen, e.g., in the presence of an additional substituent in *ortho* position [71] or due to intermolecular interactions in an ensemble of adsorbed molecules. Consequently, the analysis of the molecular orientation has to be conducted with due care. For a single CMA molecule

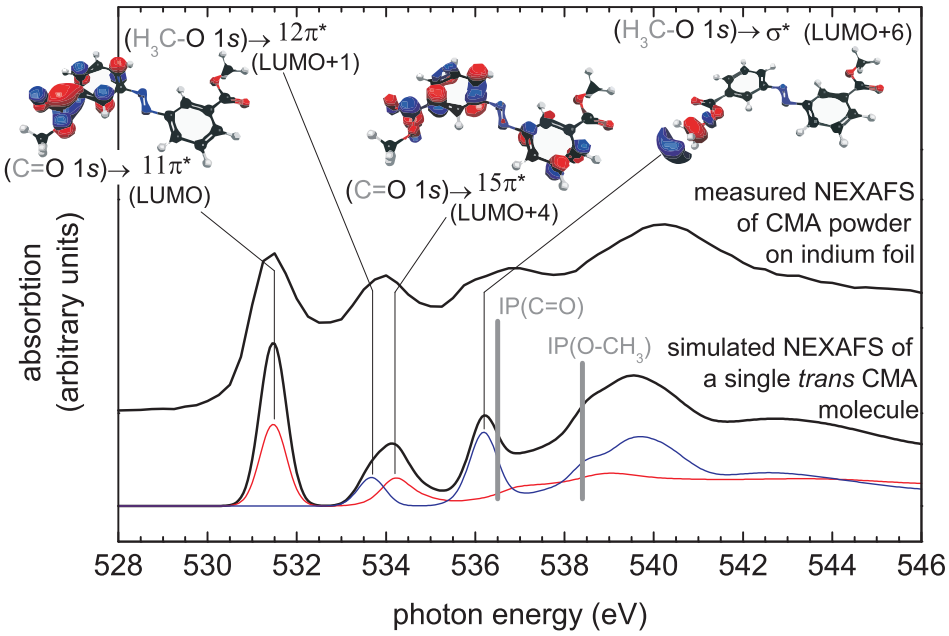

Figure 4.16: *Upper black spectrum represents the O K-shell NEXAFS measured for CMA powder pressed on an indium foil. The lower black spectrum is the simulated O K-shell NEXAFS of a single trans CMA molecule. The red and blue spectra give the partial absorption of the carbonyl (C=O) and the carboxy (H_3C-O) oxygen species, respectively. The vertical grey lines mark the ionization energies of the two different excitation centers. The orbitals present as insets are the LUMOs of the corresponding transition states.*

the quantum chemical geometry optimization leads to the *trans* conformation when starting from a planar molecular structure with literature coordinates of azobenzene [68] and methyl benzoate [72].

The O K-shell NEXAFS, measured for the powder sample of CMA, is given as the upper black spectrum in Fig. 4.16. The experimental data are in good agreement with those of gas phase ethyl benzoate that had been confirmed by *Extended Hückel Theory* [73]. Pronounced resonances found at around 531 eV and 534 eV were assigned to the C=**O** 1s and the ethyl–**O** 1$s \rightarrow \pi^*$ transitions, respectively, and appear in the present experimental data at the same positions. The different alkyl groups seem to influence the alkyl–**O** K-shell NEXAFS in the same way.

The corresponding simulated NEXAFS of the geometry-optimized isolated *trans* CMA molecule, given as the lower black spectrum in Fig. 4.16, confirms the energetic position of the experimental π^* resonances. Hence, torsions of

the caboxymethyl moiety relative to the benzene part around the ester–phenyl bond can be ruled out here, since would change the overlap of the contributing π systems and thus the energy positions of the resulting bonding/antibonding orbitals with respect to the initial core level. In conclusion, inter-molecular interactions in the molecular crystal do not disturb the natural planar geometry of the methyl benzoate. In the case that ester groups and benzene rings are coplanar, the angle dependence of the O K absorption edge will give information about the orientation of the benzoate moiety, where the contribution of the ester π bond orbital to the NEXAFS signal is comparable to the one of the out-of-plane cyano π_y bond orbital.

Furthermore the two contributions of the inequivalent O 1s excitation centers exhibit strikingly different ionization energies. This leads to an equipollent energy separation of the corresponding features that contribute to the entire NEXAFS spectrum. Their contributions are given as red and blue lines below the black sum spectrum for C=O and CH_3–O, respectively. The first two π^* resonances are separated by almost the same energy as the two O 1s core levels. This is due to the fact that they originate from the transitions of the latter into the molecular orbital that was found to be the LUMO+1 in the ground state calculation (*cf.* Fig. 4.14). Obviously the order of the LUMOs changed in the presence of the C=**O** 1s core hole, since the resulting reduced core screening has a different influence on differently localized orbitals. This was remarked already in the previous subsection about DMC. Consequently the LUMO of the C=**O** 1s transition appears as the LUMO+1 in the presence of the H_3C-O 1s transition state.

A second remark has to be made here, concerning the labeling of different types of resonances and the corresponding transitions. The terms π^* and σ-shape resonances do not signify transitions into the π^* and σ^* orbitals, respectively. The expressions rather label different types of excitation channels as it was described in detail in Sec. 2.2. The σ-shape resonances are caused by transitions into non-bonded states (ionization process), whereas π^* resonances end in a neutral excited state. In fact, for the C-O-CH_3 **O** 1s CMA it turns out that there exist three bonded transition state orbitals of σ symmetry which are related to a π^* resonance. One of those three (bond-state) σ orbitals is the LUMO+4 (C-O1s-CH_3) and is plotted as an inset in Fig. 4.16.

Summary The core level spectroscopy of azobenzene powder samples reveals a deep insight into the electronic configuration of different subunits of the two azobenzene derivatives. It turns out that the chemical structure in the organic crystals resembles the one calculated for the isolated *trans* isomers.

Valence-state and molecular-orbital theory predict that the frontier orbital system of azo center and rest groups are decoupled. By DFT ground-state calculations confirm this prediction. However, different ionization potentials are calculated for the DMC and CMA azo-N 1*s* core-level electrons. Since the corresponding core-electron transitions into the azo LUMOs exhibit the same resonance energies for both molecules we have to conclude that the valence states are shifted too either in the ground or in the exited states or both. The calculated relaxation schemes evince this energy shift as an effect of the final core-ionized/-excited states and not in the ground state. An influence of the rest groups at least on the LUMO energies can thus not be excluded completely for the core-level spectroscopy. However, the expected ground-state interaction between adsorbate and substrate should not be effected by the rest groups.

4.3 Adsorption on metallic surfaces

One of the most important aspects for the sample preparation on metallic surfaces is the determination of the amount adsorbate. For the adsorption of a molecular monolayer one can define the degree of coverage Θ_{cov} as the ratio between the number of adsorbed molecules N_{ads} and the maximum number N_{max} of molecules that can be adsorbed directly on the surface:

$$\Theta_{cov} = \frac{N_{ads}}{N_{max}} \tag{4.1}$$

Of course, this definition only makes sense if the maximum coverage N_{max} is well defined. Even in this case N_{max} can be given by different scenarios. In the simplest case, where the molecule-substrate interactions are sufficiently strong to induce adsorption on the surface and molecule–molecule interaction is so small that the accumulation of a molecular multilayer is not possible, only a single monolayer of molecules would be adsorbed on the surface. Then N_{max} is given by the ratio between the area a single molecule occupies in average on the surface and the total area that is available. In this special case, Θ_{cov} corresponds to the parameter x in Eq. (2.13).

It was already shown in Sec. 2.1.3 that, due to scattering of electrons in matter, the photoelectron signals of substrate and adsorbate strongly depend on the thickness of the adsorbate film. Thus, in the case of a layer-by-layer growth, one can use the measured ratio between the adsorbate and the substrate signal to Equ.(2.13) in order to determine Θ_{cov}. This procedure has to be preceded by the determination of the signal intensities of the clean substrate

I_{s0} as well as the ones for the full monolayer adsorbate I_{a0} and I_{subst} for each photon energy needed.

4.3.1 Adsorption on Au(111)

4.3.1.1 Adsorption rate

The adsorption rate of dimetacyano azobenzene on Au(111) has been investigated for two different substrate temperatures. The molecules are evaporated step by step with increasing exposure times. An X-ray gun and a standard electron analyzer are used to measure the ratio of the C $1s$ and the Au $4f$ XPS signals between all steps. The Mg anode of the X-ray gun provided photons with an energy of 1253.6 eV. Since the corresponding energy of the Au $4f_{7/2}$ photoelectrons is 1169.6 eV, their mean free path is much larger than the thickness of a molecular monolayer and the intensity of the clean substrate I_{s0} is of the same order as for the substrate covered with one monolayer of molecules I_{subst}. Taking Θ_{cov} as the fraction x that was defined in Eq. (2.13) one sees that in this case $R(\Theta_{cov}) \sim \Theta_{cov}$ (or $R(x) \sim x$ in Sec. 2.1.3).

In Fig. 4.17 the intensity ratio is given as a function of the evaporation time for two adsorption experiments on Au(111) at different temperatures. In panel (a) the adsorption at room temperature is shown, where the adsorption rate decreases with evaporation time and a maximum coverage can be foreseen. The maximum coverage implies that with increasing Θ_{cov} the area that is still available decreases. This results in an inversely exponential evolution of the coverage by time. For a constant evaporation rate the number of adsorbed molecules N_{ads} after an evaporation time t is given by:

$$N_{ads}(t) \;=\; N_{max}(1 - e^{-\sigma t}). \tag{4.2}$$

The same relation holds for the intensity ratio $R_{ads} \sim N_{ads}$, which can be fitted with the corresponding parameters $R_{max} = R(N_{max})$ and σ. The red curve in Fig. 4.17(a) represents the result of the fitting procedure, where $R_{max} = 0.02$ for the present experimental conditions.

In Fig. 4.17(b) the analogous adsorption experiment for a substrate temperature of 150 K is shown. The only experimental parameter which might have changed additionally is the evaporation rate. In contrast to the adsorption on Au(111) at room temperature no saturation appears and the thickness exceeds 1 ML. Thus $R(N_{ads})$ might not be proportional to N_{ads} anymore. Taking σ from the former experiment and the number of layers N of Eq. (2.12) proportional to the adsorption time t, we get the relation between the coverage and the intensity. The relation is represented by the red line in Fig. 4.17(b),

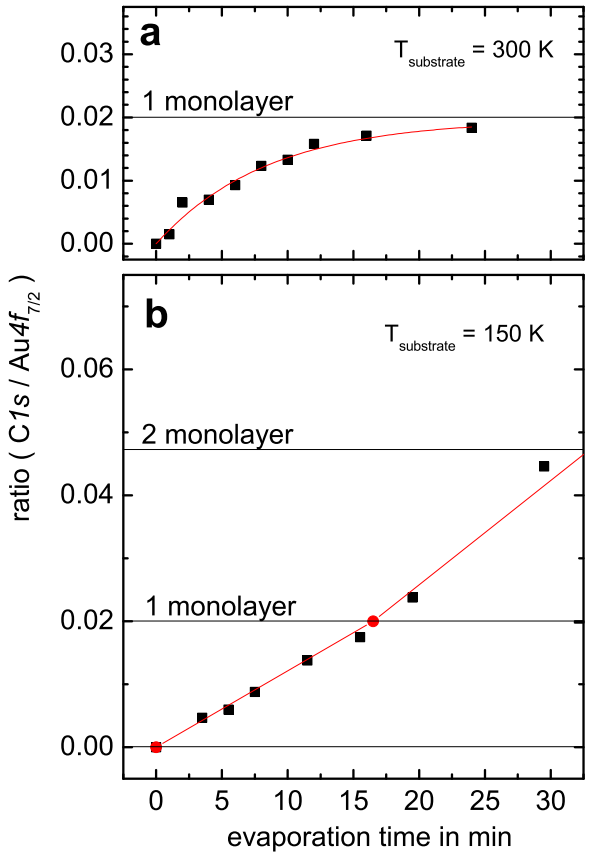

Figure 4.17: *XPS intensity ratio of the C 1s and Au $4f_{7/2}$ core level electrons given for a sequence of evaporation steps of DMC on Au(111) at room temperature (panel a) and at 150 K (panel b) in order to determine the degree of coverage. In both cases the corresponding fit functions are red presented as red lines.*

where the time when a full monolayer is formed is chosen *ad hoc* to be 16.5 min.

4.3.1.2 Adsorption state

DMC In Fig. 4.18(a) the XP spectrum of a film of about 20 ML of DMC on Cu(001) is shown. This spectrum can be used as a reference of molecules decoupled from the surface, since for 20 ML the main signal comes from the 95% of molecules that are in a physisorbed confinement of a molecular crystal. Furthermore the electron signal of the interfacial adsorbate-substrate layer is weakened by the overlayer due to the small mean free path of electrons in matter (*cf.* Sec. 2.1.3). Two strong peaks at 399.4 eV and 400.4 eV, originating from the two non-equivalent N 1*s* excitation centers in the azo bridge and the cyano rest groups, are visible. The two different binding energies can be explained considering the influence of the local chemical environment on the core-level binding energies as it was done in Sec. 4.2.1.

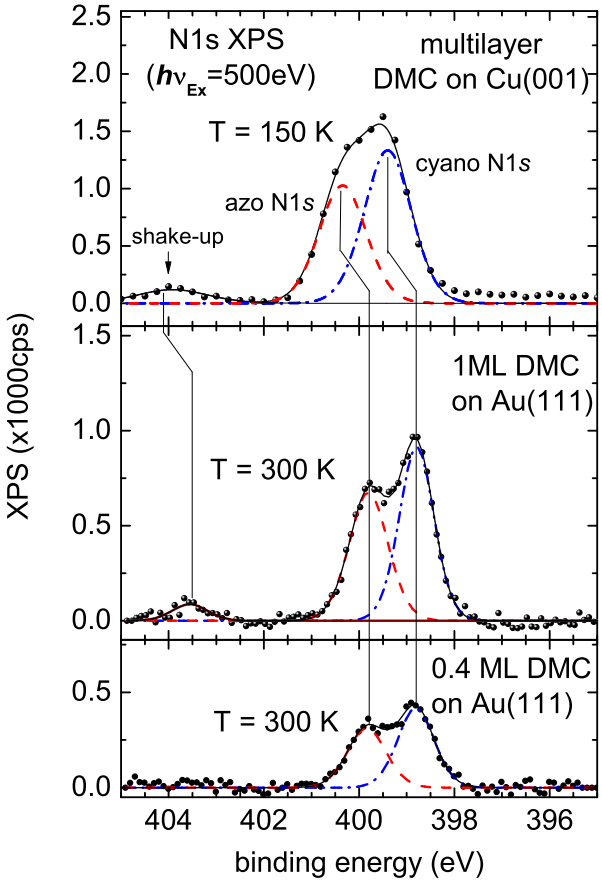

Figure 4.18: *N 1s XP spectra of a multilayer of DMC on Cu(001) (a) evaporated at 150 K, and of 1 ML (b) and a submonolayer (c) of DMC molecules evaporated on Au(111) at room temperature. Peak energies are calibrated to the Cu 3p and the Au $4f_{7/2}$ XPS signal at 84.0 eV for the multi- and monolayer, respectively.*

Cyano groups exhibit a strong permanent dipole moment with an increased electron density at the nitrogen site [67]. It was further shown in the previous section that the azo center carries almost no additional charge. This leads to the same chemical shift as in the calculated ionization potentials, such that the azo N 1*s* XPS exhibits a higher binding energy than the one of the negatively charged cyano N 1*s* excitation center.

Figure 4.18(b) shows the N 1*s* photoemission spectrum of 1 monolayer DMC on Au(111). A shift of the whole spectrum of 0.6 eV to lower binding energies appears comparing the spectrum of the multilayer on Cu(001) to the one of the monolayer on Au(111). It was reported that at the interface between a metallic substrate and an organic adsorbate a surface dipole is induced with a reduced electron density on the adsorbate side [74]. The resulting difference of the potential energy between the substrate and the adsorbate corresponds to a lowering of the adsorbate states' energy with respect to the Fermi level of the

metallic substrate. It was further shown for perylene-3,4,9,10-tetracarboxylic dianhydride (PTCDA) that the corresponding dipole moment increases from the physisorbed phase on Au(111) to the chemisorbed one on Cu(111) [75]. The higher the corresponding dipole moment, the stronger is the shift of the binding energy (measured with respect to the Fermi level) of the adsorbate electrons to lower values. Apart from the spectral shift, all features of the multilayer spectrum are reproduced for the sub- and monolayer. This is already a strong indication that no covalent bonding to the Au(111) surface takes place, since the chemical environment of the different excitation centers has not changed.

Additional low intensity peaks are visible at higher energies of 403.6 eV. For mono-substituted benzene it has been shown that such shake-up intensities can be observed if the main ionization transition is coupled to an additional electronic HOMO–x→LUMO+y [76]. In the case of DMC, the smaller intensity of the azo-N 1*s* peak compared to the one of the cyano nitrogen, indicates that the shake-up process is only coupled to the ionization at the azo center. This is consistent with the localized character of the frontier orbitals due to the particularly weak mixing of the π systems of azobenzene and benzonitrile (see Fig. 4.10). Hence we can assign the shake-up to a coupling between the azo-N 1*s* photoemission process and the electronic transition from one of the two HOMOs to the LUMOs at the azobenzene center. The appearance of such a transition proves the existence of the undisturbed original frontier orbital system that is involved in the switching mechanism.

In Fig. 4.19(a), N *K*-shell NEXAFS spectra are given for a multilayer evaporated at 150 K, where the solid and dashed lines correspond to 90° normal and 20° grazing light incidence with respect to the metal surface, respectively. Considering the sum of both spectra, the overall spectral shape is in accordance with the one measured for the bulk spectrum. This indicates, that there is no molecular damage caused by the evaporation, and that the two strong π^* resonances can be assigned as for the molecular powder. In contrast to the spectrum of the microscopically disordered bulk sample, here a pronounced angle dependence is visible for all spectral features. This linear dichroism originates from the particular order of the orientation of the molecular π orbital system with respect to the surface normal of the substrate and the associated alignment of the transition dipole moment (*cf.* Sec. 2.2.2). The opposite angle dependence of the two resonances at 398.8 eV and 399.9 eV can be related to the two types of π orbitals with perpendicular orientation, namely the system of π orbitals perpendicular to the surface plane and the one containing the *in-plane* orbitals. While the former *out-of-plane* orbital system covers the whole molecule (although the contributions are particularly localized), the

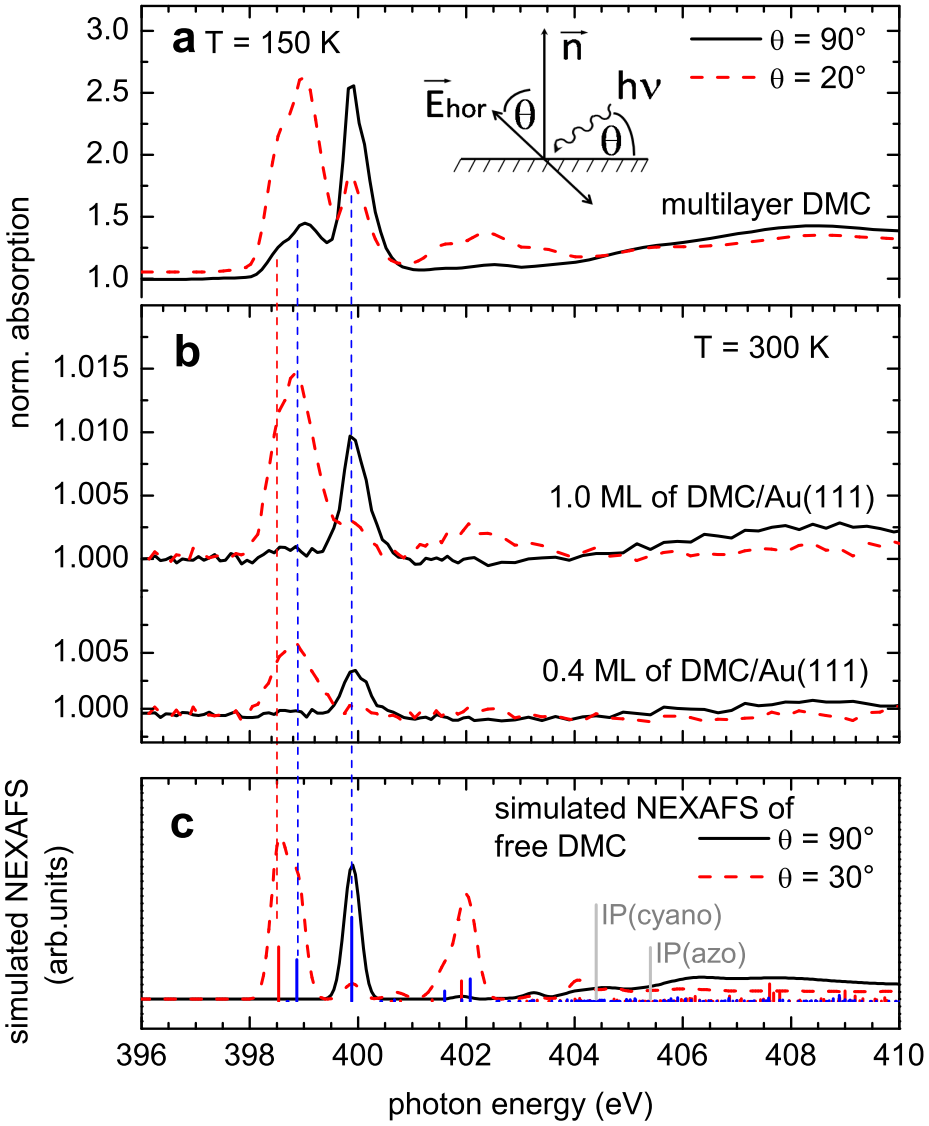

Figure 4.19: *Angle-dependent N K edge absorption spectra of (a) a multilayer sample of DMC evaporated at 150 K substrate temperature and (b) 1 and 0.4 ML DMC on Au(111) evaporated at room temperature. Continuous (dashed) lines correspond to spectra at* 90° *normal (*20° *grazing) X-ray incidence. (c) Simulated NEXAFS spectra of a free trans DMC molecule. In this case the grazing spectrum corresponds to* 30° *X-ray incidence. For the angle dependence of the calculated spectrum, the molecular plane corresponds to the surface plane in the inset of panel (a). The transition dipole moments are presented below the calculated curves as vertical lines. The gray vertical lines at* 404.4 *eV and* 405.4 *eV in the simulated spectrum of DMC mark the ionization potentials (IP) of the cyano and the azo N* 1*s core levels.*

latter is mainly present at the cyano groups. Thus we can conclude from the measurement that the molecules exhibit a high degree of zenithal order in the multilayer.

A more pronounced angle dependence and thus a higher degree of order in the molecular film is found for 0.4 and 1 ML DMC evaporated on Au(111) at 300 K. Here the absorption peak at 398.8 eV is only present in the spectrum of grazing incidence. Thus the *out-of-plane* π system is completely perpendicular to the surface. The small contribution of the peak at 399.9 eV in grazing incidence is explained by the fact, that the polarization vector of the electromagnetic wave is not perpendicular to the surface, since the light incidence angle is only 20° and not 0°. Thus the projection of the *in-plane* π^* orbital on the polarization vector of light does not vanish although the orbital orientation is in the metallic surface plane. In the spectrum of one 0.4 and 1 ML also the angle dependence of the σ-shape resonances is apparent. Since the σ-bond frame work defines the molecular plane, this is another proof that the molecules lie flat on the surface.

For 0.4 ML no remarkable differences in the overall spectral shape are found compared to the full monolayer. Thus we can exclude any coverage dependence of the adsorption states.

The measured angle dependence is in perfect agreement with the one simulated for a single oriented DMC molecule as it is shown in Fig. 4.19(c). For the latter the molecular plane was identified with a hypothetical surface plane in order to assess the light incidence angle. Here the experimental data at grazing angle of 20° agree best with the simulated curve for 30°. This might be explained by Fresnel diffraction which appears due to the interaction of the incoming X-ray wave with the electron density at the surface [46]. The quantitative agreement of the π^* resonances in the spectra of monolayer and submonolayer of DMC on Au(111) with those in the simulated spectra of an isolated DMC molecule allows us to conclude that the molecule physisorbes flat on the surface. Furthermore, the overall shape of the measured spectra is reproduced by the calculations, except for the overestimated intensity at 402 eV. This discrepancy is most likely due to the absence of the surface in the calculation [77].

In the measured XPS the distance between the azo and the cyano N 1*s* binging energy is found to be 1.0 eV. This is confirmed by the calculation, since the distances of the two corresponding ionization potentials has the same value. The difference between binding energy and ionization potential is simply caused by the different energy references for measurement and calculation. The measured values are given with respect to the Fermi edge of the substrate,

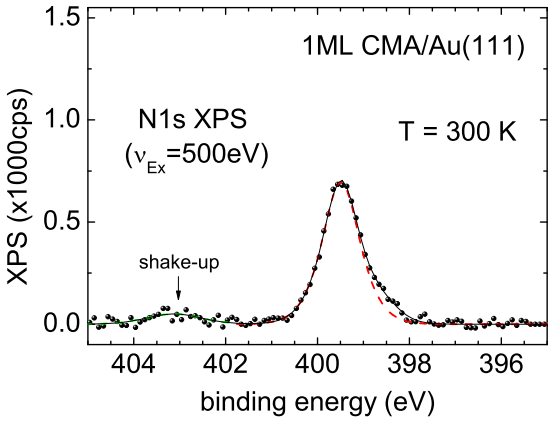

Figure 4.20: *N 1s XPS spectra of 1 ML of CMA molecules evaporated on Au(111) at room temperature. Peak energy is calibrated to the Au $4f_{7/2}$ XPS signal at 84.0 eV.*

while the calculated ones are referenced to the vacuum level. The energy difference between the two references corresponds to the Au(111) work function (*cf.* Sec. 2.1).

CMA In Fig. 4.20 the N 1*s* XPS signal of 1 ML CMA on Au(111) is given. A single peak at 399.5 eV results from the photoemission of the N 1*s* azo core electrons, since CMA contains nitrogen atoms only in the azo bridge. The difference in binding energy of 0.3 eV compared to the one of the azo N 1*s* core level electron of DMC is in good agreement with 0.5 eV difference of the calculated ionization energies for the molecules (*cf.* Fig. 4.15) and it can be explained by the lower electron affinity of the ester rest groups compared to that of the cyano groups [78] (*cf.* Sec. 4.2.2). A similar low intensity peak as in the XPS of DMC is visible at 403.1 eV in the N 1*s* XPS of CMA and confirms the intact frontier orbital system in the center of the CMA molecule.

The corresponding angle-dependent experimental and calculated NEXAFS spectra of CMA are given in Fig. 4.21. Multi- and monolayer spectra are identical to the bulk spectrum of CMA. This confirms that the molecules are intact after evaporation on the surface. A single sharp π^* resonance appears here again around 398.5 eV in all spectra of the multilayer and for 1 ML only in the spectrum of 20° X-ray incidence. Thus, one can conclude that the azo bridge is oriented parallel to the surface. Furthermore the molecules are found to be physisorbed in the monolayer on the surface, since the spectra of mono- and multilayer do not differ except in the angle dependence. The increasing disorder that is observed here toward higher thicknesses was also found for DMC.

The O *K* edge yields complementary information about the adsorption of

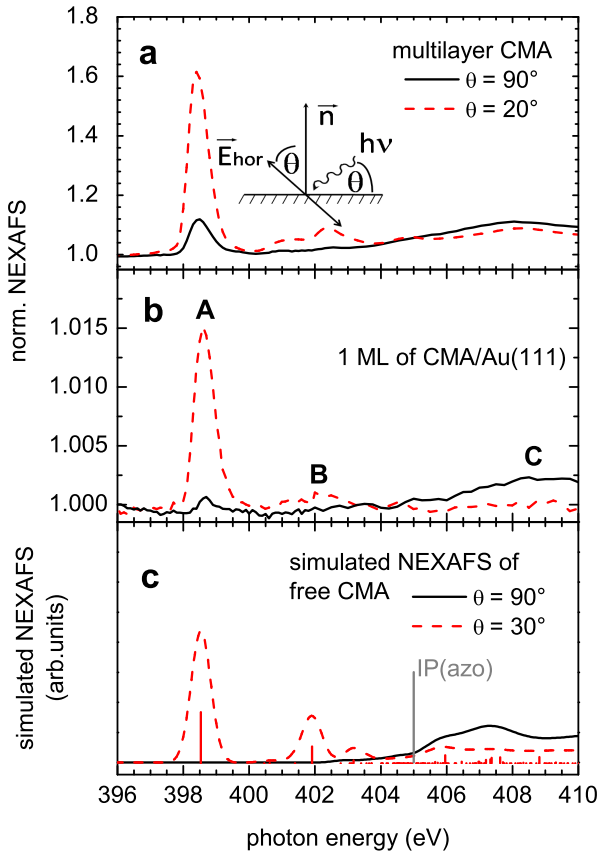

Figure 4.21: *Angle-dependent N K edge absorption spectra of (a) a multilayer and (b) a monolayer CMA on Au(111) evaporated at room temperature. Continuous (dashed) lines correspond to spectra at 90° normal (20° grazing) X-ray incidence. (c) Simulated NEXAFS spectra of a free trans CMA molecule. In this case the grazing spectrum corresponds to 30° X-ray incidence. For the angle dependence of the calculated spectrum, the molecular plane corresponds to the surface plane in the inset of panel (a). The transition dipole moments are presented below the calculated curves as red vertical lines. The gray vertical line at 405.0 eV in the simulated spectrum marks the ionization potentials (IP) of the azo N 1s core level.*

the carboxymethyl rest groups at the molecular periphery. Fig. 4.22(a) and (b) show the corresponding measured data. The same physisorption state is found for the rest groups in the multi- and monolayer. In the regions between 530 eV and 535 eV two sharp resonances at 531.5 eV (peak A) and 539.0 eV (peak B) are only present in the spectrum of grazing incidence. As shown in Sec. 4.2.2 these features originate from transitions into the ester π system which is thus perpendicularly oriented to the surface. In contrast, the angle dependence of the peak C does not attest that the related final state σ^* orbital is aligned in the surface plane as it follows from the ratio of 0.8 between grazing and normal incidence intensity (*cf.* Sec. 2.2.2). Both findings are in contradiction, since the C-O π and σ orbitals should be perpendicular.

In order to fathom this disagreement one has to look at the simulated angle-dependent O K-shell NEXAFS of the geometry-optimized isolated CMA molecule given in Fig. 4.22(c). The optimized geometry was almost fully planar with the ester group tilted by an angle less than 3° away from the benzene

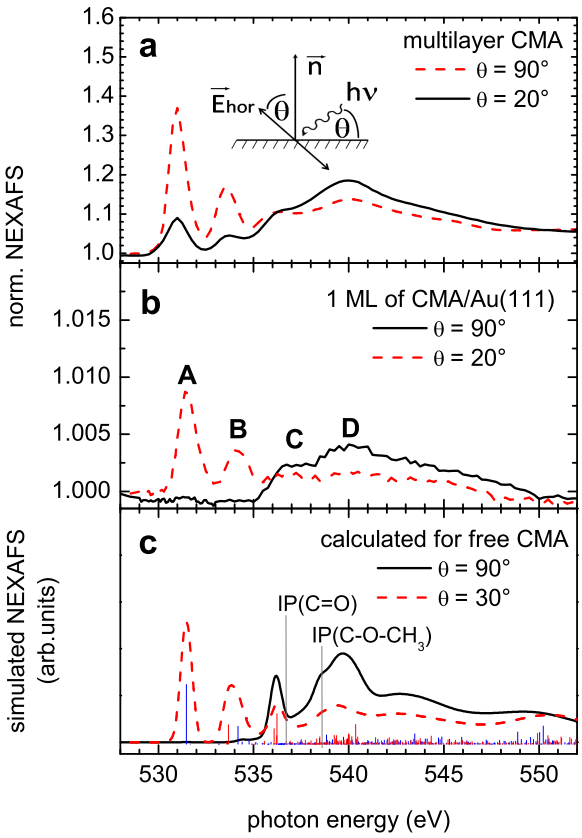

Figure 4.22: *Angle-dependent O K edge absorption spectra of (a) a multilayer and (b) 1 ML of CMA molecules evaporated on Au(111) at room temperature. Continuous (dashed) lines correspond to spectra at 90° normal (20° grazing) X-ray incidence. (c) Simulated NEXAFS spectra of a free trans CMA molecule. In this case the grazing spectrum corresponds to 30° X-ray incidence. For the angular dependence of the calculated spectra, the molecular plane corresponds to the surface plane in the inset of panel (a). The transition dipole moments are presented below the calculated curves as vertical red and blue lines. The two gray vertical lines at 536.7 eV and 538.6 eV mark the ionization potentials of the C-O-CH_3 and the C=O oxygen core levels, respectively .*

ring. Although the C–O–C σ^* bond axis lies parallel to the surface in the NEXAFS simulation, the resulting angle dependence around 536 eV affirms the corresponding C–O–C σ^* bond orbital oriented partially out of the surface plane. This is in agreement with the measured data of 1ML. By inspecting the corresponding transition state orbital it is found that the out-of-plane orientation is due to the additional mixing of the C–H σ bond orbitals of the methyl group to those of the C–O–C σ bond. Those C–H σ bond orbitals are conversely oriented due to the sp^3 hybridization of the bearing C atom. Thus the angle dependence of peak C is not suitable to accurately determine the benzoate orientation on the surface. Nevertheless, the orientation of the π orbitals is determinable and additionally a tendency of the molecular tilt can be obtained from peak C. The comparison of simulated and measured angle-dependent N K-shell NEXAFS, leads to the conclusion that the entire CMA molecule physisorbs flat on the surface in the similar as the DMC.

Finally the O 1s XPS of 1 ML CMA on Au(111) is given in Fig. 4.23. Two

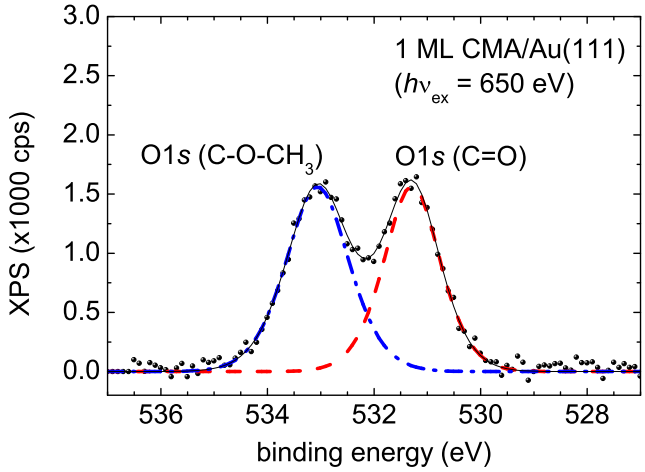

Figure 4.23: *O 1s XPS of 1 ML CMA evaporated on Au(111) at room temperature. Red and blue lines represent the fitted components that can be assigned to the C=O and the C-O-CH_3 O 1s excitation centers.*

equally shaped peaks arise at 531.3 eV and 533.1 eV. The energy distance is in good agreement with the one of the calculated gas phase molecule, and the sizable energy difference is enough to inform of which part of the ester moiety is more involved in a possible chemical interaction.

Summary From NEXAFS and XPS studies we find both azobenzene derivatives adsorbed on Au(111) with a maximum (saturation) coverage at room temperature while they adsorbe in a thick film of a partially ordered crystalline phase on the surface at 150 K. From the lower intermolecular sticking coefficient we can conclude the intermolecular interactions are weaker than the interaction between adsorbate and substrate. The measured NEXAFS spectra of sub- and monolayer do not exhibit any difference compared to the crystalline forms. Furthermore, they are reproduced by DFT-based simulations of the corresponding spectra of a free molecule. Thus covalent or ionic bond formation can be excluded, since they are expected to change the configuration of the frontier orbital system including the unoccupied states probed by the NEXAFS technique. A chemical shift, as well as a relaxation shift, should be visible in XPS due to the change of the bond configuration. In conclusion, the adsorption process can only be driven by localized electrostatic interaction in the form of (adsorbate)dipole—(metal)image-dipole interaction and by diffusive van-der-Waals forces that lead to physisorption.

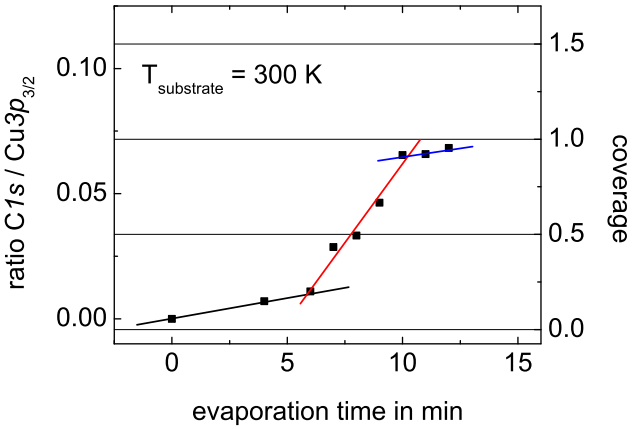

Figure 4.24: *XPS intensity ratio of the C 1s and Cu $3p_{3/2}$ core level electrons given for a sequence of evaporation steps of DMC on Cu(001) at room temperature in order to determine the degree of coverage. The three differently colored lines indicate regions of different adsorption rates.*

4.3.2 Adsorption on Cu(001)

4.3.2.1 Adsorption rate

For the adsorption on Cu(001) at room temperature, the corresponding adsorption characteristics can be seen in Fig. 4.24. Similarly to the experiment on Au(111) at room temperature, the coverage saturates after a certain time. This can be used again as a reference to calibrate the thickness of all the following preparations. Unfortunately, the data points do not follow a reasonably characteristic curve, like for Au(111) substrate at room temperature, where the amount of adsorbate per time unit decreases exponentially in time. At this point, no reliable interpretation can be made but the assumption, that the adsorption behavior changes at a certain coverage leading to a higher adsorption rate. This is contradicting with the simplest picture of only one type of substrate-adsorbate and one type of adsorbate-adsorbate interaction. A dominating adsorbate–adsorbate interaction would result in two convoluted contributions in the form of Eq. (4.2), where the contribution of the multilayer prevails and the resulting shape of the fit function is similar to the one of Fig. 4.17(b). A strong adsorbate-substrate interaction in the absence of adsorbate-adsorbate interaction would lead to a saturation as it is observed for DMC on Au(111) at room temperature. Thus we have to conclude that more than one type of adsorbate-surface interaction appears for different coverages.

By looking at the N 1*s* XP spectra in Fig. 4.25 that are taken at each evaporation step, significant changes are observed that coincide with the regions of different adsorption rates. The first to spectra show a broad peak around 398.5 eV which increases linearly in intensity from 4 min evaporation time to 7 min. In the second region (red spectra) a shoulder arises at 397.1 eV

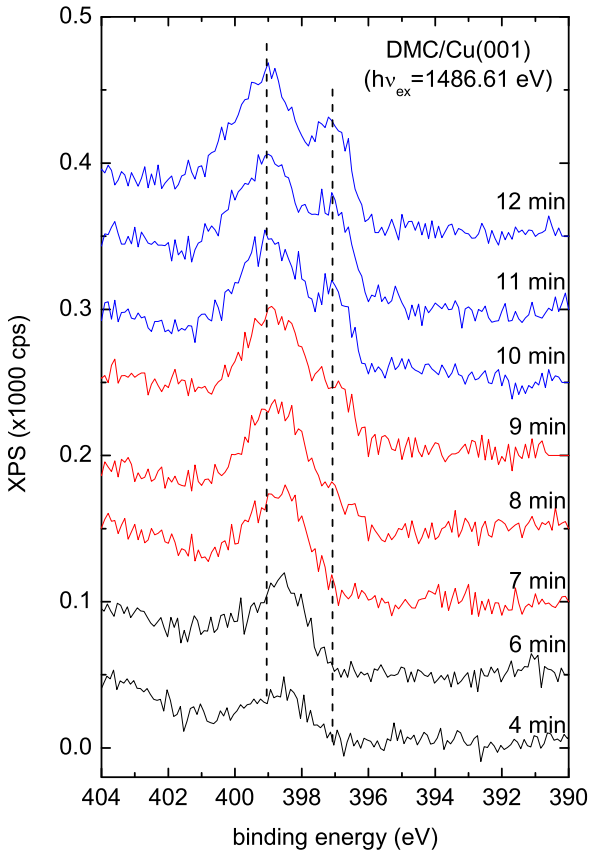

Figure 4.25: *N 1s spectra for the different evaporation steps that correspond to the C 1s/Cu 3p$_{3/2}$ intensity ratios given in Fig. 4.24. The colors of the spectra indicate the regions of different evaporation rates as they were found by the evaluation of the C 1s/Cu 3p$_{3/2}$ intensity ratios.*

while the main peak starts to shift two 399.5 eV. For the spectra of the third region (blue spectra) the overall shape remains the same which corresponds to the saturation in coverage that is visible in Fig. 4.24. This strongly supports the former assumption that there are more than two types of interaction (one adsorbate–substrate + one adsorbate–adsorbate) involved in the adsorption of DMC on Cu(001), and that the dominating interaction depends on the thickness.

4.3.2.2 Temperature-dependent adsorption

As demonstrated by the XPS measurements presented in Fig. 4.25, Cu(001) reveals its more reactive character with the ability of stronger molecule-substrate interactions compared to Au(111). Thereby, chemisorption of organic molecules on Cu(001) is quite likely to happen at room temperature, whereas for sufficiently low temperatures the thermal energy might not be large enough to overcome the activation barrier for the chemical bond forma-

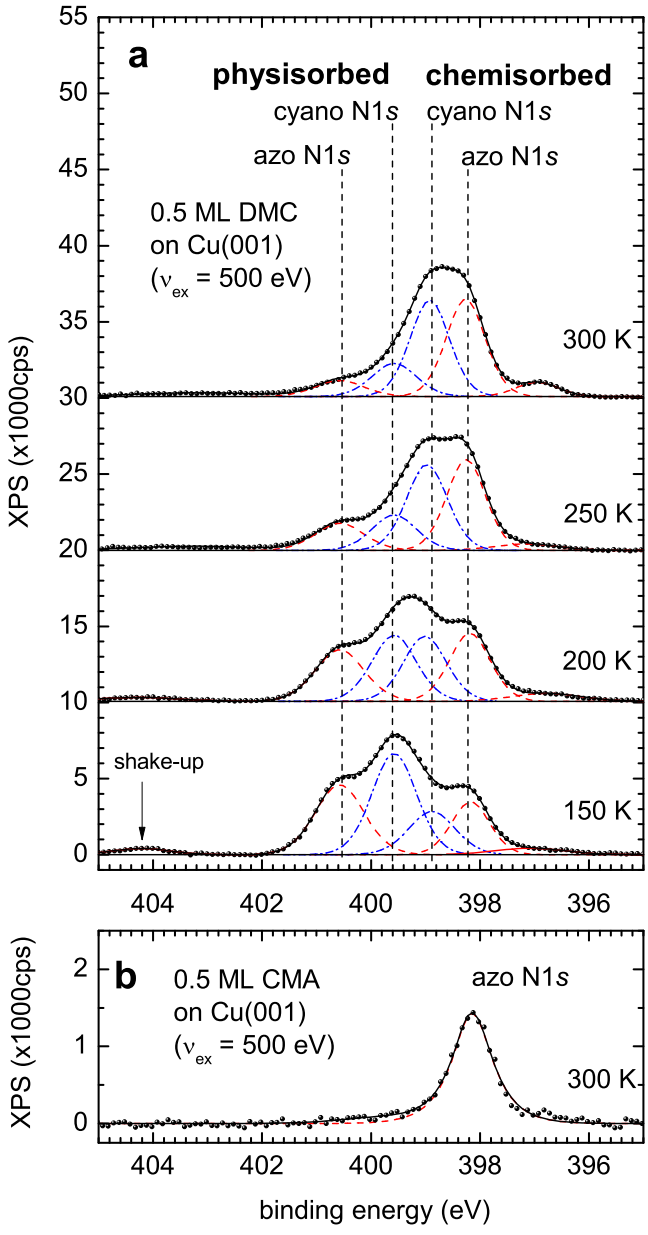

Figure 4.26:
(a) Temperature-dependent N 1s XPS of 1 ML DMC molecules evaporated on Cu(001) at 150 K. Spectra are shifted vertically for clarity. (b) N 1s XPS signal from 1 ML CMA molecules evaporated on Cu(001) at 300 K. Red dashed and blue dotted lines correspond to the fitted components that can be assigned to the azo and cyano N 1s excitation centers, respectively. Vertical dashed lines indicate the positions of the different physisorbed and chemisorbed species.

tion. Thus, we studied the temperature dependence of the adsorption state of DMC molecules on Cu(001) in a temperature range between 150 K and room temperature. As a suitable coverage, the chosen thickness corresponds to the one of eight minutes evaporation time in Fig. 4.25.

In Fig. 4.26(a), the N 1*s* XPS spectrum 0.5 ML of DMC molecules evaporated on Cu(001) at 150 K is shown after the substrate has been annealed to different temperatures. At 150 K, four different peaks are needed to fit the main spectrum in the region between 397 eV and 402 eV. The energy positions of the two peaks at higher binding energies of 400.5 eV and 399.6 eV are comparable to the ones of the azo and the cyano N 1*s* binding energies found for physisorbed DMC molecules in a multilayer on Cu(001) (*cf.* Fig. 4.18). An additional weak shake-up resonance is present at around 404.2 eV, at a distance of 3.7 eV to the closest XPS peak. This value is identical to the distance between the shake-up and the azo N 1*s* peak for multilayer DMC on Cu(001). We thus conclude that a substantial fraction of the molecules is physisorbed on the surface, which leads to the perfect agreement of the XPS intensity above 399 eV with the corresponding spectrum of a multilayer DMC on Cu(001) [Fig. 4.18(a)].

Two additional peaks, separated by 0.6 eV, are found at lower energies of 398.2 eV and 398.8 eV. A shift of the binding energies to lower values is generally expected to be caused by chemisorption on metallic substrates [79]. A possible chemical shift due to fuctional groups is in this case overcompensated by the electron donation from the substrate [80]. This might be the case for the center of the DMC molecule. Furthermor, the same surface-induced chemical shift would be expected for CMA if it is chemisorbed in the same way. The N 1*s* XPS signal of 0.4 ML CMA evaporated on Cu(001) at room temperature [Fig. 4.26(b)] shows an energy shift of 1.3 eV to lower binding energies compared to the one of CMA on Au(111), indicating chemisorption of the CMA molecules on Cu(001). Correspondingly, the peak of CMA on Cu(001) at 398.2 eV coincides in energy with the rightmost peak of DMC at 150 K, so that we can assign the peak at 398.2 eV to the azo N 1*s* core level ionization of DMC. As a result, a change in the order of the azo and the cyano N 1*s* signals appears, if compared to the physisorbed DMC, which implies that the rest groups are much less influenced by the effect of electron donation from the surface. We conclude that at 150 K there is a mixture of chemisorbed and physisorbed DMC molecules, where the former are bound at the Cu(001) surface via their azo group.

At higher temperatures, the amount of chemisorbed DMC increases at the expense of the physisorbed species, according to the change in the peak

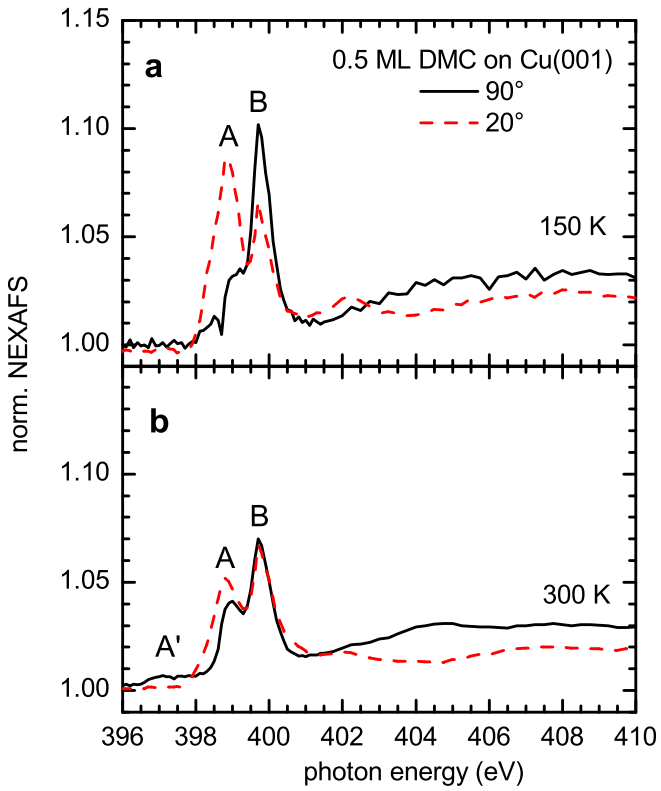

Figure 4.27: *Temperature-dependent NEXAFS spectra of 0.5 ML DMC molecules evaporated on Cu(001) at 150 K (a) and after increasing the temperature to* 300 *K (b). Continuous (dashed) lines correspond to spectra at* 90° *normal (*20° *grazing) X-ray incidence.*

ratio. The transformation is almost complete at 250 K, but a small amount of physisorbed DMC is still recognizable even at 300 K. This remnant of physisorbed molecules probably exists because they cannot approach the surface appropriately in order to form a bond with the substrate. Furthermore, the shake-up resonance vanishes during the chemisorption process, indicating a change in the electronic structure at the azo center (*cf.* Sec. 4.3.1.2).

Obviously, the XPS data suggest, that a mixture of physisorbed and chemisorbed DMC molecules are present on Cu(001) at 150 K. The corresponding NEXAFS spectra for 0.5 ML DMC molecules on Cu(001) at 150 K are shown in Fig. 4.27(a). The contribution of the physisorbed species can be assimilated to the one of DMC molecules on Au(111), so that differing features can be assigned to the chemisorbed phase. The different shapes observed for peak A at 398.7 eV for grazing and normal incidence geometries can be explained by considering that there are two contributing resonances [similar to the peak around 398.8 eV in the spectrum of DMC on Au(111) in Fig. 4.19(a)]. At lower energies, the azo π^* orbital remains out of the surface plane, but the lower intensity of peak A with respect to the in-plane resonance at 399.7 eV,

labeled as peak B, implies a weakening of the N=N double bond, caused by a bond formation with the metallic substrate [30]. In contrast, the shoulder at 398.9 eV in the normal-incidence spectrum of the out-of-plane cyano orbital evidences that the benzonitrile moieties are tilted out of the surface plane. This also results in the modified angle dependence of peak B of the in-plane cyano orbital, which can be explained by the formation of bonds between the azo center and the metallic substrate that force the molecule to adopt a different orientation on the surface. In addition, the intermolecular interactions can have an influence on the orientation of the benzonitrile moieties.

The NEXAFS spectra at 300 K (panel b) exhibit an enhancement of the characteristic features of the chemisorbed species. The absence of any angle dependence of peak B can be explained by the fact that the majority of DMC molecules is chemisorbed, as evidenced by XPS, and all DMC molecules are either uniformly ordered with an angle of 35.3° between the in-plane orbital and the surface plane (magic angle for linearly polarized light), or completely disordered. However, the presence of a residual angle dependence of peak A favors the former scenario. The total cross section, which can be estimated roughly by adding the intensity of grazing and the double intensity of normal incidence, is decreased for peak B at 399.7 eV when going from 155 K to 300 K. From the examination of the C $1s$/Cu$3p_{3/2}$ XPS intensity ratios we know that the amount of carbon and thus the molecular coverage does not change during annealing to room temperature. We thus explain the lower total adsorption intensity by the convolution of peak B with contributions of the much broader peak A. Due to the discussed decrease in intensity of feature A during annealing, the intensity of peak B appears smaller although its total cross section does not change.

So far, we can conclude that DMC binds via its azo center with the Cu(001) surface. In order to elucidate whether the surface–molecule or the intermolecular interactions dominate, the conformational effect, we varied the molecular coverage at the surface as it will be shown in the next section.

4.3.2.3 Thickness-dependent adsorption

In Sec. 4.3.2.1 a series of thickness-dependent low-resolution XP spectra was already presented as a survey, in order to study the global adsorption behavior of DMC on Cu(001). The different spectral features that were found for different coverages are related to different adsorption states. It is possible to get further information of the two different adsorption phases by conducting high-resolution XPS measurements for the different coverages. Here the XPS peak assignment from the temperature-dependent studies can be used as a

starting point for the peak analysis.

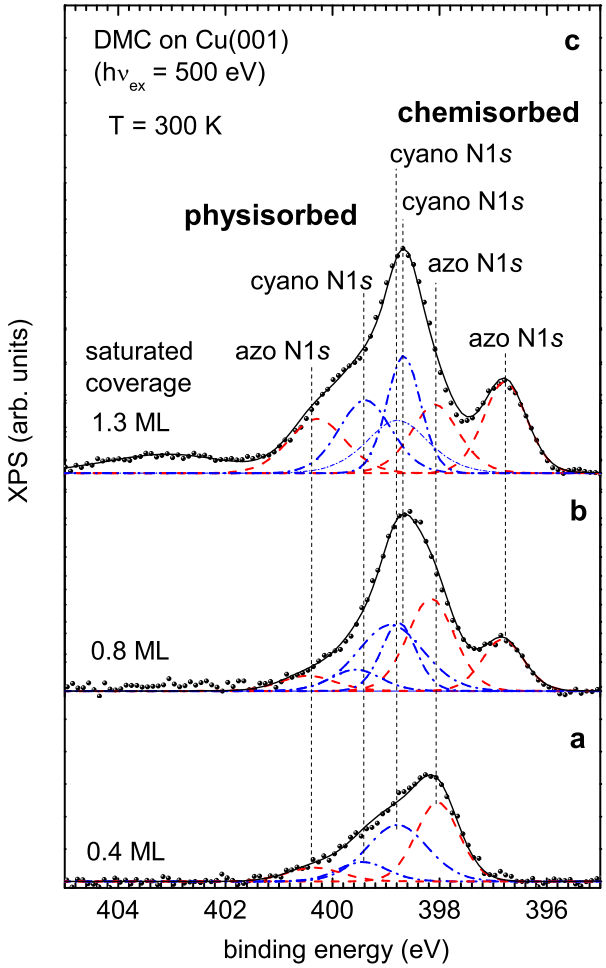

Figure 4.28: *Sequence of N 1s XPS spectra taken during stepwise evaporation of DMC on a Cu(001) substrate at room temperature. Red dashed and blue dotted lines correspond to the fitted components that can be assigned to the azo and cyano N 1s excitation centers, respectively. Vertical dashed lines mark the positions of the different physisorbed and chemisorbed species.*

The corresponding N 1*s* XPS of 0.4 ML DMC molecules evaporated on Cu(001) at 300 K is given as the lower spectrum in Fig. 4.28. The peak assignment of the spectrum is similar to the one of 0.5 ML at room temperature in the temperature-dependent measurement with a dominating signal between 398 eV and 399 eV (*cf.* Fig. 4.26). For the 0.4 ML DMC evaporated at room temperature the contribution of physisorbed DMC at higher binding energies is smaller, so that the overall spectral shape appears more asymmetric. As a noticeable difference, the spectrum of 0.5 ML [topmost curve of Fig. 4.26(a)] exhibits a small shoulder at 397 eV, which may come from an additional species that only appears at higher coverage.

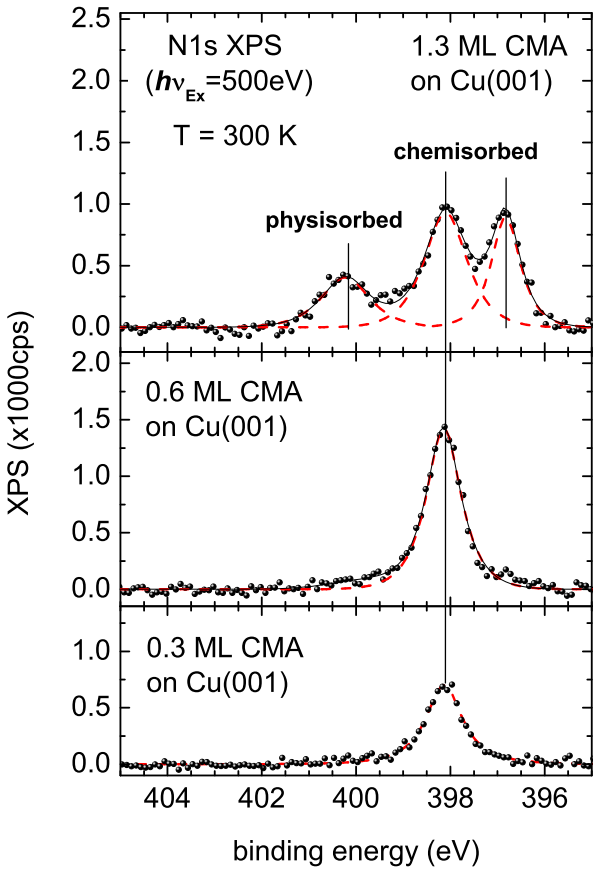

Figure 4.29: *Sequence of N 1s XPS spectra taken during stepwise evaporation of CMA on a Cu(001) substrate at room temperature. Red dashed lines correspond to the fitted components that can be assigned to the azo center. Vertical black lines mark the positions of the different physisorbed and chemisorbed species.*

As middle spectrum of Fig. 4.28 the N 1*s* XPS of DMC for higher coverages is given. For 0.8 ML (middel panel) an additional peak at 397 eV appears at the same energy position as the shoulder in the spectrum of 0.5 ML coverage discussed above. Obviously a new species starts to grow in the presence of the flatly chemisorbed DMC. Consequently, three different pairs of azo and cyano XPS peaks have to be considered in the fitting procedure, belonging to the small amount of physisorbed DMC and to the two chemisorbed species that appear consecutively with increasing coverage. By further deposition of DMC up to the saturation coverage for the adsorption at room temperature the intensity of the peak at 397 eV increases further, as shown in the upper part of Fig. 4.28. At the same time the amount of molecules from the low-coverage chemisorbed species remains constant. Additionally an increase of the number of physisorbed molecules is observed, very likely accumulated into a second layer. The intensity of this species contributes with one fourth to the entire spectrum. Thus we refer to this coverage as 1.3 ML. For all other

samples the coverages were calibrated with respect to this saturated layer.

The confirmation of the previous N 1*s* XPS peak assignment of DMC on Cu(001) comes from the corresponding thickness dependent N 1*s* XPS of CMA on Cu(001) shown in Fig. 4.29. As already discussed in the previous sections, the CMA molecule only exhibits one type of N 1*s* excitation center. Assuming that all molecules are equivalently adsorbed and that both nitrogen atoms of the azo bridge bond to the substrate in the same way, only one singel peak should appear as it can be seen at a binding energy of 398.2 eV in the lower two panels which show the XP spectra for coverages of 0.3 ML and 0.6 ML. For the saturated coverage two additional species at 397.0 eV and 400.5 eV are present beside the central peak. The energetic positions of all three peaks are in accordance with those of the azo N 1*s* peaks in the spectrum of 1.3 ML DMC on Cu(001) (*cf.* Fig. 4.28). This indicates that the adsorption behavior of both azobenzene derivatives is the same in spite of the different intermolecular interactions caused by the different rest groups. The only slight difference is that for CMA no physisorbed molecules are found in the low-coverage phase.

A decrease of the intensity for higher coverage is found when comparing the signals of the central peak at 398.2 eV for 0.6 ML and 1.3 ML . Thus we have to conclude that a noticeable part of the initially chemisorbed species is transformed to the high-coverage species represented by the peak at 397.0 eV. In view of the two chemisorbed species visible at 397.0 and 398.2 eV in the XP spectrum of the saturated monolayer, a pair of scenarios can be considered when going from 0.6 ML to 1.3 ML coverage. In the first scenario additionally adsorbing molecules may be forced by the already present adsorbate to bind in another way to the surface copper atoms than those that are already adsorbed. Additionally, a certain amount of molecules of the already present adsorbate are forced to change their adsorption state which leads to a decrease of the signal at 398.2 eV. Alternatively, another scenario could be assumed in which the two peaks at 398.2 eV and 397.0 eV belong to the same adsorbate species of molecules with the two nitrogens of the central azo bridge asymmetrically bond to the surface copper atoms. In the latter case the N 1*s* binding energy of one nitrogen atom would match with the ones of the azo bridge of the previously adsorbed molecules at lower coverages. This is, however, most unlikely, since the chemical environment is expected to change for both azo bridge nitrogens going from the symmetrically to the unsymmetrically adsorbed case.

The corresponding sequence of O 1*s* XPS for different coverages is shown in Fig. 4.30. A characteristic double peak originates from the two inequivalent O 1*s* core levels located in the ester rest group. The energy difference of 2.0 eV is the same as for CMA on Au(111). Nevertheless the hight of the two features

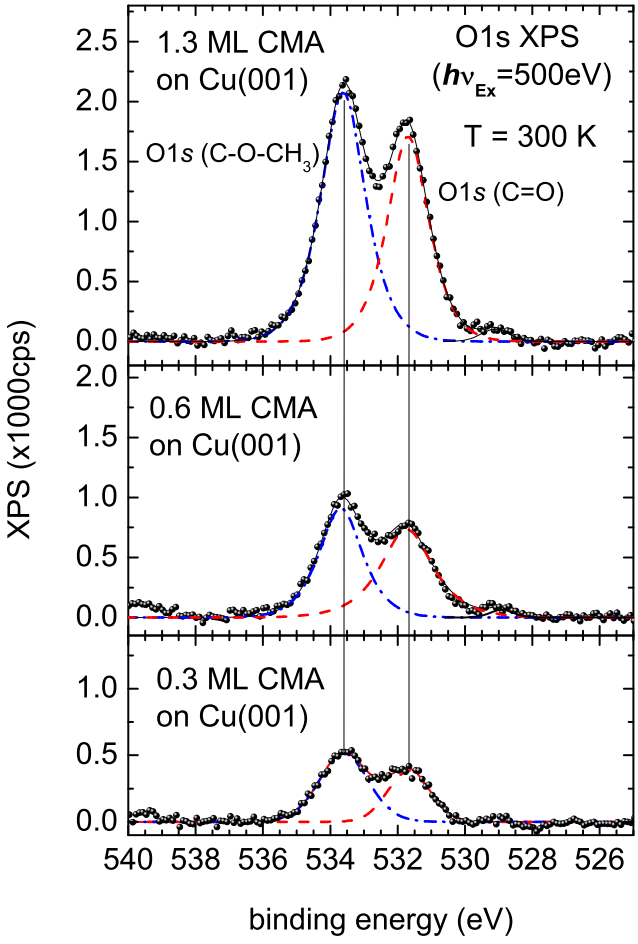

Figure 4.30: *O1s XPS spectra taken during stepwise evaporation of CMA on a Cu(001) substrate at room temperature. Red and blue lines represent the fitted components that can be assigned to the C=O and the C-O-CH_3 O 1s excitation centers. Vertical black lines mark the positions of the different excitation centers.*

is different as it can be seen in all three spectra. Since this peculiarity is not found for CMA on Au(111), a molecular shake-up resonance (as found in the N 1*s* XPS of CMA on Au(111)) arising at the expense of the O 1*s* XPS signal can be excluded. This is supported by the fact that the difference in peak intensity decreases when the coverage approaches 1.3 ML. This can be easily explained by the contribution of the physisorbed phase which should have the same peak ratio as the physisorbed phase on Au(111). However, the inequivalent signal heights at 531.6 eV and 533.3 eV caused by the presence of the Cu(001) surface, might either come from a vibrational broadening or a plasmonic side band (which would appear beyond the region of the given graph), both due to the electronic coupling to the substrate. Both has been considered in fit procedures by different constraints all leading to satisfying results. The intensity present at 540 eV might be assigned to excitations of surface plasmons coupled to the

core-level ionization, since they appear for weakly surface-coupled systems [81] and with additional energies of in the order of magnitude of 10 eV [82]. The same characteristic XPS-peak broadening is found for the cyano rest groups of the low-coverage species of DMC chemisorbed on Cu(001) (*cf.* Fig. 4.28). There the fit gives a sufficiently good result only if the cyano component of the low-coverage species is reduced in height. Although an influence of the metallic environment is found on shape and intensity of the XPS signals of the rest groups, there is no indication about covalent interaction with the surface. Thus the biggest influence of the metal surface interaction is observed at the molecular azo center.

Further insight into the two different chemisorption states is expected from the NEXAFS, since it reflects the configuration of the unoccupied molecular states and thus provides a more complete picture of the chemical states.

4.3.2.4 Adsorption at low coverages

In order to study individually the molecule–surface interaction, we evaporated 0.4 ML of CMA and DMC molecules on the Cu(001) surface at room temperature, where it is likely that chemisorption takes place before the molecules can form islands. The corresponding NEXAFS spectra are shown in Fig. 4.31(a) and (b), respectively. For the physisorbed species of CMA molecules on Au(111), the NEXAFS spectrum exhibits only one sharp π^* resonance below the ionization barrier at 398.2 eV photon energy, as it was shown in Fig. 4.21 of Sec. 4.3.1.2. For a submonolayer on Cu(001) at room temperature, this π^* resonance is substituted by two resonances of lower intensity, as it can be seen in Fig. 4.31(a), attesting the weakening of the central azo π bond. The formation of bonds between the nitrogen atoms and the Cu(001) surface is also reflected by the broad spectral shape of those two resonances that can be assigned to the hybridization of the involved orbitals. From the angle dependence of these features, it is evident that they remain oriented mainly perpendicular to the surface, implying that the adsorbate–surface bonding character is σ-like. While the N K-shell NEXAFS spectra on Cu(001) prove the chemisorption of CMA, the O K edge, shown in Fig. 4.32, does not show any substrate dependence except for the difference in orientation (compare to Fig. 4.16 and 4.22). Here the rest groups appear to be tilted out of the surface plane. From the detailed analysis of the angle dependence, the angle between surface normal and the involved π^* orbital at 531.7 eV is found to be 35°. This is a strong indication that the rest groups are not involved in the chemisorption process.

In the case of DMC, the two non-equivalent nitrogen excitation centers contribute differently to the N K-shell NEXAFS spectra, which can be com-

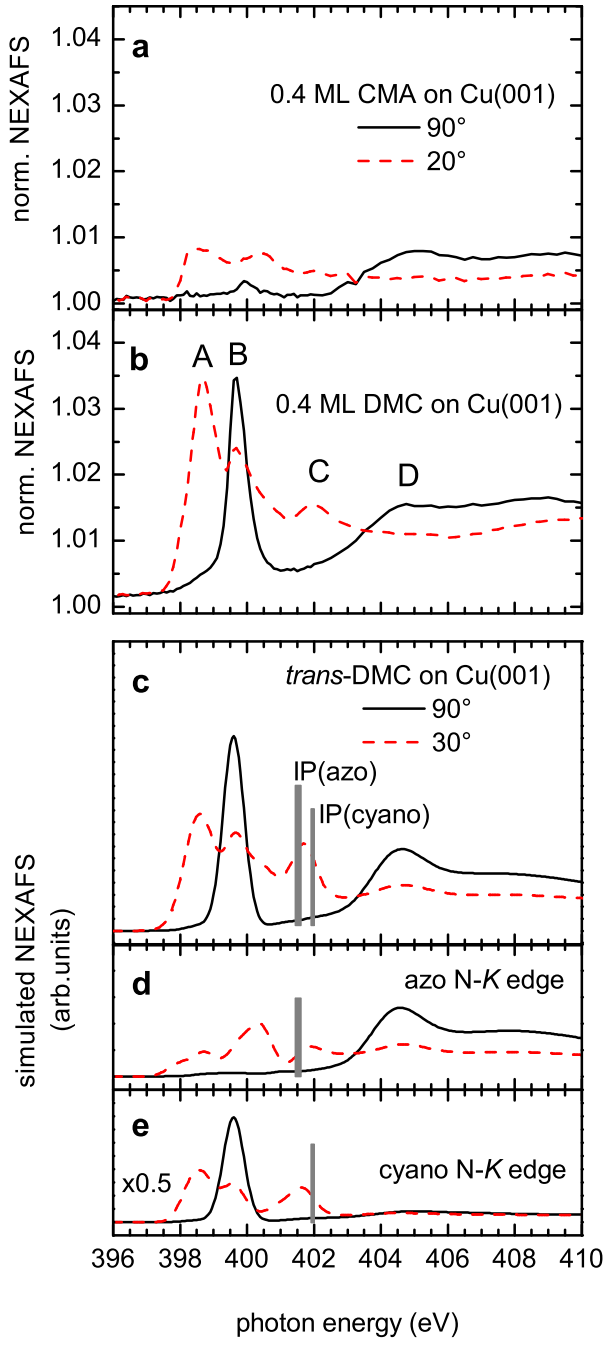

Figure 4.31: *N K-shell NEXAFS spectra measured for 0.4 ML of CMA (a) and DMC molecules (b) deposited on Cu(001) at room temperature. (c) Simulated NEXAFS spectra for a single DMC molecule on a Cu(001) cluster, in which the contributions of the azo (d) and the cyano (e) excitation centers are plotted individually. Gray bars mark the corresponding ionization barriers. Continuous lines correspond to spectra acquired or simulated for* 90° *normal X-ray incidence while dotted lines correspond to the spectra measured under* 20° *grazing and simulated for* 30° *grazing X-ray incidence.*

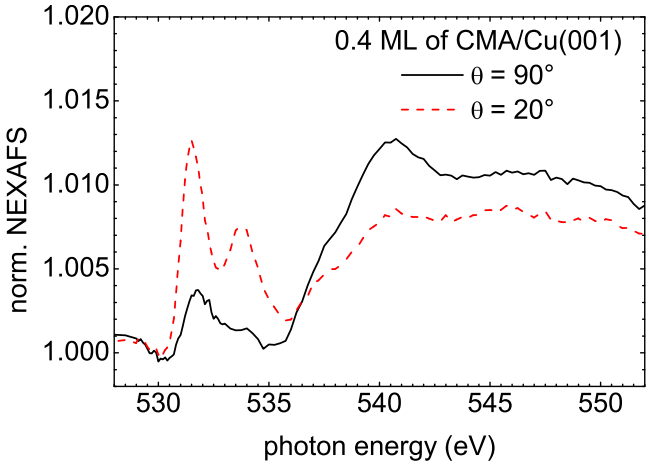

Figure 4.32: *Angle-dependent O K edge absorption spectra of 0.5 ML of CMA molecules evaporated on Cu(001) at roomt temperature. Continuous (dashed) lines correspond to spectra at 90° normal (20° grazing) X-ray incidence.*

pared to the corresponding DFT calculations. The relaxed structure of a DMC molecule on a Cu_{68} cluster, see Fig. 4.33, shows that the azo center is attracted to the two central Cu atoms, and that the outer parts are tilted by 9° with respect to the surface plane. This leads to a distortion of the crystalline Cu structure with atom displacements below 0.5 Å. In addition, the N=N bond is stretched from 1.287 Å to 1.339 Å by the attractive forces in the two N-Cu bonds.

The simulated angle-dependent spectra of a single DMC molecule on the Cu_{68} cluster [Fig. 4.31(c)] resemble strikingly well the experimental data of Fig. 4.31(b). The contributions of the azo and cyano N 1*s* excitation centers can be separately identified (panels d and e). Compared to the simulated spectra on Au(111), a clear change in the overall azo N *K* edge spectra is evident, whereas the cyano contributions are rather unperturbed. Similar to the measured spectra of CMA on Cu(001), the single π^* resonance of the DMC azo N *K* edge splits into two broad features due to the hybridization of the azo

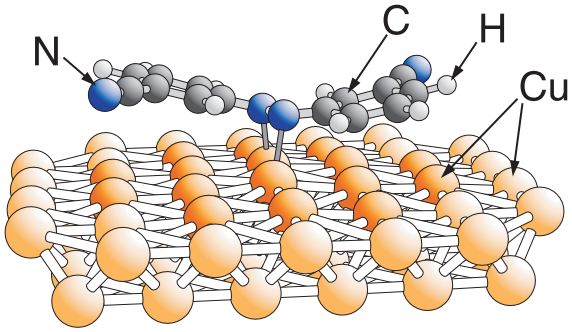

Figure 4.33: *Relaxed geometric structure of a single DMC azobenzene molecule on top of a Cu_{68} cluster, resulting from DFT geometry optimization. Darker and brighter substrate atoms were free and fixed during optimization, respectively.*

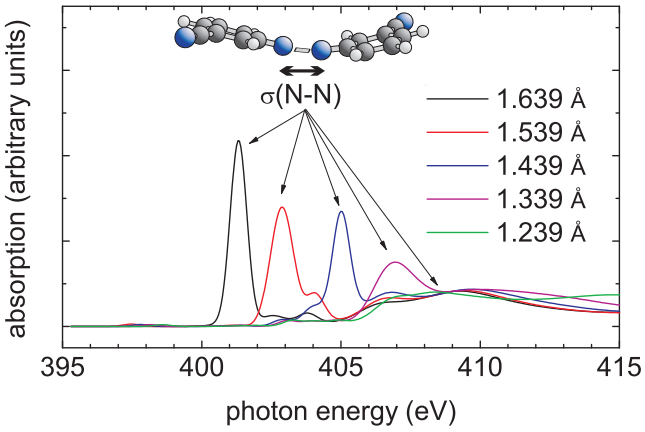

Figure 4.34: *Evolution of the σ shape resonance that is related to the central azo N–N σ bond as it is simulated for a single free DMC molecule in the adsorbate geometry. The azo N-N bond distance is varied in steps of 0.1 Å.*

π^* orbitals with the valence bands of the metallic surface. The peak at around 400.4 eV (panel d) is also visible as a shoulder of the cyano in-plane resonance in the measured DMC/Cu(001) spectrum for grazing incidence (panel b).

At 404.6 eV, there is a strong σ shape resonance visible for all spectra of 90° incidence in Fig. 4.31. This resonance is found to result from N1$s \rightarrow \sigma^*$(azo) transitions. The same resonance for gas phase and physisorbed molecules (see Fig. 4.19) turns out to be much weaker in intensity compared to the other spectral features, and is located at higher energies than on Cu(001). In order to ascertain the origin of this peculiarity, we calculated the NEXAFS of a DMC molecule of fixed geometry as for the adsorbate on Cu(001), but in the absence of the metal cluster. This yields the σ shape resonance at the same energy position as for the adsorbate system, as it can be seen in Fig. 4.34. Thus, we can exclude that a direct electronic interaction between the surface and the central molecular σ-bond orbital is responsible for this resonance. Another possible origin is the surface-induced bending of the molecular geometry, which reduces the overlap in the π bonds of the azo group. Together with the attracting forces between the azo nitrogen atoms and Cu(001), this increases the N–N bond distance and reduces the overlap in the N–N σ bond, resulting in a lower energetic splitting between the σ and the σ^* levels. It is worth to note the very high sensitivity of the energy position of this σ^* shape resonance on the N–N bond distance, with a calculated value of 20 eV/Å. At this point, we have to remark that we found the DMC molecules at a coverage of 0.4 ML much more flat on the surface than in the case of 0.5 ML. Obviously the stronger lift-up of the benzonitrile moieties out of the surface plane is not only caused by the bond formation to the surface, but seems to be also influenced by the molecular density in the organic layer.

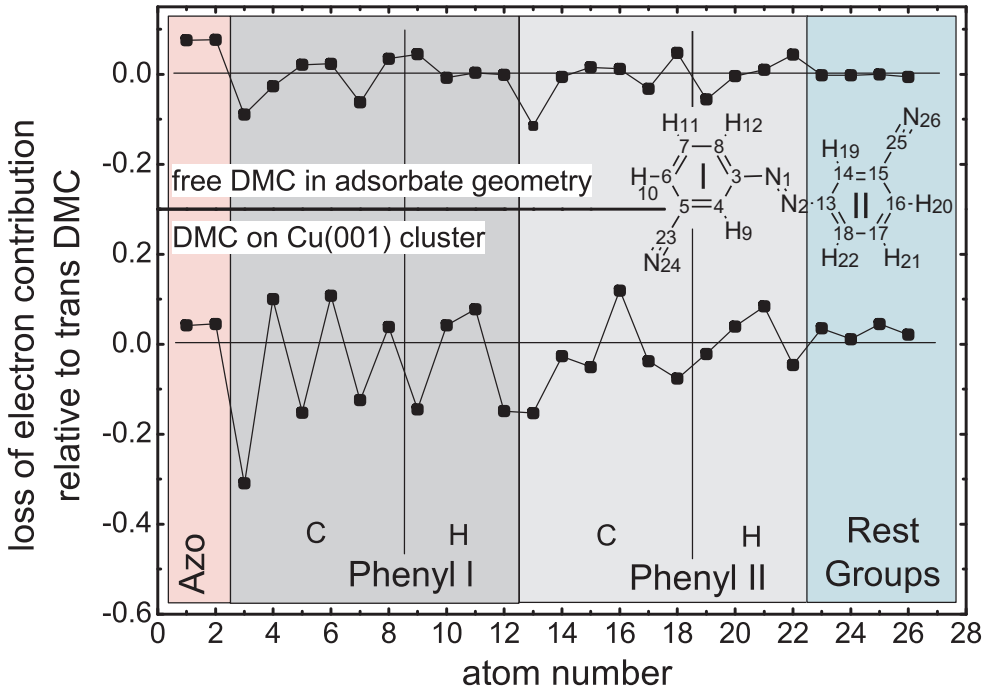

Figure 4.35: *Electron-redistribution diagram. The upper curve shows the change in electron density due to the bending of the molecular structure from the planar gas-phase trans geometry to the butterfly-like one of the chemisorbed low-coverage DMC species. The lower curve shows the change in electron density due to the bond formation to the surface. The atom numbers agree with those in the molecular structure in the inset. Negative values indicate electron loss at the corresponding atomic sites.*

4.3.2.5 Adsorption mechanism

Since the adsorption state is found to be common for both azobenzene derivatives and thus independent from the rest groups, a more general picture of the adsorption of azobenzene on Cu(001) can be established. In addition to the NEXAFS simulation of the DMC/Cu_{68}, the ground state of this model system was calculated using the all-electron basis sets for C, N, and H (described in Sec. 3.2.4), while keeping the basis set configuration of Cu. Concomitantly, a *Mulliken* population analysis of the calculated orbital configuration was conducted in order to analyze the bond structure, in particular at the center of the molecule.

The adsorption can be assumed as a combination of two correlated processes, the conformational change from the planar *trans* DMC to the butterfly-like geometry, and the bond formation of the adsorbate molecule to the Cu(001)

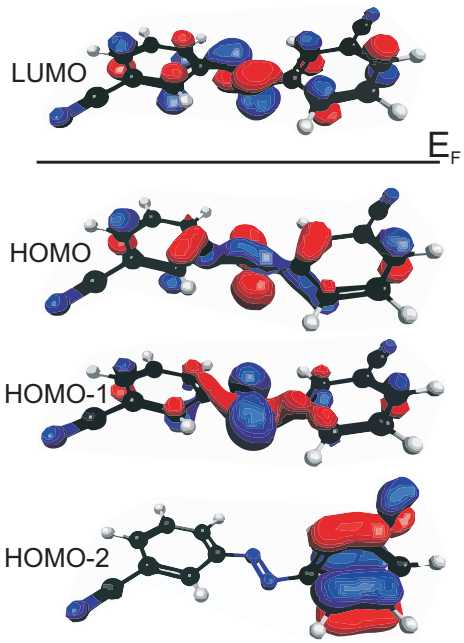

Figure 4.36: *Frontier orbitals of a free DMC molecule in adsorbate geometry. The horizontal black line markes the Fermi level.*

surface. Therefore, the change in electron density at each atomic center is shown for both processes in Fig. 4.35. The change in the electron distribution that is caused by going from the planar to the bent butterfly-like DMC is given in the upper curve. Only a slight charge transfer can be observed, mainly from the azo-linked carbon in the phenyl ring to the neighboring nitrogen. The bent non-planar structure that provokes the rehybridization of the atomic orbitals in the center of the molecule is accountable for this. Two new orbitals are formed, including both contributions from the original sp^2 hybridized non-bonding HOMO and the π HOMO-1 (*cf.* Fig. 4.10).

The resulting new frontier orbital configuration is given in Fig. 4.36. The rehybridization of the contributing atomic $2p$ orbitals leads to a reorientation of the molecular orbitals. For the new orientation the overlap in the corresponding adsorbate-surface σ bonds is optimized regarding the trapezoid arrangement of the Cu–N–N–Cu atoms (the N–N distance in the azo bridge is 1.339 Å, and that between the neighboring Cu atoms 2.602 Å). For a maximum coupling of the aromatic (phenyl) π orbital system to this central N-N orbital configuration, the benzene rings have to be tilted such that their π-orbital systems are parallel to the corresponding N–Cu σ bonds. The mixture of the bonding and non-bonding (gas-phase) orbitals leads then to the involvement of the non-bonding orbitals into the σ bond formation between adsorbate and substrate, and thus to an increase of bond energy. Vice versa, it can be argued

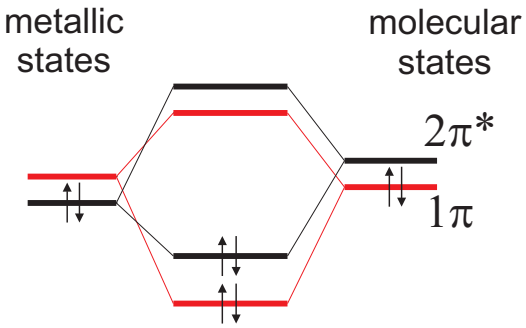

Figure 4.37: *Valence state structure in π-donation (red) + π*-back-donation (black) configuration introduced by Dewar, Chatt, and Duncanson [83, 84].*

that the reconfiguration of the HOMO and HOMO-1 and the correlated energy minimization, together with the repulsive forces between the phenyl rings and the substrate, causes the bending in the structure of the chemisorbed DMC molecule at low coverages. No conclusion from the calculations can be given here as to which extend the rehybridization of the atomic N 2*p* orbitals and the involvement of the lone-pair electrons contribute to the bonding mechanism. The LUMO remains mainly in its gas-phase configuration (*cf.* Fig. 4.10), since a rehybridization in this case would cost much more energy than what is gained by an optimization of the orbital overlaps.

The lower curve in Fig. 4.36 shows the change of electron contribution to the single atom centers going from the free DMC in adsorption geometry to the adsorbed system. The integration over all atomic centers yields a decrease of the total electron density of 0.784 *e*, due to the bond formation to the surface. This electron loss is conspicuously inhomogeneous. While the decrease of total electron density dominates at the azobenzene backbone, an increase of local electron density at the *ortho* and *para* positions, as well as at the central azo bridge, can be observed. The distribution pattern coincides with the localization of the LUMO of the isolated azobenzenes. This suggests that the LUMO exhibits an electron accepting character. In addition, the electron density is slightly increased at the rest groups. The higher electron density agrees well with the shifts of the N 1*s* binding energies that were measured by XPS for chemisorbed DMC and CMA.

The electron donation to the surface and back can be explained with a model introduced by *Dewar, Chatt, and Duncanson* (DCD model) [83, 84]. A schematic diagram is given in Fig. 4.37. According to this model, an occupied molecular orbital mixes with an unoccupied one of the metal, leading to the donation of electrons to the latter one. Vice versa, an occupied metallic orbital of the metal mixes in the present case with the azobenzene LUMO back-donating electrons of the organic adsorbate. Since the mixing orbitals have to be close in energy, the donation—back-donation only appears close to the

Fermi edge. Naturally, the mixing orbitals must exhibit the same symmetry. This implies that the HOMO can not donate electrons directly to the LUMO, but only transmit them via the substrate.

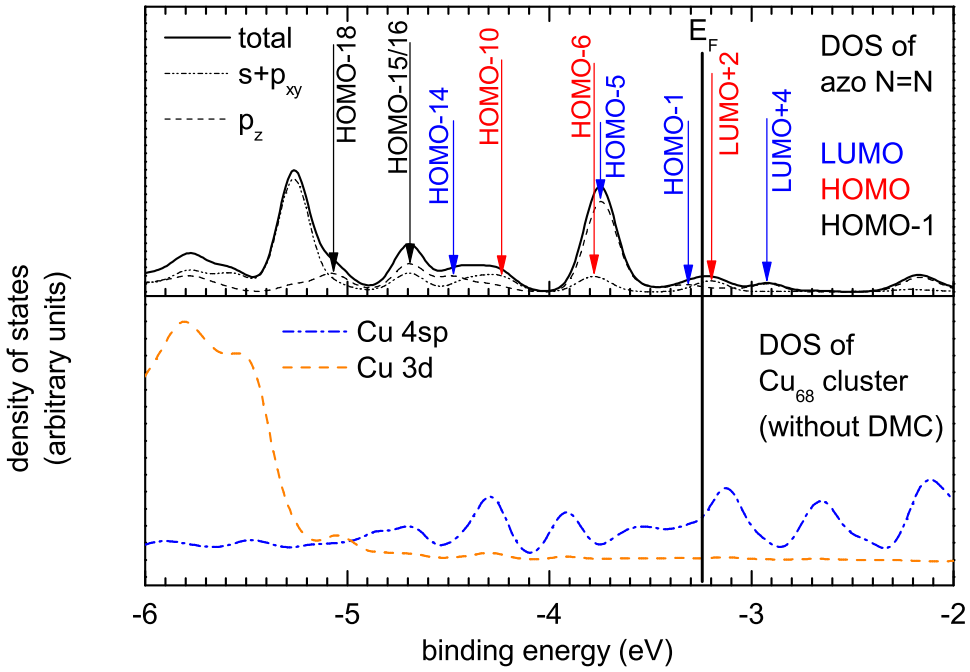

Figure 4.38: *Upper panel: partial density of states (PDOS) of the azo N=N bridge. Dotted and dashed lines show the contributions of the corresponding atomic N* $2s+$ *N* $2p_{xy}$*, and the N* $2p_z$ *orbitals, respectively. The features in black, red, and blue have been assigned to contributions that resemble the character of the HOMO-1, HOMO, and LUMO gas-phase trans DMC (see procedure in the text). Lower panel: blue and orange curves show the contributions of the Cu* $4sp$ *and* $3d$ *atomic orbitals to the density of states, respectively.*

The hybridization again follows a two-step path [85]. For noble metals, the valence electrons completely fill the Cu $3d$ band, and only partially the $4sp$ band. While for copper the former is placed between -5 eV and -2 eV below the Fermi level (*cf.* lower panel of Fig. 4.38), the much broader $4sp$ band has contributions around the Fermi edge [86] and can thus interact directly with the frontier orbitals of various organic compounds. Their partial occupations makes those $4sp$ states rather suitable for the π donation - π^* back-donation mechanism. The resulting hybrid orbitals can mix further with the $3d$ band. The strength of this mixing depends on the coupling between the metallic *sp*

and d orbitals. For the rather localized Cu $3d$ orbitals, the coupling is stronger than for the more extended Au $5d$. This accounts for the difference between the physisorptive behavior on Au(111) and the chemisorptive bond character on Cu(001), as it was observed for DMC and CMA.

The described bonding characteristic on Cu(001) is further confirmed by the simulated partial density of states (PDOS) in the that originates from the azo bridge (upper panel of Fig. 4.38). The ground-state calculation of the DMC/Cu_{68} results in discrete metal-organic states between the Cu $3d$ band and the Fermi edge. The orbital plots of these states exhibit certain symmetries that have to match the symmetry of the contributing molecular orbitals. Thus, metal-organic orbitals that exhibit contributions of the LUMO of the butterfly-like DMC (Fig. 4.36) can be easily distinguished from the HOMOs by the observation of the corresponding orbital plots. HOMO-1 and HOMO of the DMC in adsorbate geometry are similar in shape, since both are mixtures of the HOMO-1 and HOMO of the free *trans* DMC molecule (the latter are given in Fig. 4.10). However, these two HOMOs of the DMC in adsorbate geometry can be distinguished by a different characteristic contribution of atomic N $2p_{xy}$ and $2p_z$ orbitals. The HOMO exhibits a much stronger $2p_{xy}$ character than $2p_z$ character in contrast to the HOMO-1, for which the $2p_z$ contribution dominates. Each of the three frontier orbitals have thus a characteristic fingerprint and the metal-organic orbitals can be assigned, as indicated in the upper panel of Fig. 4.38. The energetic position of the assigned contributions can help to analyze the calculated bond configuration. In contrast, the plotted intensities in the upper panel of Fig. 4.38 are not meaningful, since only the contributions of the azo bridge nitrogen atoms are plotted here, and while those of the phenyl ring have been disregarded[2].

Both HOMO and LUMO split to components below and above the Fermi level. This confirms the suggested DCD model of π-donation — π^*-backdonation. The resulting (HOMO and LUMO) π^* orbitals are visible as the two π^* resonances between 397 and 401 eV in the measured N K-shell spectrum at 20° grazing X-ray incidence of low-coverage CMA layer on Cu(001), and in the calculated partial azo N K edge absorption at 30° X-ray incidence of DMC on Cu(001) (*cf.* Fig. 4.31). Furthermore, the energy position of the involved orbitals lies between the Cu $3d$ band and the Fermi level. This attests the mixture of the molecular orbitals preferably with the Cu $4sp$ band, and the subsequent mixing of the resulting adsorbate+Cu $4sp$ species with the Cu $3d$ band.

[2]The contributions of the phenyl rings have to be excluded from this consideration, since they originate from both the azo and cyano orbital system.

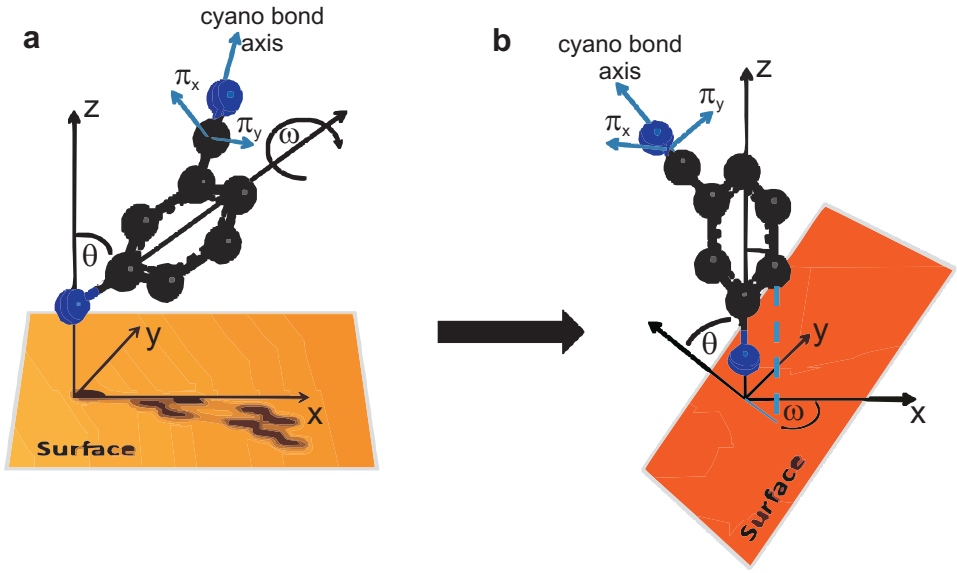

Figure 4.39: *Sketch of the transformation from the coordinate system with the surface in the x-y-plane to the one where the inner azo C-N bond points in the z direction.*

Finally, it has to be noted that DFT reveals that the DMC molecule bonds comparably weak to the Cu(001) surface. From the comparison of the calculated total energies of the separated (*trans* DMC) + (Cu_{57}(32,25)) and the (joined) adsorbed DMC on Cu(001) system, the binding energy was found to be 0.77 eV. In contrast, the calculated binding energy of 6.17 eV of DMC at the azo bridge is much larger. Similar values are found for different thermolysis scenarios of azobenzene [87]. The assumption that the main contribution of the N=N binding energy originates from the corresponding σ bond is confirmed by the relatively small change of the N–N bond length of about 10%.

4.3.2.6 Molecular orientation

As already mentioned in Sec. 4.2.1, the benzonitrile moiety exhibit two orthogonal π^* orbitals (π_x and π_y as defined in Fig. 4.8 and 4.9). Their measured orientation can be used to get the full azimuthal orientation of the benzonitrile moiety of DMC on the metallic surface. This orientation, on the other hand, is well defined by the tilt angle ϑ and the angle ω that describes the rotation of the phenyl ring around the central azo C–N bond axes, as shown in Fig. 4.39(a).

An easier mathematical description is obtained when using spherical coordinates and assuming the azo C–N bond axis in z direction. The desired

transformation is sketched in Fig. 4.39. In this picture the tilt angle ϑ coincides with the zenithal component of the spherical coordinates, and ω is given by the corresponding azimuthal contribution in the resulting x-y-plane plus a arbitrary phase as initial condition. If the surface normal $\vec{\mathbf{n}}$ is defined as:

$$\vec{\mathbf{n}} = (0, \sin\vartheta, \cos\vartheta), \tag{4.3}$$

the description of the normalized orientation vectors $\vec{\mathbf{p}}_o$ for the π_x orbital and $\vec{\mathbf{p}}_i$ for the π_y orbital can be derived from simple geometric considerations as:

$$\begin{aligned}\vec{\mathbf{p}}_o(\omega) =& (\cos(\varphi)\sin(\vartheta), \sin(\varphi)\sin(\vartheta), \sin(\vartheta))|_{(\vartheta=\frac{\pi}{2}, \varphi=\omega+\frac{\pi}{2})} \\ =& (-\sin(\omega), \cos(\omega), 0),\end{aligned} \tag{4.4}$$

$$\begin{aligned}\vec{\mathbf{p}}_i(\omega) =& (\cos(\varphi)\sin(\vartheta), \sin(\varphi)\sin(\vartheta), \sin(\vartheta))|_{(\vartheta=\frac{\pi}{6}, \varphi=\omega-\pi)} \\ =& (-\frac{1}{2}\cos(\omega), -\frac{1}{2}\sin(\omega), \frac{\sqrt{3}}{2}),\end{aligned} \tag{4.5}$$

where $\vec{\mathbf{p}}_o$ and $\vec{\mathbf{p}}_i$ are normalized and orthogonal. In view of the mentioned phase constant for ω it is also obvious that for $\vartheta = 90°$ and $\omega = 0°$, the benzene plane is parallel to the surface.

The orientations of π_x and π_y with respect to the surface normal are known from the angle-dependent NEXAFS and labled here as the angles δ (for π_x) and γ (for π_y), respectively. These two angles correspond to the angle Θ of the polar orbital orientation that was introduced in Sec. 2.2.2. These angles are related to ϑ and ω by the scalar product between $\vec{\mathbf{p}}_o$ and $\vec{\mathbf{p}}_i$ and the vector $\vec{\mathbf{n}}$ of the surface normal:

$$\begin{aligned}\cos(\delta) &= \vec{\mathbf{p}}_o \,.\, \vec{\mathbf{n}} \\ &= \sin(\vartheta)\cos(\omega),\end{aligned} \tag{4.6}$$

$$\begin{aligned}\cos(\gamma) &= \vec{\mathbf{p}}_i \,.\, \vec{\mathbf{n}} \\ &= \frac{\sqrt{3}}{2}\cos(\vartheta) - \frac{1}{2}\sin(\vartheta)\sin(\omega).\end{aligned} \tag{4.7}$$

The solution space of both equations (shown in Fig. 4.40) is countable infinite, since periodic functions are involved. Thus, one has to clarify which subspace of solutions is physically meaningful by giving a reasonable range for the resulting angles that characterize directly the orientation of benzonitrile. For the adsorbed DMC the tilt angle ϑ cannot exceed 90°, since for higher angles

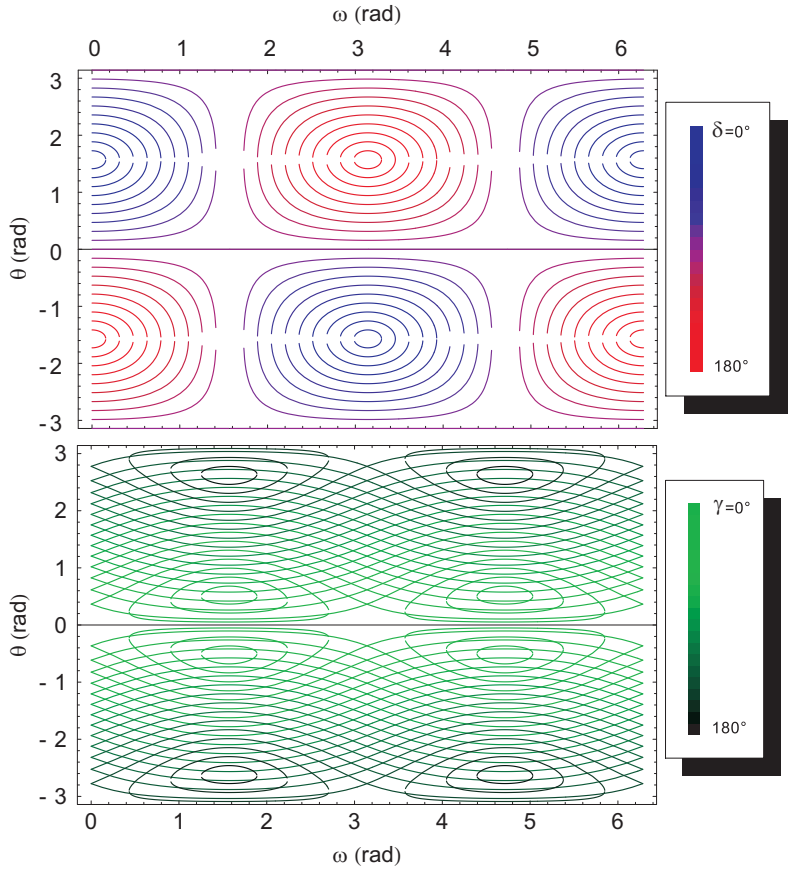

Figure 4.40: *Solution spaces of the two Eqs.* (4.6) *and* (4.7)*, where the different possible constellations of* ϑ *and* ω *for selected fixed orbital orientations* δ *and* γ *are given by the colored curves.*

the benzonitrile is placed in the substrate. The same counts for angles below $-90°$. For ω the restriction depends on ϑ. For $\vartheta = 90°$ the solution space is reduced to $\omega = 0°$, while for $\vartheta = 0°$, ω represents a purely azimuthal quantity and is thus arbitrary. Based on this consideration Fig. 4.41 displays the graph from wich ϑ and ω can be extracted for the given orbital orientations δ and γ as the intersection of the corresponding green and violett iso-angle lines.

With this tool at hand, the orientation of the chemisorbed DMC on Cu(001) with respect to the surface can be determined. The resulting values of δ, γ, ϑ, ω are summarized in Tab. 4.2. From the present orbital angles the solution for lift up ϑ and tilt ω is found in the upper left and right corners.

Regarding the overlap of transitions into azo—surface-bond orbitals and into the cyano π^* orbitals in π^* resonance region of the K K-shell NEXAFS, the

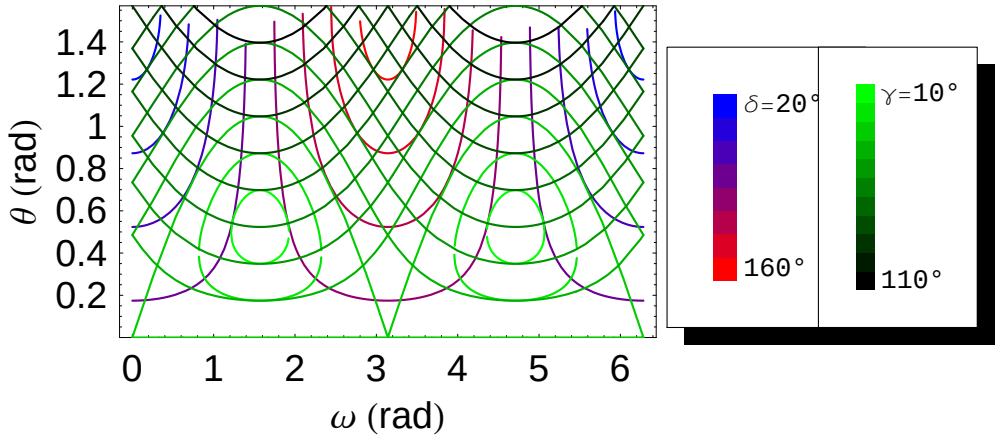

Figure 4.41: *Overlap of the iso-angle lines of the orbital orientations δ and γ in a adequate range of values of lift-up and tilt angles.*

determination of angles of the cyano π^* orbitals has to be done with due care. Since the azo—surface-bond orbitals are perpendicular to the surface, they only enhance the signal of grazing incidence of both in- and out-of-plane resonances. This leads to an overestimation for the angle δ and a underestimation for γ. Consequently the correct values for ϑ and γ would be even closer to the two upper corners of Fig. 4.41, *e.g.*, closer to the planar adsorption configuration.

4.3.2.7 Adsorption at high coverages

It was already seen in Sec. 4.3.2.3 that by doubling the coverage of DMC on Cu(001) to 0.8 ML, an additional species appears in the XP spectrum beside the butterfly-like chemisorbed molecules already present for 0.4 ML. It stands to reason that intermolecular interactions become important at higher packing densities on the surface and may influence the adsorption process. The corresponding angle-resolved N K-shell NEXAFS spectra are shown in

	δ	γ	ϑ	ω
experiment	$< 30°$	$> 60°$	$> 70°$	$< 10°$
theory			$60°$	$0°$

Table 4.2: *Summary of angles derived from angle-dependent measuredments of 0.4 ML DMC on Cu(001) (experiment) and from DFT-based geometry optimization of trans DMC on a Cu_{68} cluster (theory).*

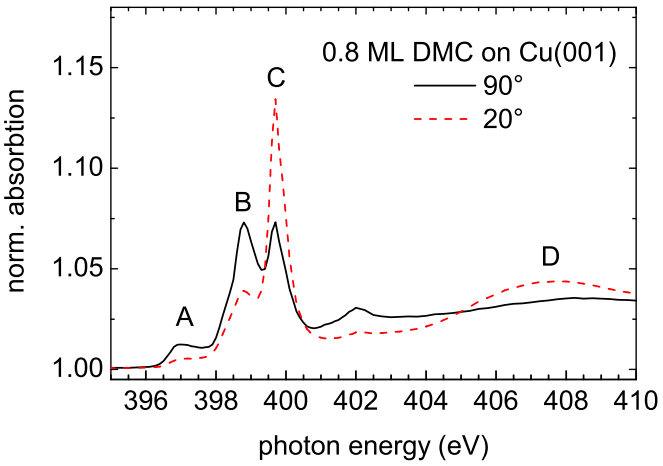

Figure 4.42: *N K-shell NEXAFS measured for 0.8 ML DMC evaporated on Cu(001) at room temperature. The continuous (black) and dotted (red) lines correspond to the spectra acquired for* 90° *normal and* 20° *grazing X-ray incidence, respectively.*

Fig. 4.42. Evident differences with respect to the spectra of 0.4 ML DMC sample (Fig. 4.31) on Cu(001) appear as a new π^* resonance peak at 397 eV labeled as A, and a shift of the σ-shape resonance at 407.4 eV (feature D) to higher energies. Most strikingly, the angle dependence of the entire spectrum is reversed. The π^* resonance at 399.7 eV (C), as well as the σ-shape resonance, are now more pronounced at 20° grazing incidence, while the features at around 398.6 eV (B) are more intense in the spectrum of 90° normal incidence. This strong angular dependence indicates a highly ordered molecular film.

The angle dependence of peaks B and C can be used to determine the orientation as for the case of 0.4 ML DMC on Cu(001) in Sec. 4.3.2.6. To do so, the signal of the low-coverage DMC (*cf.* Fig. 4.31) has to be subtracted first in order to obtain the pure spectrum of the additional species. Here we assume that the 0.4 ML spectrum represents the hole amount of low-coverage molecule. This is resonable regarding the grazing-incidence spectra of low- and high-coverage species in the upper panel of Fig. 4.43. There the resonance at 398.7 eV in the spectrum of the 0.4 ML sample fits perfectly into the one of 0.8 ML. This indicates that this peak originats only from the low-coverage species, taking into account that the low-coverage species is not influenced by the higher coverages (*cf.* Sec.4.3.2.3). Thus, we can substract the spectra of 0.4 ML from those of the saturated coverage. The difference spectra are given in Fig. 4.43, while the corresponding angles are summarized in Tab. 4.3. The data imply that the benzonitrile moiety of the high-coverage species stands almost perpendicular on the surface. Hence two scenarios could be considered. One possibility is that the molecule binds via the lone-pair electrons of one of the cyano nitrogens coordinatively while the molecular plane orients perpendicularly to the surface. A second possible scenario is that the molecules are bond

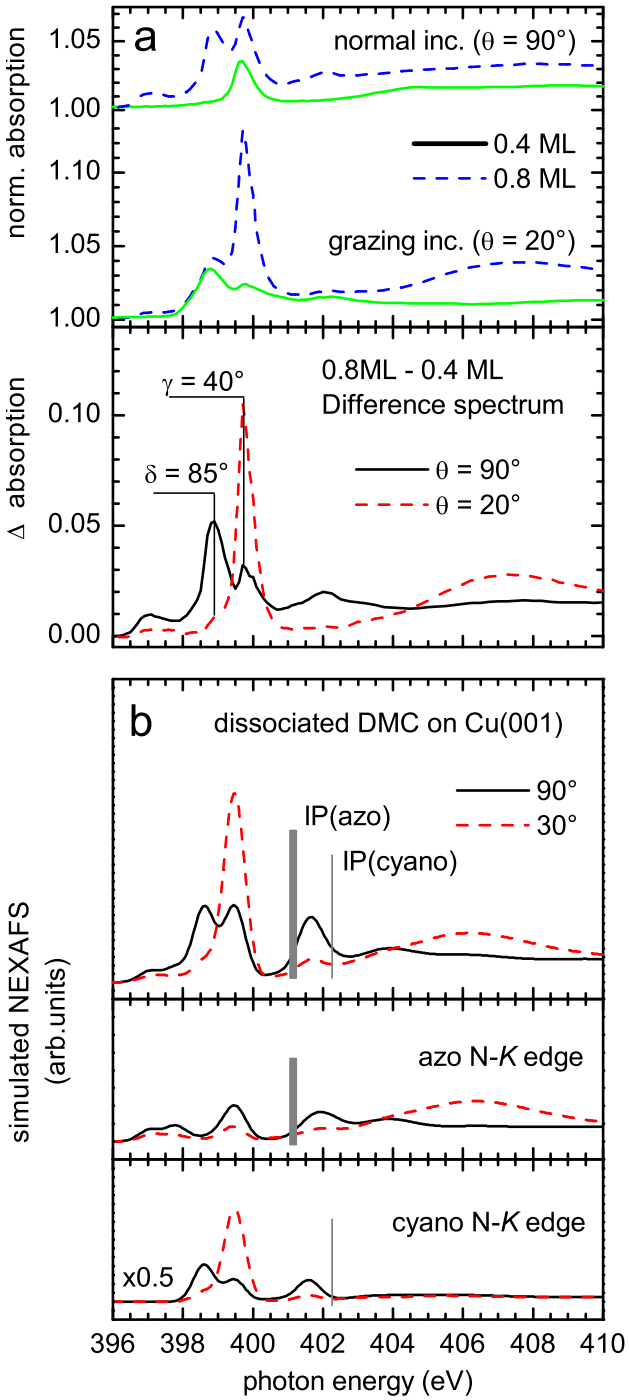

Figure 4.43: *(a) The upper panel shows the comparision of 0.4 (green) and 0.8 ML (blue) DMC on Cu(001) for* 90° *normal and* 20° *grazing X-ray incidence, separately. In the lower panel the difference spectra of 0.8 and 0.4 ML are given for normal (black) and grazing (red) X-ray incidence. (b) Simulated NEXAFS spectra of dissociated azobenzene on a Cu(001) surface (cf. Fig. 4.44). Gray bars mark the corresponding ionization barriers. The two lower panels in part (b) show the angle-dependent absorption spectra of the different excitation centers. Continuous lines correspond to spectra acquired or simulated for* 90° *normal X-ray incidence while dotted lines correspond to the spectra measured under* 30° *grazing and simulated for* 30° *grazing X-ray incidence.*

	δ	γ	θ	ω
experiment	85°	40°	15°	45°
theory	90°	30°	0°	*arbitrary*

Table 4.3: *Angles deduced from angle-dependent measurements of 0.8 ML DMC on Cu(001) (experiment) and from DFT-based geometry optimization of DMC dissociated at the azo bridge on a Cu_{68} cluster (theory).*

with their azo bridge and the benzonitrile moieties are tilted perpendicular to the surface.

For the 0.4 ML DMC on Cu(001), peak C in Fig. 4.42 at 399.7 eV was assigned to the in-plane cyano π^* orbital. This feature is found at the same energy position in the spectrum of 0.8 ML. Thus we can assume the cyano group to be rather unaffected at high coverages by any direct interaction with the surface. Furthermore the azo bond should not be influenced by this cyano–surface interaction, but the shift of the σ-shape resonance in energy from 408.5 eV for the physisorbed phase to 407.4 eV (peak D in Fig. 4.42) does not agree with this fact. We can thus exclude the first scenario of a coordinative cyano N–Cu bond scenario. The present data rather suggest an additional chemisorption state where the azo centers form bonds to the surface in a different way than in the low-cowerage species.

Considering the sp^2 character of the σ bond backbone of the azo center, the angle between the two azo–phenyl bonds can vary between 60° and 180°, by a rotation of the two azobenzene halves around the N=N bond axis without changing the overlap of the two nitrogen sp^2 orbitals. Assuming the azo bond axis in the surface plane, the tilt angle θ (see inset in Fig. 4.44) can vary between 30° and 90° without changing the binding energy of the azo σ bond. Further bending of the benzonitrile moieties toward the surface normal will reduce the overlap of the two nitrogen sp^2 orbitals, weakening the N=N double bond, and may ultimately lead to dissociation of the azo center. In order to substantiate this issue, we performed DFT calculations of a fraction of the dissociated DMC on Cu(001), as presented in Fig. 4.44.

From the geometry optimization, we find that the dissociation product adsorbs via the azo nitrogen in a hollow Cu(001) site perpendicular to the surface. The very good agreement of the simulated NEXAFS spectra, shown in Fig. 4.43(b), with the experimental data in Fig. 4.43(a) supports the suggested dissociation process. The low-energy π^* resonance at 398.7 eV corresponds to an additional N–Cu(001) bond oriented in the surface plane. The angle

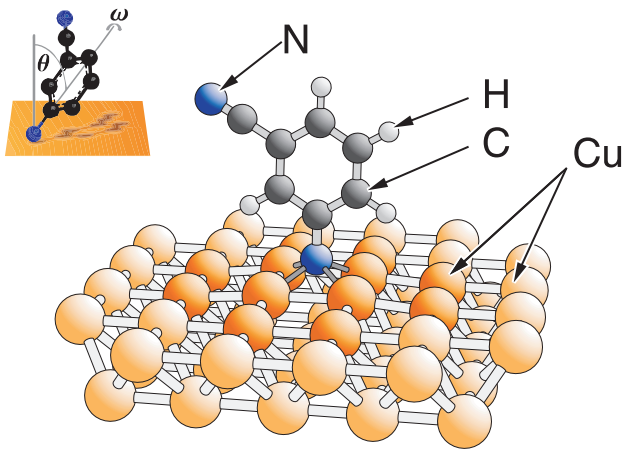

Figure 4.44: *Relaxed geometric structure of a single dissociated DMC azobenzene subunit on top of a Cu_{57} cluster, resulting from DFT geometry optimization. Darker and brighter substrate atoms were free and fixed during the optimization, respectively. In the inset the two angles θ and ω are defined to describe uniquely the orientation of the benzonitrile moiety with respect to the surface normal.*

dependence of the σ-shape resonance at 406.2 eV proves the absence of an azo σ bond lying in the surface plane. The only slight discrepancy between the experimental and simulated data appears in the angle dependence of the resonance at 399.7 eV. From the geometry optimization the orientation of the benzonitrile moiety can be determined, where $\theta = 0°$ with ω arbitrary. The slightly different orientation found in experiment and theory can be explained by the influence of intermolecular interactions which are not considered in the DFT calculation.

The adsorption site of the surface-binding nitrogen atom resmbles the one of strongly bond radical atomic nitrogen found on Cu(001) [88–90]. Furthermore, the calculated value of the adsorbate–substrate binding energy of 4.18 eV is in the range of the one of the DMC azo bridge (6.17 eV, *cf.* Sec. 4.3.2.4) and five times higher than the one of the low-coverage species (0.77 eV). The tilt of the phenyl rings provokes the cleavage of the N–N sigma bonds due to the strong coupeling to the aromatic π system that was discussed for the low-coverage adsorption mechanism (*cf.* Sec. 4.3.2.5). This is accompanied by the increase of interaction of the lone-pair electrons with the surface, as it was also reported for the stabilized cis-DMC isomer on Cu(001) in Ref. [15], which might reduce the activation barrier for the dissiciation process.

4.4 Discussion

In this chapter, the adsorption of CMA and DMC azobenzene molecules on metallic surfaces was studied by means of XPS and angle dependent NEXAFS measurements, comparing the results to DFT simulations. Au(111) and

Cu(001) are used as substrates with different reactivities. In the case of Au(111) at room temperature, 1 ML DMC is physisorbed lying flat on the surface in the *trans* conformation with an electronic structure similar to that calculated for the free molecule. In contrast, on Cu(001) a mixture of physisorbed and chemisorbed species appears already at low substrate temperatures of 150 K. During annealing the sample to room temperature, almost all physisorbed molecules evolve to the chemisorbed state above 250 K. The chemisorbed DMC species is characterized by the substitution of the central azo π bond with covalent bonds to the Cu(001) substrate. As a result, the benzonitrile moieties are tilted out of the surface plane. The influence of the molecule–substrate and intermolecular interactions was studied separately by comparing experimental NEXAFS data with simulated results from DFT calculations. We conclude that the chemisorbed DMC molecules exhibit a strongly distorted geometry with an increased bond length of the azo N=N bond due to the presence of the Cu(001) surface. The rehybridization of the HOMO system was found to cause the bent structure for this low-coverage species together with the repulsive forces between the phenyl rings and the substrate.

The bonding adsorbate-substrate interaction provokes a partial emptying and filling of the HOMO and LUMO, respectively. This is comparable with a optical excitation into the S_1 and S_2 states in which both *trans* and *cis* configurations are destabilized (*cf.* Sec. 4.1 and Fig. 4.5 therein). Hence, the bistable character that originates from the stabilization of the central N=N double bond is (at least partially) superseded by another bistability caused by the antagonistic interplay of atomic N $2p$ – Cu σ bonds formation and the interaction of the lone-pair electrons with the surface.

By increasing the coverage to 0.8 ML DMC on Cu(001), the intermolecular interactions lead to the dissociation of the additional azobenzene molecules at the azo center, so that the benzonitrile moieties are almost perpendicular to the surface plane.

Chapter 5

Ring-opening reaction of spiropyran

A class of organic photo switches is given by compounds for which the photo isomerization includes a reversible bond-cleavage/-formation process, or in particular for aromatic structures a ring-opening/-closing reaction. In contrast to purely conformational switches this type of izomerization causes a sizable modification of the corresponding chemical configuration which might even lead to the formation of radicals. Hence, beside the features that are known for pure conformational switches the bond-cleavage reaction opens a further dimension of light switching applications based on the control of the photoswitch's reactivity.

1',3',3'-trimethyl-6-nitro-spiro[chromene-2,2'-indole](nitro-BIPS) in particular undergoes such a photochromic process as shown in Fig. 5.1. The closed-ring *spiropyran* (**SP**) conformer on the left-hand side consists of a indoline and a benzopyran moiety. The two subunits are linked via a central sp^3 hybridized carbon atom such that their main symmetry planes[1] are orthogonal. In this non-planar geometry the aromatic π orbital systems of the two subunits have different symmetries and can thus only mix weakly by space-through interactions [91, 92]. Consequently with NEXAFS the LUMOs of the different subunits can be probed separately similar to the case of meta-substituted azobenzene (*cf.* Sec. 4.2).

After cleaving the bond between the pyran oxygen and the central carbon atom the molecule is free to unfold into the planar structure of *merocyanine* (**MC**) as shown on the right-hand side in Fig. 5.1. Here, the hy-

[1]Here, the main symmetry planes for indoline and benzopyran are given by the planes of the corresponding aromatic ring systems.

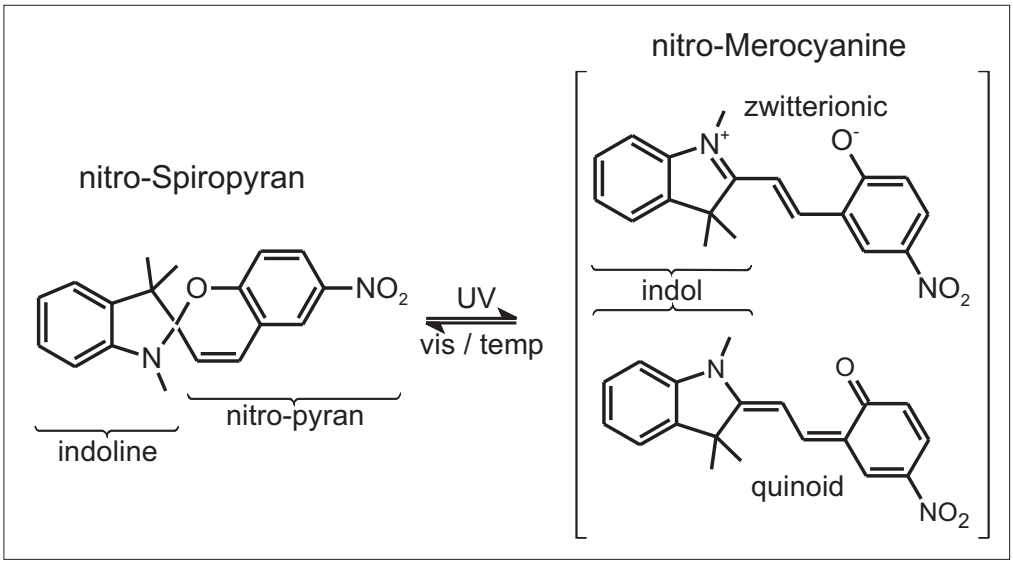

Figure 5.1: *Structure of the two most stable photoisomers of nitro-BIPS ($C_{20}N_2O_3H_{18}$).*

bridization of the central carbon atom has changed from sp^3 to sp^2, and the unhybridized atomic p orbital can couple the neighboring molecular π-orbital systems. This gives rise to a delocalized molecular orbital system that covers the whole molecule.

The resulting extended bond conjugation between the indol nitrogen and the ketonic oxygen leads further to two different possible bond configurations in the MC isomer labeled as quinoid and zwitterionic in Fig. 5.1. The two forms are close in energy. This provokes a mesomeric behavior which leads to hybrid structures with contributions of the zwitterionic and the quinoid form (*cf.* Sec. 5.1). Depending on possible additional substituents and also on the environment either the former or the latter dominates. In a polar solution, *e.g.*, the zwitterionic form is supposed to be stronger due to a higher gain of solvation energy, whereas the quinoid might be better embedded in a non-polar solvent [93, 94].

Noticeable from the zwitterionic form is the reactivity that is exclusively given for the MC isomer. It is, *e.g.*, known that the MC form offers protons to be accepted at the negatively charged ketonic oxygen, while the SP form is rather inert against this reaction (*cf.* Fig 5.2). A photoinduced ring-opening can thus lead to a change from acidic to a basic ambience of the molecular switch. It was further shown that in the ring-closing back reaction protons will be released again. A polyaniline chain that was embedded in such a

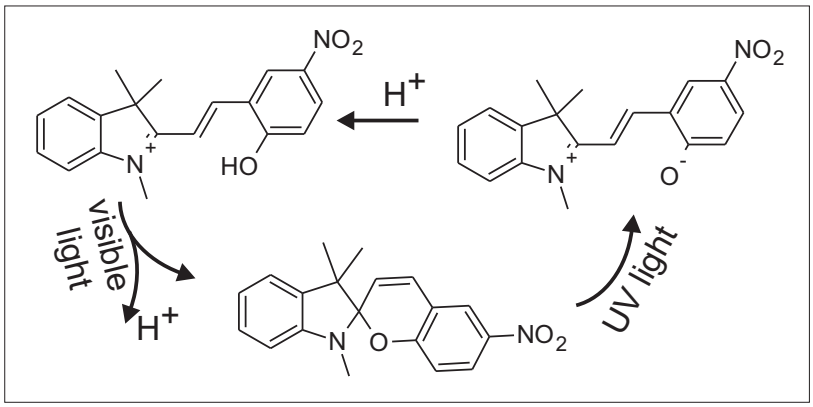

Figure 5.2: *Photo-controlled proton acceptance/donation of nitro-BIPS, adopted from [95].*

photo-controllable chemical milieu could be switched reversibly from low to high conductivity [95]. It has been further shown that the ketonic oxygen also accepts metallic ions as coordinative-bond partners. In this case same reversible photon-triggered attachment/detachment was observed, and the MC was even stabilized against thermal and optical back reactions [11, 96]. The interplay of chemically controlled photoreactivity and photocontrolled chemical reactivity has opened a new branch of information technology research that is named chemionics [97, 98].

In the last chapter it was shown that for azobenzene on Cu(001) the bond formation to the surface leads to a reconfiguration of the electronic system of the molecule that is responsible for the switching functionality. The resulting elimination of the switching ability might not appear in the case that BIPS adsorbs with an coordinative bond to the metallic substrate. In fact, possible coordinative bonds of MC compounds with metallic surfaces via the ketonic oxygen might rather lead to a support of the switching mechanism.

5.1 Isomerization process

To discuss the isomerization process, the reaction paths can be subdivided into two steps. Taking the SP isomer as a starting point, the forward (SP→MC) reaction starts with the ring-opening process. This is followed by the relaxation of the molecular structure along the resulting alkene chain that connects the indol moiety with the ketonic nitrobenzene. Vice versa, for the backward (MC→SP) reaction the refolding of the alkene bridge has to precede the ring-closing reaction [99]. The single steps have been identified by optical

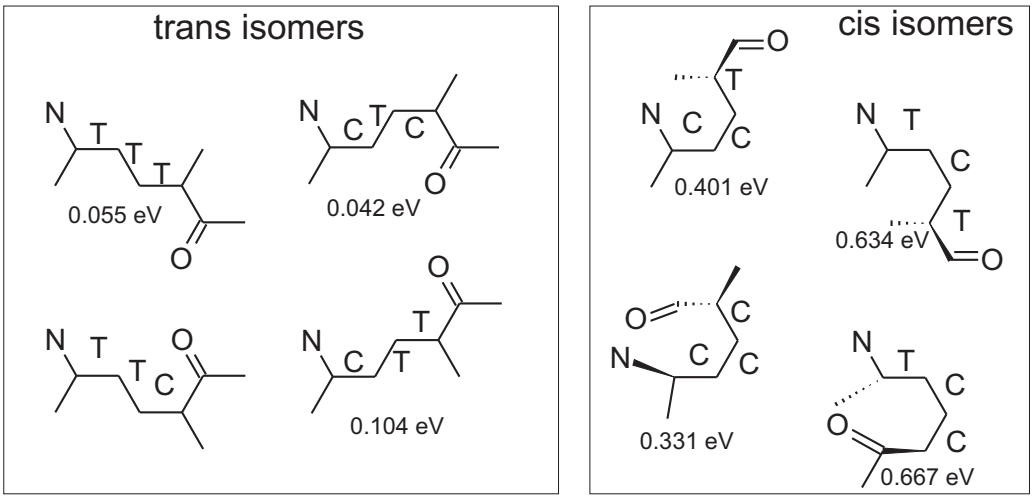

Figure 5.3: *Sketch of the eight possible conformers of merocyanine. For simplicity only the central part of the molecule is drawn in the chemical structure. The energy values correspond to the total energies of the DFT-relaxed geometries. The labels T (trans) and C (cis) indicate the conformations of the corresponding alkene-bride segments.*

and time-resolved Raman spectroscopy [100–102]. To understand the corresponding reaction dynamics, the activation barriers of all conformational and ring-opening/ring-closing processes have to be regarded. On one hand the ring-opening reaction is a rather straight process in which the bond cleavage causes the rehybridization of the central carbon atom. As for all chemical reactions, the reaction barrier of this process strongly depends on the distance between the two contributing atoms.

On the other hand, the conformational change at the alkene bridge can follow different reaction paths. Each of the three segments of the alkene bridge can be rotated around the bond axis of its neighbors into one of two possible, stable orientations. Consequently, there are eight different conformations possible as shown in Fig. 5.3. Comparing the structures of the resulting isomers, the biggest distance between indol and ketonic nitrobenzene is given for the trans-MC molecules (left panel in Fig. 5.3). In this case, the interaction between the two aromatic subsystems is relatively weak. This leads to a planar configuration for all four trans-MC compounds which is confirmed by DFT geometry optimization. The corresponding calculated ground state energies are given with respect to the one of the TTC isomer (left bottom), which is the most stable compound. The values are in good agreement with those presented by Leszczynski *et al.* [99] for another nitro-BIPS derivative where the methyl

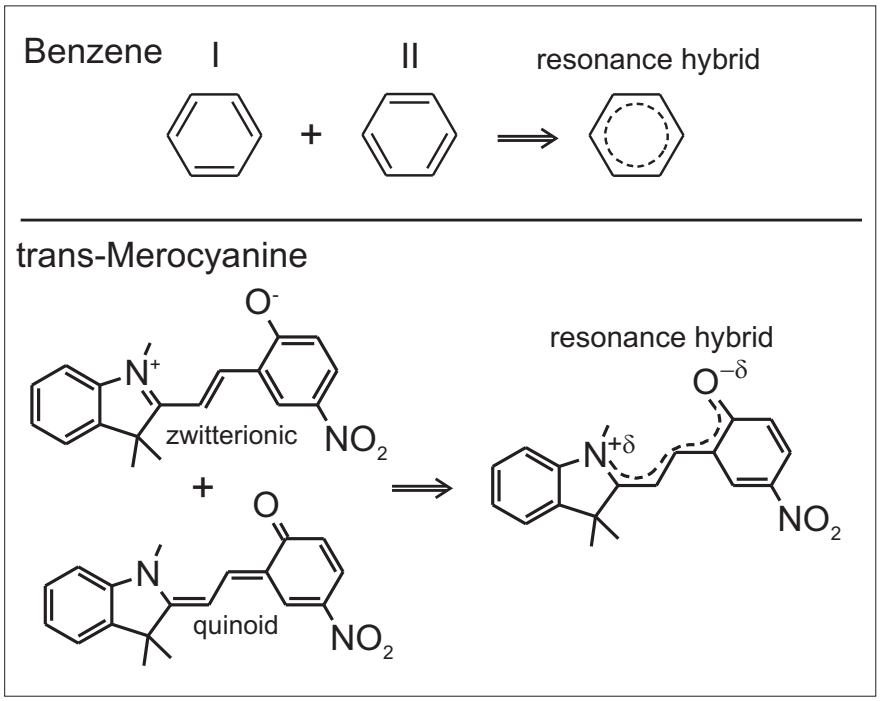

Figure 5.4: *Mesomerism of benzene (upper panel) and merocyanine (lower panel).*

substituents at the indole ring had been replaced by hydrogen (nitro-BIPS2).

In the *cis* form the indol and the ketonic nitrobenzene interact much stronger with each other due to their reduced distance. This leads to steric hindrance and results in a nonplanar ground state geometry in analogy to the case of *cis* azobenzene in chapter 4.1. The resulting ground state energies are hence much higher than those of the *trans* species. The strong steric interaction between the two aromatic subsystems is further influenced by their substituents, and the resulting total energies are thus different to the ones of nitro-BIPS2. Due to their lower ground state energy the *trans* isomers are the end products of the photoisomerization in gas phase and solution[103], while the *cis* conformers are intermediates on the SP→MC and MC→SP reaction paths. This is reasonable regarding the transition from the 3D SP structure two the 2D *trans* MC conformation and vice versa.

Not only the different ground state energies are influenced by the present substitution groups, but also the isomerization process itself. It was shown in different studies that the activation barrier for thermal back-(MC→SP)-reaction is strongly increased by appended electron-donor and -acceptor groups as well as by a polar environment, while the SP→MC isomerization is not

evidently affected [93, 94, 103, 104].

The dependence of the trans-cis activation barrier that is found for the MC form can be explained by going back to the mesomeric character of this isomer introduced in the last section (*cf.* Fig. 5.1). For this, one might start with the easier picture of the mesomerism of benzene. Here, the alternating single-bond/double-bond arrangement can exist in two different configurations labeled as I and II in the upper panel of Fig 5.4. Assuming that a single molecule could adopt only one of these structures at the same time, each pair of π bond electrons will be localized around one pair of double-bonded carbon atoms. The bond lengths between the neighboring carbon atoms would than alternate corresponding to the single-/double-bond pattern. However, the two mesomeric states of benzene are energetically equal and can thus coexist equally in a quantum chemical hybrid state (resonance hybrid). This results in a six-fold symmetry of π bond system along the ring structure. Due to the higher delocalization of the valence electrons in the resonance hybrid, the ground state energy of the benzene molecule is lowered by the so called resonance energy.

The two resonating MC species are shown in the lower panel of Fig. 5.4. Similar to benzene, an opposite distribution of double bonds is given for the quinoid and the zwitterionic species between the indol nitrogen and the ketonic oxygen. An optimal mixing and thus a maximum gain of stabilizing resonance energy is given if both bond configurations are energetically equal (like in the case of benzene). The strength of the mesomerism and its stabilizing effect on the alkene bridge thus depends on the total-energy position of the zwitterionic isomer. For unsubstituted BIPS the latter can be lowered toward the total energy of the quinoid form by both, appended electron-donor groups at the indol and acceptor groups at the ketonic benzene as well as by the polarity of the environment. The resulting increase of bond strength at the central alkyl bridge causes an higher activation barrier for the trans-cis rotation. The gained contribution of the resonance energies are in the order of magnitude of the activation barrier of the izomerisation process. For the MC isomer of nitro-BIPS, the activation barrier of the trans→cis transformation is higher than the one of the ring-opening reaction and thus the rate-determining process.

5.2 Multilayer

In the gas phase and in solution, the isomerization of nitro-BIPS is well understood, as discussed in the last section. However, the addressability of molecular units, e.g., in information storage of computational devices usually demands a

solid phase. There is a variety of different strategies to implement switchable molecules into a solid matrix, like, e.g., into amorphous material like silica gel [105] or glasses, into polymers [106] or in single and clathrate crystals. In general, the question arises whether the original photo functionality is preserved in a solid ambience. Since the intermolecular bond mechanisms in organic crystals are mainly of non-covalent nature, the chemical properties of the embedded compounds do usually not change. Indeed a bigger problem arises from the decreased conformational flexibility. Since most of the photoisomerization processes involve a conformational change, there has to be enough elbowroom to perform the entire transformation. A key task is thus the development of rather slackly packed organic arrangements. There are various examples for BIPS derivatives in solid matrices, but they were studied only recently in single crystal confinements [107, 108].

An easy way to produce an organic single crystal of switchable molecules is to crystallize them from solution or by vapor deposition on a substrate. A disadvantage is that in such ensembles the packing density is usually quite high and the molecules tend to be frozen in a certain conformational state. For spiropyran and spirooxazine derivatives it has been shown that the C–O bond cleavage takes place in several single-crystalline structures [109, 110], but usually the conformational change is sterically hindered. However, recently Karcher *et al.* presented a work in which nitro-BIPS deposited as an organic film of 5 - 40 nm thickness on a MgO substrate could be switched reversibly by UV and visible light [111]. This proven system was taken here as a starting point for spectroscopical characterization. Since the interaction of the molecules with both, the insulating MgO as well as the relatively inert Au(111) is expected to be weak, the effect on the crystalline growth mode was assumed to be negligible. Regarding this, all the present studies are performed on a Au(111) metallic single crystal where X-ray photoemission induced electric charging at the surface can be compensated through the substrate, and the experimental efford for XPS and TEY NEXAFS is thus moderate.

5.2.1 Growth mode

The molecules have been evaporated from a Knudsen cell at ca. 100°C. Similar to DMC and CMA, nitro-BIPS adsorbs on Au(111) at 300 K with a noticeable adsorption rate only up to a certain coverage, which will be refered here as to a saturated monolayer. To evaporate films thicker then the saturated monolayer, the substrate was cooled to 150 K. The resulting O K-shell NEXAFS spectra of nitro-BIPS multilayers of different thickness and of a saturated monolayer

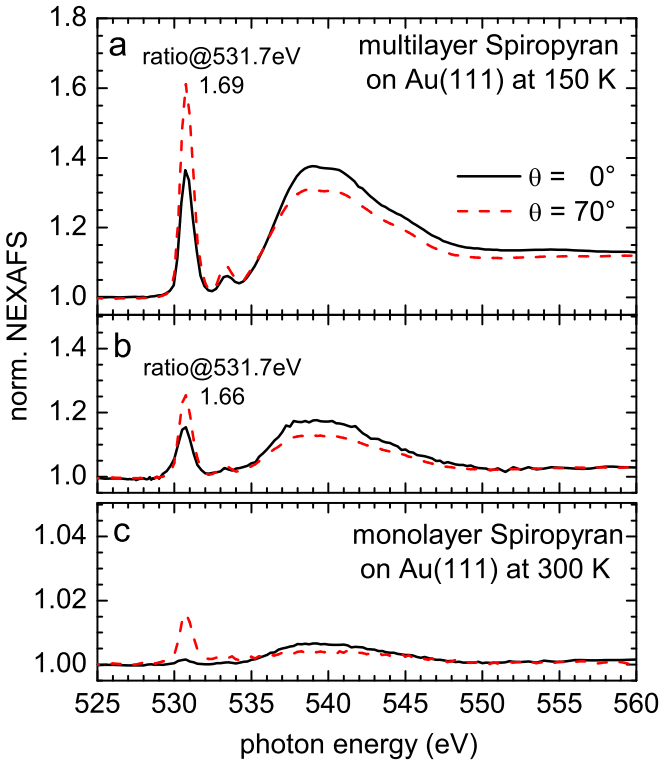

Figure 5.5: *Thickness-dependent O K-shell NEXAFS of (a,b) multilayers of different thicknesses evaporated on Au(111) at 150 K, (c) saturated monolayer evaporated on Au(111) at 300 K.*

are given in Fig. 5.5a, b, and c, respectively. For the monolayer, the adsorbate contributes here with 1.5% to the spectrum of $\vartheta = 20°$ (grazing) X-ray incidence at 530.8 eV. The corresponding intensity of the multilayer NEXAFS is more than one order of magnitued higher.

For the saturated monolayer the resonance at 530.8 eV appears almost only in 20° normal X-ray incidence. This evidences that the corresponding final-state π^* orbital species is perpendicular to the metalic surface for all adsorbed molecules. The angle dependence of the resonance at around 530.8 eV, which appears in all three spectra, is obviously decreased going from the film of saturated coverage to thicker coverages, but there is still at least a certain degree of order. On the other hand, in the NEXAFS of the multilayers of different thicknesses the same angle dependence is visible wich a constant intensity ratio between normal and grazing incidence of 1.7 at 530.8 eV (*cf.* Fig. 5.5(a) and (b)). This implies that the molecular order is preserved toward higher coverages. Obviously there is a molecular crystal formed.

For the determination of the multilayer film thickness one can use Eq. 2.12. The electrons' minimal mean free path is assumed to be $L = 7$ Å [112] and the thickness of 1 monolayer to be about d = 0.7 Å, which is the average

covalent radius of carbon and nitrogen. Assuming that the saturated film has a thickness of around one monolayer I_{a0}/I_{s0} corresponds to the 1.5% measured at 530.8 eV in grazing incidence. The corresponding values for panel a and b have to be extracted from both normal ($\vartheta = 0°$) and grazing incidence spectra. Here the normal incidence absorption counts double for linearly polarized light if we assume the molecular orbitals either aligned in a three-fold symmetry like the Au(111) surface or randomly oriented in the surface plane (*cf.* Sec. 2.2.2). Thus the relative adsorbate intensities of the multilayer films for panel a and b are 130% and 65%, and the resulting number of monolayers 35 and 20, respectively.

5.2.2 Electronic properties of spiropyran

The thickness-dependent angle-resolved N K-shell NEXAFS spectra of nitro-BIPS are given in Fig 5.6. They coincide with what was discussed in the last section. The same angle dependence as for the O K-shell NEXAFS is found for the spectra of the two multilayer thicknesses in panel a and b. However, for the 35 ML film it becomes obvious that the different angle dependences of a small resonanceat 401.8 eV and one stronger resonance at 403.6 eV prove the existence of final state orbitals of different orientations. There are several indications that the molecular crystal consists of SP molecules. Assuming that the organic film consists exclusively of *trans* MC molecules, the same angle dependence f should be observed for all π^* resonances, since the planar *trans* MC structure exhibits only one conjugated π system. Furthermore, in gas phase SP is the more stable isomer even regarding the evaporation temperature of 100°C and a ring-opening reaction during adsorption is most unlikely. Finally SP was also found to be adsorbed on the MgO substrate as reported in Ref. [111].

To identify the present molecular state, a DFT-based NEXAFS simulation was carried out for an isolated Spiropyran molecule. The geometry was optimized strarting with the coordinates given in Ref. [113] where the resulting bondlengths do not differ more than 1% from literature. The result is given in Fig. 5.6(d). The good agreement between calculated and measured data supports the initial guess that only the SP isomer is forming the crystalline film. The partial absorption of the two different N 1s excitation centers are given as the lower graphs of panel d together with the plots of the transition state orbitals corresponding to the two most prominent NEXAFS resonances. The strong resonance at 403.3 eV results from the nitro N 1s transition into the LUMO, which is consistent with what was found for

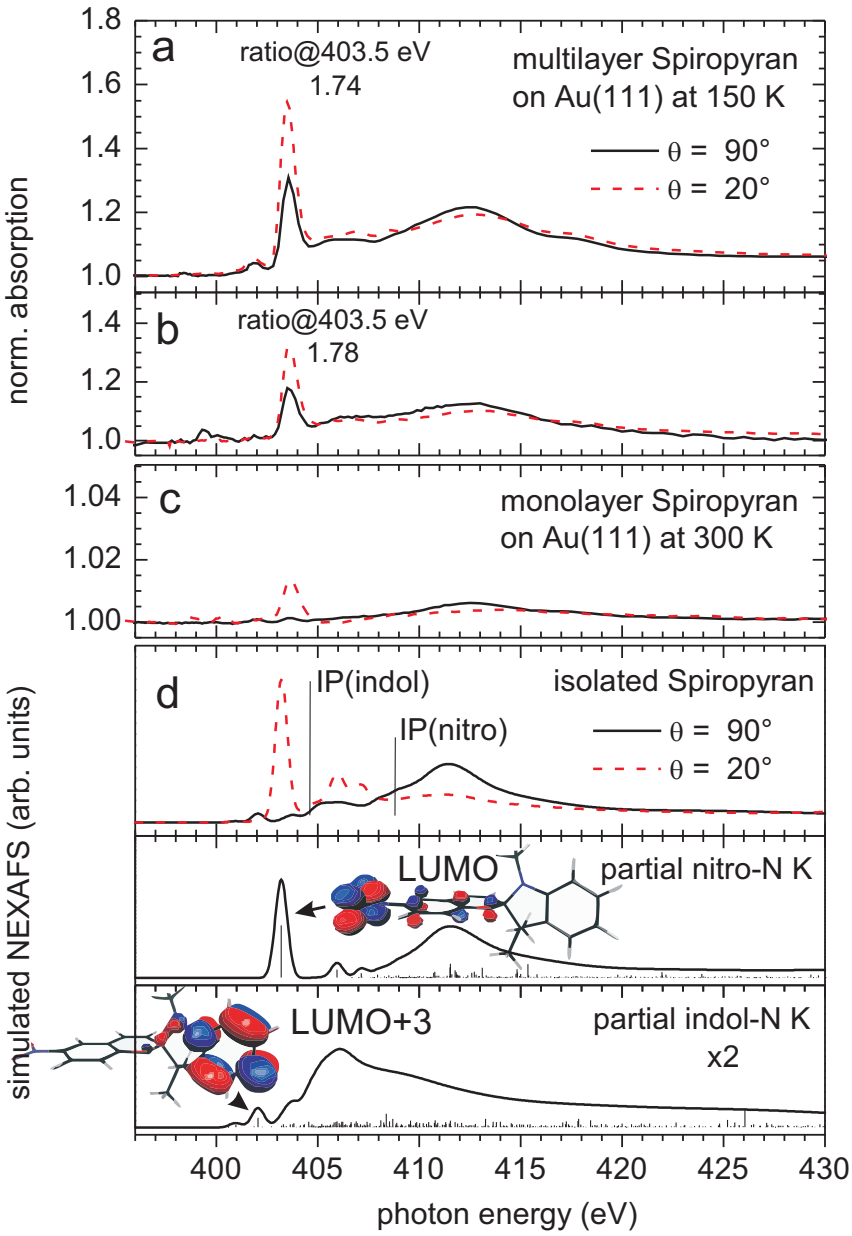

Figure 5.6: *Thickness-dependent angle resolved N K-shell NEXAFS of (a,b) multilayers of different thicknesses evaporated on Au(111) at 150 K, (c) saturated monolayer evaporated on Au(111) at 300 K. (d) Simulated angle-dependent N K-shell NEXFAS of an isolated spiropyran molecule for which the angle θ is defined between the polarization of light and the benzopyran plane. The two lower graphs of panel d show the partial absorption of the indoline and the nitro N 1s excitation centers, respectively and include also the transition orbital plots for the two energetically lowest prominent resonances.*

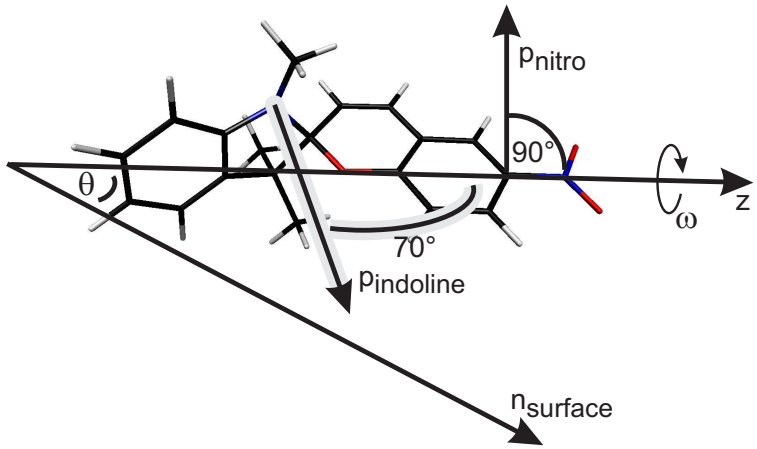

Figure 5.7: *Orientation-defining angles for the determination of the alignment of the SP molecules in the organic crystal.*

nitrobenzene [114]. The weaker feature at 401.8 eV belongs to the indol N 1*s* transition into the LUMO+3 and appears at lower energies than the one of the nitro N 1*s* →LUMO transition because this binding energy of the indol excitation center is 4 eV lower. Here the entire partial indol spectrum spectrum is shifted to lower photon energies.

The observed orientation in the π^* resonances in N and O K-shell edges opens the question how the molecules are oriented in the crystalline phase. Indeed the peaks at 401.8 and 403.3 eV in the N K edge spectra are related to the two orthogonal π systems and can hence be used to get an idea of the polar orientation of the two spiro-linked moieties with respect to the surface normal. The resulting orbital orientations are given with respect to the surface normal in Tab. 5.1, assuming that all molecules are oriented in the same way.

Similar to the angle analysis of DMC azobenzene in the last chapter (*cf.* Sec. 4.3.2.6), one might give now a more detailed picture of the orientation in the thin film using the fixed relative orientation of the two decoupled π orbital systems of indoline and nitrobenzene. Analog to the azo phenyl bond axis in

	$\Theta_{nitro}(NKedge)$	Θ_{indol}	$\Theta_{nitro}(OKedge)$
Multilayer (35 ML)	46°	49°	47°
Multilayer (20 ML)	46°	53°	47°

Table 5.1: *Calculated angle for the orientation of SP in the organic multilayer.*

the angle analysis for DMC, the nitro NO_2-phenyl bond is now defined as z axis. The nitro-LUMO vector is perpendicular to the z axis and defined in the $y-z$ plane. The orbital vector of the indoline LUMO+3 is given by the following geometrical consideration based on the geometry-optimized molecular structure (*cf.* Fig. 5.7): The aromatic rings of indoline and nitrobenzene are perpendicular to each other. Thus the indoline orbital vector has to lie in the $x-z$ plane. The angle between the indoline plane and the nitro–phenyl bond vector is 20°. Since the indoline bond vector is perpendicular to the indoline ring, the angle between the indoline orbital vector and the z axis is 70°. The corresponding orbital vectors are thus given as follows:

$$\begin{aligned}\vec{\mathbf{p}}_{nitro}(\omega) =&(\cos(\varphi)\sin(\vartheta),\sin(\varphi)\sin(\vartheta),\sin(\vartheta))|_{(\vartheta=\frac{\pi}{2},\varphi=\omega+\frac{\pi}{2})}\\ =&(-\sin(\omega),\cos(\omega),0)\end{aligned} \tag{5.1}$$

$$\begin{aligned}\vec{\mathbf{p}}_{indole}(\omega) =&(\cos(\varphi)\sin(\vartheta),\sin(\varphi)\sin(\vartheta),\sin(\vartheta))|_{(\vartheta=\frac{7}{18}\pi,\varphi=\omega-\pi)}\\ =&(-\frac{1}{2}\cos(\omega),-\frac{1}{2}\sin(\omega),\frac{\sqrt{3}}{2})\end{aligned} \tag{5.2}$$

To specify the molecular orientation uniquely, two angles ϑ and ω define the orientation of the SP molecule with respect to the surface normal uniquely. The resulting angles for the multilayered SP are $\vartheta = 85°$ and $\omega = 45°$.

5.2.3 Switching properties

The photochromic behavior of the molecular multilayer was studied by illuminating the sample with the filtered light of a 1000 W Xe arc lamp. The set-up is shown in Fig. 5.8. The lamp is commercially available from LOT and has a light-emitting spot size of 1 mm x 3 mm. A collimator optics with a lens of 50 mm focal length integrated in the lamp housing forms a parallel bundle of rays. The parallel rays are focused by a 250 mm lens behind the mirror onto the sample resulting in a light spot of about 1 cm in diameter. Light of the desired wavelengths was in three steps filtered out of the white Xe arc spectrum that covers a range from 250 nm to above 1000 nm. Since a sizable spectral contribution is infrared the beam is passed through an IR absorbing water flow cell. In a second step either a cold or a visible light mirror reflects the spectral components below or above 400 nm, respectively, toward the sample. To refine a spectral region that corresponds more or less to the one of the molecular absorption band, additional absorption filters are included.

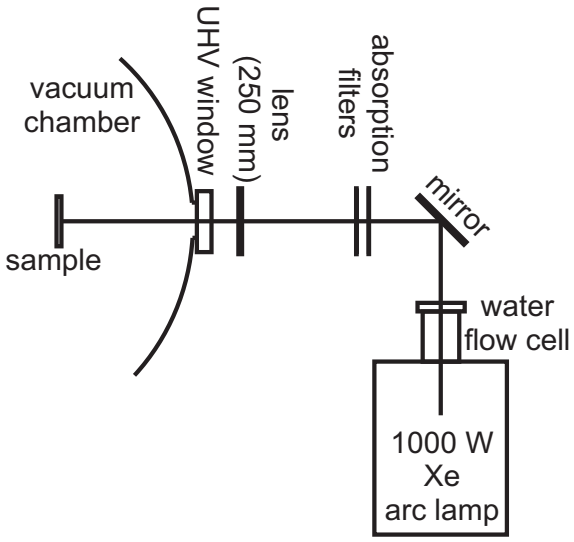

Figure 5.8: *Illumination set-up: Light from a 1000 W Xe arc lamp is reflected by a wavelength-selective mirror (either cold light (250-400 nm) of visible light (400 to 800 nm)) toward a 250 mm lens that focusses the beam on the sample. A water flow cell absorbs the IR contributions of the light beam. Additional absorption filters select the desired range of wavelengths.*

For the illumination of the SP multilayers with UV light, a UG11 absorption filter was used together with the cold light mirror. The estimated intensity at the sample was 200 mW/cm^2. Fig. 5.9(a) shows the N K-shell NEXAFS spectra of a SP multilayer before and after illumination for 15 min, taken under grazing X-ray incidence. Here the peak at 401.8 eV, which was assigned to the indol N 1s →LUMO+3 transition, vanishes almost completely. Instead a stronger resonance appears at 400.2 eV. Assuming that the SP→ MC transformation is induced by the UV light, the NEXAFS of an isolated TTC merocyanine molecule was simulated, shown in Fig. 5.9(b). Again the nitro N 1s →LUMO transition is the most prominent π^* resonance at 403.3 eV. The additional peak at 400.3 eV that was observed in the measured spectra, appears in the simulated spectra as related to the indoline N 1s →LUMO core hole excitation. This resonance is stronger in intensity than the one at 401.8 eV of the transition in the indol π system, since the non-hybridized atomic N p orbital now contributes more strongly to the conjugated MC π system, which results in a bigger overlap between the indoline N 1s core orbital and the LUMO. The higher contribution is consistent with the appearance of an additional fourth π bond at the indoline nitrogen in the chemical structure of the zwitterionic MC isomer (*cf.* Fig. 5.1).

The NEXAFS simulations of the seven other MC conformers (*cf.* Fig. 5.3) result in spectra without any evident difference neither in resonance intensities and energies nor in the calculated ionization potentials. Thus NEXAFS and XPS might not be suitable to determine the conformational state of the ring-opened form.

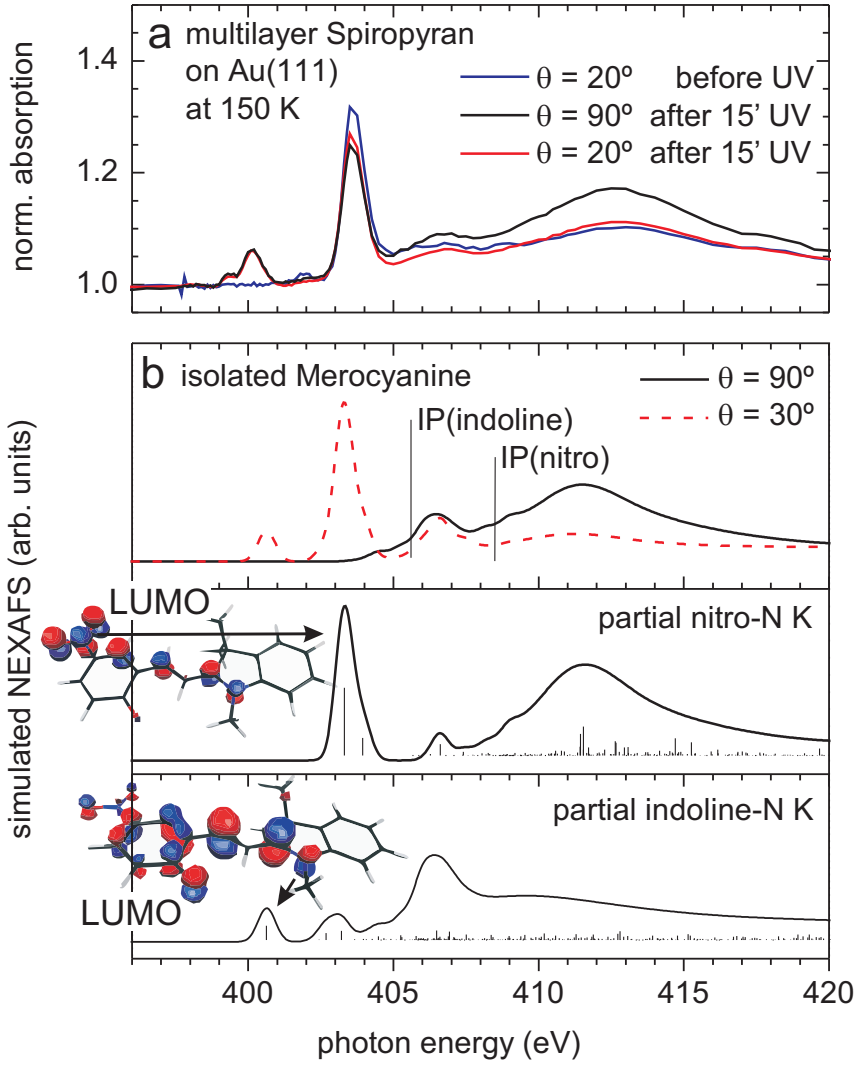

Figure 5.9: *Upper panel: N K-shell NEXAFS of a nitro-BIPS multilayer on Au(111) after 15 min UV radiation for* 90° *normal (black) and* 20° *grazing (red) X-ray incidence. For comparison the grazing spectrum of the sample before illumination is added as the blue curve. Lower panel: Simulated angle-dependend N K-shell NEXAFS of a isolated merocyanine molecule. Transition orbital plots are given for for the two energetically lowest prominent resonances from the indoline and the nitro N 1s excitation centers.*

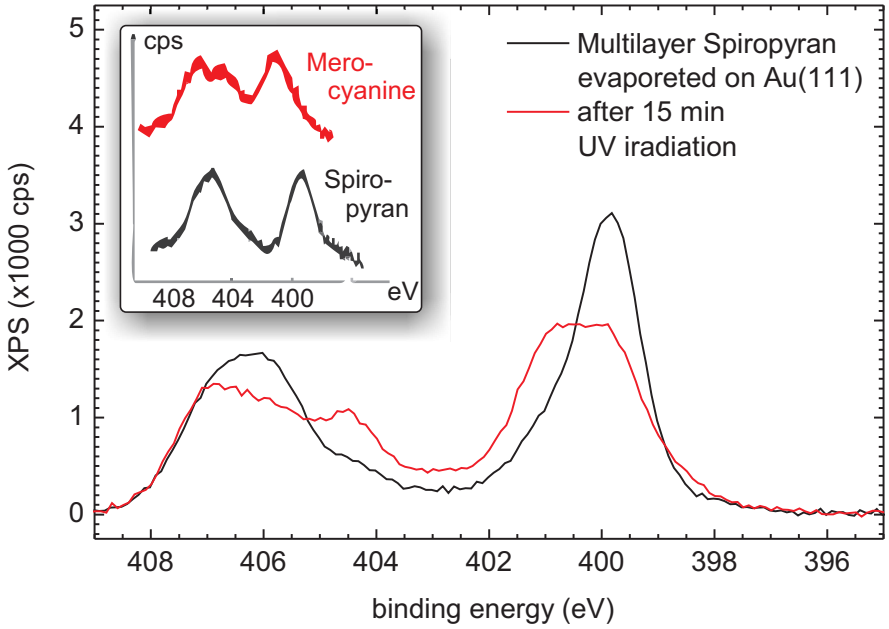

Figure 5.10: *N1s XPS of a monolayer spiropyran (a) adsorbed in a multilayer on a Au(111) surface at 150 K substrate temperature. (b) The same sample illuminated for 15 min with UV light. Inset data were taken from Ref. [115].*

The angle dependence of the π^* resonance at 403.3 eV is decreased after illumination (compare the upper panels of Fig. 5.6 and Fig. 5.9). This might be caused by a possible molecular reorientation in the crystal due to the conformational change after the ring-opening reaction. However, an increase of the angle dependence is observed in the entire σ resonance area, and attests a preserved degree of order. The reorientation in the crystalline structure thus seems to happen homogeneously in the whole film. Unfortunately, no reliable angle analysis can be performed here on the base of the σ regarding the possible overlap of the shape resonances with shake-up features (*cf.* Sec. 2.2.1).

The calculated energetic difference between the ionization potentials of indol and nitro N 1*s* core electrons is significantly smaller for SP than for MC, so that one can expect a strong change in the XPS signal between the two species, too. The XPS measured for a film of 25 ML of nitro-BIPS before and after 15 min UV illumination is given in Fig. 5.10. The spectrum of the sample before illumination shows two prominent peaks at 399.8 and 406.5 eV. The XPS of a similar nitro-BIPS derivative was measured by Delamar *et al.* [115] and is given as the black lower graph in the inset of Fig. 5.10. This

specturm is in very good agreement with the one of the unilluminated sample. The sharper peak at 399.8 eV is due to emission from the indoline nitrogen atom, while the broader peak at higher binding energy (406.5 eV) is assigned to N 1s core levels in the nitro moiety[2], which is consistent with the larger ionic character of nitro group [115, 116]. We have thus an additional confirmation that the evaporated species before illuumination is the SP form.

After illumination the spectral form has changed drastically. The intensity of the low-energy component at 399.8 eV decreases and shifts toward 400.5 eV. The high energy peak at 406.5 eV is also reduced in intensity while an additional feature appears at 404.5 eV. The N 1s XPS of a pure MC derivative is given as the red curve in the inset of Fig. 5.10. Compared to the corresponding SP spectrum (in the same inset), the low energy component transforms completely from the peak at 399.8 to 401.3 eV. This shift of the indoline N 1s peak to a higher binding energy indicates a decrease in the electronegativity of this atomic site after the ring opening. This is expected for the merocyanine zwitterion, where an additional π bond is created at the triply bonded nitrogen atom, and balanced with a negative charge at the carbonyl oxygen (see structure in Fig. 5.1). Further comparison of the SP and MC spectra in the inset of Fig. 5.10 reveals that the high-energy component splits up into two peaks at 404.5 and 407.0 eV. This double-peak structure in the N 1s photoemission from the nitro moiety is a characteristic feature in the spectra of the merocyanine. It has been attributed to the appearance of a prominent shake-up satellite involving a charge transfer between the electron donor and acceptor parts of the molecule [115, 117], and reflects the very high degree of conjugation between the two cycles.

From the observation of the measured N 1s XP spectrum that was take after 15 min UV illumination it becomes clear now that it contains contributions from both, the pure SP and MC spectra (in the inset of Fig. 5.10). The intensity of the low-energy component in our case only decreases about halve by the amount as before illumination. Conclusively, half of the SP molecules in the organic crystal have been switched to MC. Further illumination with UV light does not increase the amount of MC molecules.

Light of several wavelengths has been used to provoke a back switching from MC to SP at 150 K, however, without any success. The produced MC isomer was stable over at least 4 hours at this temperature and also going from 150 K to room temperature no change could be observed. At 330 K

[2]The broadening of the peak has been explained by a second component at higher energies in addition to the N1s(NO_2) resonance. The additional peak is a shake up resonance coming from intramolecular charge transfer [115]

the molecules of the multilayer have been fully desorbed except the monolayer that was directly adsorbed on the metallic substrate. Obviously the different preparations reported in [111] lead to different growth modes, such that the resulting different crystalline structure in our case prevents the back reaction. This might be caused either by the different substrates used or by the different evaporation temperatures. On the other hand the appearance of radiation damage is most unlikely regarding the good agreement of measured and calculated data.

5.3 Adsorption on Au(111)

As found in the last section, both isomers can be clearly identified by their N K-shell NEXAFS and N 1s XPS. The XPS of 1 ML of nitro-BIPS on Au(111) is given in Fig. 5.11 for an annealing sequence from 230 to 330 K acquired at 500 eV photon energy. Compared to the multilayer all spectra in Fig. 5.10 are shifted by 0.8 eV to lower binding energies for the directly adsorbed molecules. This is the same effect that was found and discussed for DMC on Au(111) (*cf.* Sec. 4.3.1.2 and Fig. 4.18 therein). The spectrum at 230 K shows two prominent peaks at 399.0 and 405.3 eV, the positions and line-widths of which closely resemble the N1s photoemission spectra that were obtained for the multilayer SP samples and presented in the previous section. Thus the data suggest that the molecules are adsorbed in their spiropyran form at low temperatures.

When the temperature of the sample is increased above 300 K, the indol N 1s peak undergoes a similar change in energy as caused by UV irradiation of the SP multilayer, where a new component at $E_b = 400.5$ eV arose, while the peak intensity at 399.0 eV was decreased. In Fig. 5.11 the low energy feature of indoline vanishes almost completely at 330 K. Conclusively, the SP form is converted almost completely to MC on the Au(111) surface at 330 K.

In addition to the N 1s spectra, O 1s XPS data were recorded to corroborate the thermally induced ring-opening reaction (Fig. 5.12). The spectrum at 230 K shows a peak centered around 532.2 eV binding energy and a shoulder at ≈ 534 eV. Upon warming the sample to 330 K, the main peak shifts to lower binding energies and becomes broader. The shift of the weight of the measured signal to lower binding energies is consistent with the negative charge on the pyran oxygen atom in the zwitterionic form of the merocyanine. Since the signals from the pyran and nitro oxygen atoms are close in binding energies, certain assumptions are necessary in order to decompose the peak into its components. For the peak decomposition shown in Fig. 5.12 the following assumptions have been made: The position of the peak resulting from the nitro

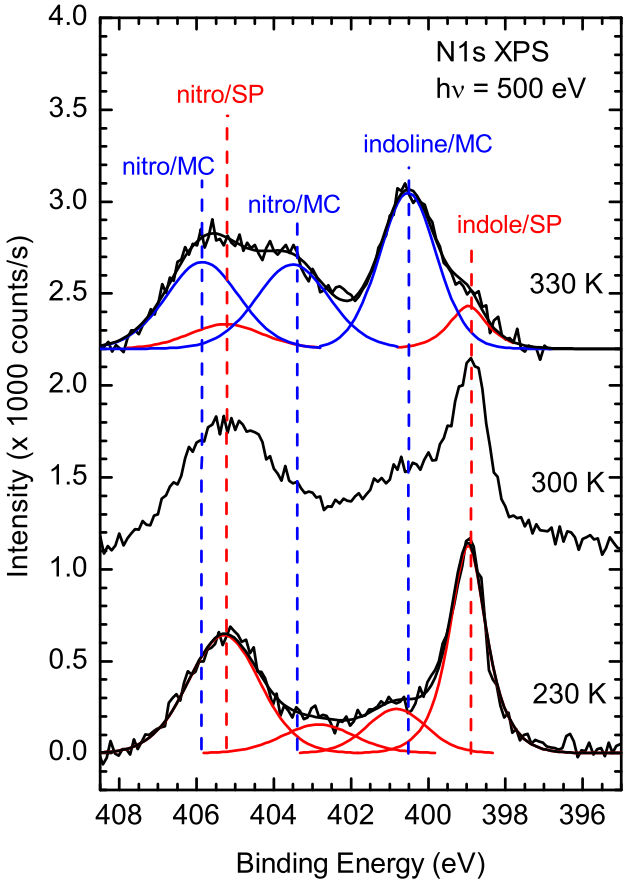

Figure 5.11: *X-ray photoelectron spectra of ∼ 1 ML nitro-BIPS on Au(111), taken during a heating sequence from 230 K to 330 K (overall energy resolution for XPS is 670 meV). From each spectrum a linear background was subtracted. The spectra are shifted vertically for clarity. Smaller components at 400.8 and 402.8 eV in the spectrum at 230 K (red lines) may be due to either a minute amount of the high-temperature phase already present at that temperature, for example at step edges or kinks, to shake-up processes during the emission of the indol N1s electron, or to partial cleavage of some of the molecules.[118].*

O 1*s* photoemission is kept fixed, as well as its width. The shoulder at higher binding energy, which we assign to the shake-up process linked to the emission from the nitro O 1*s* level,[118–121] is also kept fixed in position and width. The area ratio between the sum of these peaks and the third component, representing the emission from the pyran oxygen atom, was fixed at 2:1 acording to the amount of nitro (2 atoms) and keto (1 atom) oxygen in the nitro-BIPS molecule. Under these assumptions the shift of the peak is attributed solely to the pyran oxygen emission. The resulting binding energies are: For the nitro O 1*s* main peak 531.8 eV, the nitro shake-up 533.8 eV, the pyran O 1*s* at 230 K 532.5 eV, and from the pyran O 1*s* at 330 K 530.9 eV. Note that this decomposition is not unique and depends on the assumptions mentioned above; it is not intended to determine the individual binding energies but to emphasize the expected shift of the O1*s* line from the pyran oxygen compared to that of the nitro oxygen upon the ring-opening reaction of the molecules.

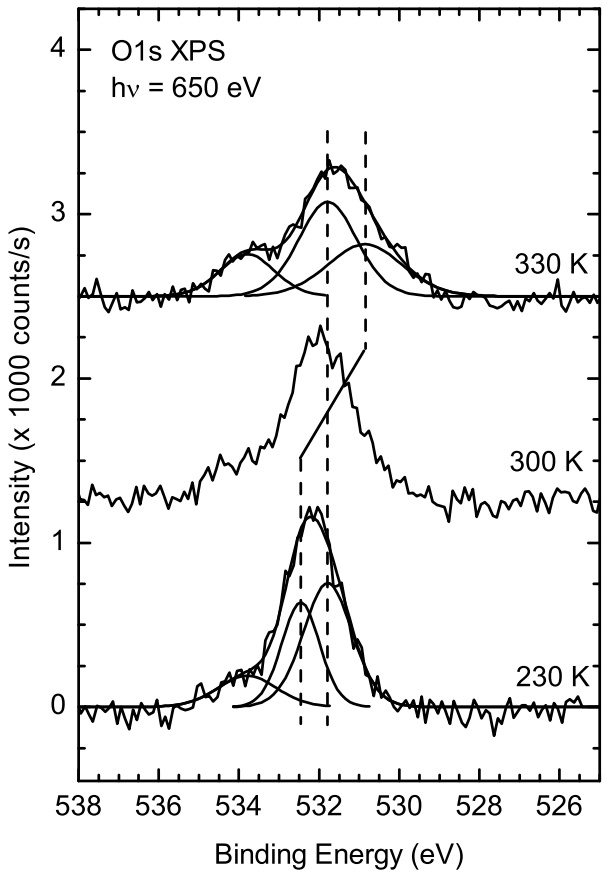

Figure 5.12: *X-ray photoelectron spectra of the O 1s level of ≈ 1 ML nitro-BIPS on Au(111), taken during the same heating sequence as the data presented in Fig. 5.11. From each spectrum, a linear background was subtracted. The spectra are shifted vertically for clarity.*

A shift of the indol N 1*s* XPS peak to higher binging energies was observed due to the SP→MC transformation (*cf.* Fig. 5.11). In fact, an opposite shift is observed in the temperature series of O 1*s* photoemission spectra, taken during the same heating sequence. This series of XPS spectra thus suggests that the transition corresponds to a temperature-induced SP→MC reaction taking place between 300 K and 330 K. The same phase transition was observed in **S**canning **T**unneling **M**icroscopy (**STM**) and **H**igh **R**esolution **E**lectron **E**nergy **L**oss **S**pectroscopy (**HREELS**) experiments [122].

Further evidence for the thermally induced ring-openig reaction comes from the N *K*-shell NEXAFS of the same annealing sequence of 1 ML nitro-BIPS on Au(111) shown in Fig. 5.13. For the spectra taken at temperature below 300 K, a strong π^* resonance is visible at 403.5 eV as the only spectral feature that was already assigned to the nitro N 1*s* → LUMO excitation. The same was found for the SP multilayer at 150 K except for the small resonance

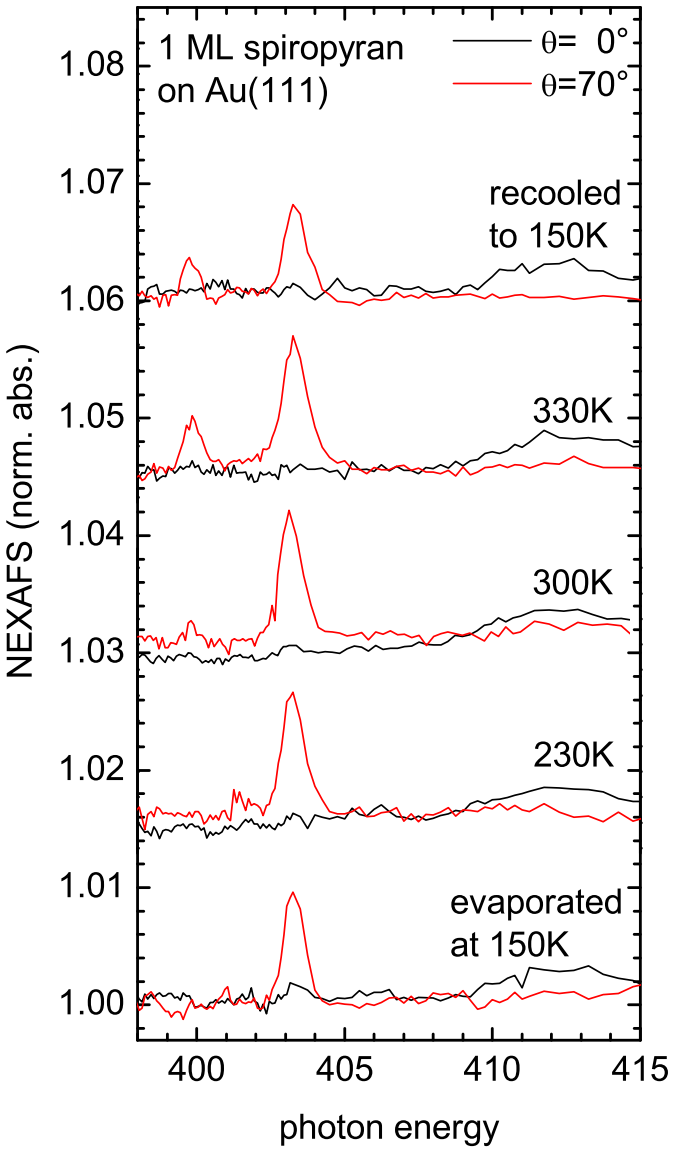

Figure 5.13: *a) N K edge absorption spectra of 1 ML spiropyran on Au(111), taken during a heating sequence from 230 K to 330 K (simultaneously to the data in Fig. 5.11 and 5.11). Continuous black (dashed red) lines correspond to spectra acquired at 90° normal (20° grazing) x-ray incidence. The spectra are shifted vertically for clarity.*

at 401.8 eV, which might be not recognized here due to the low signal-to-noise ratio. In contrast to the multilayer, a stronger angle dependence is visible such that the resonance at 403.5 eV is not present in any of the normal-incidence spectra. This attests that the nitro group is aligned parallel to the surface plane. Regarding the 3D structure of the SP isomer it indicates a rather strong non-covalent attractive interaction between the nitrobenzopyran and the metallic surface, which forces the former to lie flat on the surface.

Above 300 K the resonance assigned before to the indol N $1s \rightarrow$ LUMO+3 transition develops at 399 eV. The resonance of the nitro N $1s \rightarrow$LUMO excitation remains unaffected by the increasing temperature. Both facts agree with the ring-opening reaction that was also observed for the SP multilayer after UV irradiation. Both resonances are present exclusively in the grazing-incidence spectra, attesting that the produced MC isomer lies flat on the surface. The lack of resonances in both the experimental and simulated spectra at normal incidence proves that the π orbital system of merocyanine lies perpendicular to the surface and, consequently, all parts of the molecule lie flat and parallel to the metal surface, in agreement with the angular dependence of HREELS data that have been measured for the same system [122].

For T $\geq$ 300 K, a second π^* resonance appears at 400.3 eV. This resonance was also found in the measured spectrum of the multilayer sample after illumination and in the simulated spectrum of merocyanine. It was further found, that this feature can only be caused by the formation of an additional π bond to one of the nitrogen atoms. As already suggested by the XPS data, the indoline nitrogen site is expected to develop such a new intramolecular bond in the merocyanine zwitterion. This π bond is linked to the conjugated system of the nitrobenzene moiety, allowing electronic transitions from the indoline N 1s state into the extended π^* molecular orbitals. Thus, the two different π^* resonances seen in the experimental NEXAFS grazing spectrum at 330 K come from transitions from the two non-equivalent N1s excitation centers into the LUMO of the MC molecule. The subsequent cooling back to 150 K provokes no further changes.

5.4 Discussion

The good agreement of the data measured for the nitro-BIPS multilayer and that for the monolayer on Au(111) evidences that the ring-opening reaction has taken place in both systems. This is further supported by the DFT-based simulations of the N K-shell NEXAFS of the corresponding free SP and MC molecules. No covalent interaction is found neither between the molecules in

the crystalline phase nor to the surface.

In the multilayered film the MC form turned as the stable one after UV irradiation against thermal- and photoisomerization. No back reaction could be induced by visible light exposure. In the crystalline structure this irreversibility of the isomerization process might be caused by the steric hindrance that prevents a conformational back reaction of the unfolded merocyanine. Unfortunately, no reliable conclusion can be drawn from NEXAFS and XPS about the extent of these effects. A second mechanism that might constrain the back reaction originates from the formation of stable dimers. In this case, the attractive electrostatic interaction between two zwitterionic isomers could further stabilize the MC form against the *trans* → *cis* transformation.

In the monolayer on Au(111), the MC form is the thermally more stable isomer. It was shown by means of STM that the SP and MC molecules are arranged in islands at 150 K and in chains of dimers at 330 K on the Au(111) surface [122]. It was further found that the MC dimers are rather stable compounds whith a much higher binding energy than the one between dimers. Force field calculations of a free TTC-MC dimer in the determined adsorption geometry revealed that the strong intra-dimer interactions are mainly due to hydrogen bonds between the methylic hydrogen and the oxygen of the nitro groups.

Furthermore, DFT calculations were conducted on the MC dimer. The RPBE functional (*cf.* Sec. 3.2.3) used for the calculations was recently applied to describe hydrogen bonds [123]. The structure resulting from the force field calculations was used as a starting point for the geometry optimization. All nitrobenzene atoms rings had been constrained to the same plane. DFT yield hydrogen-bond lengths between 2.7 Å and 3.5 Å, differing between 5% and 10% from the values found by the force-field calculations. The calculated binding energy for the dimer is 0.109 eV per nitro group. This might be an underestimation, regarding that the used basis set is less diffusive than those normaly used for the description of hydrogen bonds. However, Mulliken population analysis reveals a trend of the charge redistribution in the MC molecule after dimer formation with a decrease of 10% in electron density at the nitro group. This enhances the electron accepting character of the nitro group and might lead to a further stabilization of the zwitterionic structure. This is an additional mechanism that may strengthen the intra-dimer interaction, and thus prevent the back reaction toward the SP as discussed in Sec. 5.1.

In addition, the metallic surface appropriately stabilizes the zwitterionic structure and the hydrogen bonds on the surface by the interaction of the molecular dipoles with an induced metallic image dipole. Beyond the attrac-

tive dipole-(induced)dipole interaction, this would inevitably lead to the stabilization of the central alkene bridge increasing the activation barrier for the back reaction. In order to reduce this stabilization of the zwitterionic form by the substrate, one could reduce the intrisic molecular dipole by suppressing the zwitterionic form. This could be achieved either by avoiding the attachment of donor and acceptor groups, as they are present in nitro-BIPS, or even more by attaching them in the opposite way, meaning nitro groups at the indol part and methylic groups at the benzopyran subsystem. Another strategy in this direction would involve the choice of different non-polar and non-metallic substrates. In this case, the stabilization by (induced) substrate dipoles would also be suppressed.

A different aspect that might be interesting concerns the reactivity of the ketonic oxygen at the ring-opened isomer. Since the Au(111) single crystal surface is inert against coordinative bond formation to organic adsorbates, no such interaction was consequently found in the present measurements after the ring-opening reaction. This might change when going to more reactive metallic surfaces. In the presence of the ketonic O=C double bond of the quinoid MC the orbitals of the lone-pair electrons are in plane with the molecular structure. Thus the MC molecule might be further forced to a perpendicular adsorption geometry in order to form a coordinative bond between the ketonic oxygen and the involved metallic surface atom[3]. On the one hand, this would reduce the image dipole formation. On the other hand, it would stabilize the MC form in another way that could give rise to an easier back reaction. Thus a more reactive surface could be another interesting starting point for further investigation.

[3]This is similar to the tilt of the benzonitrile that was observed for DMC on Cu(001) (*cf.* Sec. 4.3.2.5)

Conclusions

In this work, the adsorption of two types of molecular switches on noble metal surfaces was studied by means of XPS and angle-dependent NEXAFS measurement. By comparing the experimental results to DFT calculations, detailed information was obtained on the interaction between the molecular switches and their environment. These studies reveal that not only adsorbate-surface, but also intermolacular interactions can strongly influence the isomeric states on the surface.

Two azobenzene derivatives, dimetacyano and dimetacarboxymethylester azobenzene (DMC and CMA), representing a group of small conformal switches, have been investigated in different environments. The two compounds were chosen because they display the same adsorption behavior, while their different rest groups yield complementary information about the molecular state. In both cases, no evident differences are observed between the corresponding core level spectra for crystalline powder pressed on an In foil, for a deposited multilayer, and for mono- and submonolayers directly adsorbed on a Au(111) single crystal surface. Furthermore, all these data are very well reproduced by theoretical simulations of the gas-phase *trans* azobenzene. Therefore strong chemical and electronic interactions can be excluded in those condensed phases. As a consequence 1 ML (monolayer) azobenzene is physisorbed lying flat on the surface in the thermally more stable *trans* conformation on Au(111) at room temperature.

In contrast, for coverages below 0.4 ML of azobenzene on Cu(001), a mixture of physisorbed and chemisorbed species appears even at low substrate temperatures of 150 K. While annealing the sample, it is observed that at 250 K the majority of the physisorbed molecules are transformed to the chemisorbed state. The influences of the molecule–substrate and intermolecular interactions were separately studied by comparing the experimental NEXAFS data to a DFT simulation of a single azobenzene molecule on a Cu(001) cluster. The chemisorption of the azobenzenes is characterized by rehybridization of the central azo highest unoccupied molecular orbitals (HOMOs), and by the sub-

sequent σ bond formation between the azobenzene frontier orbitals and those of the Cu(001) substrate. As a result, the benzonitrile moieties are tilted out of the surface plane. In this conformation the lone-pair electrons can participate in the chemical binding, leading to a higher stabilization of the bent structure. The electronic reconfiguration of the adsorbate is well described in the picture of adsorbate-HOMO to substrate donation and substrate to adsorbate-LUMO back-donation, referred to as DCD (Dewar-Chatt-Duncanson) model. In this case the central azo π bond is weakened by the deoccupation of the bonding and the occupation of the antibonding orbital. Finally, it is concluded that the chemisorbed DMC molecules exhibit a strongly distorted geometry with an increased bond length of the azo N=N double bond due to the presence of the Cu(001) surface.

When increasing the coverage to 0.8 ML DMC on Cu(001), the intermolecular interactions provoke the phenylic moieties of the additionally adsorbed species to tilt further away from the surface plane. This effect is supported by the destabilization of the *trans* conformation by both the DCD donation–back-donation process, and the increasing interaction of the lone-pair electrons with the substrate. The bending leads to the dissociation of the additional azobenzene molecules at the azo center, so that the benzonitrile moieties are oriented almost perpendicular to the surface plane. The binding energy of the new adsorption state is about five times larger in binding energy than the one of the low-coverage species. A dependence of the dissociation process on the substitution groups of the different azobenzene derivatives was not observed. The coverage-dependent growth mode might open a new possibility of molecular structuring and self-assembling using molecular vapor deposition.

For azobenzenes, it can thus be concluded that the bistable character that originates from the stabilization of the central N=N double bond in *trans* and *cis* conformation is (at least partially) suppressed by the partial emptying and filling of the HOMOs and the LUMO, respectively. This is compensated by another bistability caused by the antagonistic interplay of atomic N $2p$ – Cu σ bond formation and the interaction of the lone-pair electrons with the substrate. Pathways to improve the switchability of azobenzenes on metallic substrates could include surfaces of specific reactivity, between the ones of gold and copper, that balance these opposing interactions. This could be realized, *e.g.*, by using Au clusters, since their reactivities can be tuned by their size [124].

The adsorption of nitro-BIPS, a ring-opening/ring-closing system, on Au(111) was also investigate. In this case, intermolecular interactions are found to dominate the influence on the isomerization state: nitro-BIPS evap-

orated on Au(111) at 150 K adsorbs in its ring-closed state with the nitro moieties flat on the surface. By means of XPS, the isomerization toward the ring-opened form was observed during annealing the sample to 330 K. The N *K*-shell NEXAFS data reveal that the resulting planar isomer lies flat on the surface. In a collaborative STM work it was observed that the ring-opened species arrange in stable dimers. The inter-dimer interaction is dominated by hydrogen bonds between the nitro oxygen and the methylic hydrogen. A subsequent DFT calculation of the dimer reveals the increase of the electron-accepting character of the nitro group induced by those hydrogen bonds. No reliable conclusion can be given about the influence of the surface on the interaction without including the substrate in the calculation.

However, Au(111) appears to be unsuitable to provoke a coordinative bond between the ketonic oxygen of the ring-opened isomer and the metallic substrate atoms. The switchability of the adsorbate-surface system could be improved in two ways. Firstly, the inter-dimer interactions can be partially prevented by omitting the nitro substitution, in order to suppress the corresponding hydrogen-bonds. Additionally, this might decrease the dipole moment of the zwitterionic structure in the ring-opened form. Secondly, a more reactive surface might provoke the chelation of the ring-opened isomer and lead to processes comparable to the metal-ion attachment/detachment in solution.

Bibliography

[1] Z. Guo, F. Zhou, J. Hao, and W. Liu, *Stable biomimetic super-hydrophobic engineering materials*, J. Am. Chem. Soc. **127**, 15670 (2005). 1

[2] Ltd. Hitachi, *Hitachi achieves nanotechnology milestone for quadrupling terabyte hard drive* (2009). 1

[3] Intel Corporation, *Intel Core2 Duo Mobile Processor T9900* (2007). 1

[4] J. Lahann, S. Mitragotri, T.-N. Tran, H. Kaido, J. Sundaram, I. S. Choi, S. Hoffer, G. A. Somorjai, and R. Langer, *A reversibly switching surface*, Science **299**, 371 (2003). 2

[5] H. S. Lim, D. Kwak J. T. Han, M. Jin, and K. Cho, *Photoreversibly switchable superhydrophobic surface with erasable and rewritable pattern*, J. Am. Chem. Soc. **128**, 14458 (2006). 2, 39

[6] M. Alemani, M. V. Peters, S. Hecht, K.-H. Rieder, F. Moresco, and L. Grill, *Electric field-induced isomerization of azobenzene by STM*, J. Am. Chem. Soc. **128**, 14446 (2006). 2, 3

[7] M. J. Comstock, N. Levy, A. Kirakosian, J. Cho, F. Lauterwasser, J. H. Harvey, D. A. Strubbe, J. M. J. Fréchet, D. Trauner, S. G. Louie, and M. F. Crommie, *Reversible photomechanical switching of individual engineered molecules at a metallic surface*, Phys. Rev. Lett. **99**, 038301 (2007). 3

[8] S. Hagen, F. Leyssner, D. Nandi, M. Wolf, and P. Tegeder, *Reversible switching of tetra-tert-butyl-azobenzene on a Au(111) surface induced by light and thermal activation*, Chem. Phys. Lett. **444**, 85 (2007).

[9] M. Alemani, S. Selvanathan, F. Ample, M. V. Peters, K.-H. Rieder, F. Moresco, Ch. Joachim, S. Hecht, and L. Grill, *Adsorption and switching properties of azobenzene derivatives on different noble metal surfaces: Au(111), Cu(111), and Au(100)*, J. Phys. Chem. **112**, 10509 (2008). 2, 3

[10] L. Bernard, M. Calame, S. J. van der Molen, J. Liao, and C. Schönenberger, *Controlled formation of metallic nanowires via Au nanoparticle AC trapping*, Nanotechnology **18**, 235202 (2007). 2

[11] T. Sakata, D. K. Jackson, S. Mao, and G. Marriott, *Optically switchable chelates: Optical control and sensing of metal ions*, J. Org. Chem. **73**, 227 (2008). 2, 4, 103

[12] J. Henzl, M. Mehlhorn, H. Gawronski, K.-H. Rieder, and K. Morgenstern, *Reversible cis-trans isomerization of a single azobenzene molecule*, Angew. Chem. Int. Ed. **45**, 603 (2006). 2, 3, 39, 40

[13] J. Henzl, T. Bredow, and K. Morgenstern, *Irreversible isomerization of the azobenzene derivate methyl orange on Au(111)*, Chem. Phys. Lett. **435**, 278 (2007). 2, 3, 40

[14] A. Langner, Y. Su, and M. Sokolowski, *Luminescence quenching of tetracenen films adsorbed on an ultrathin alumina (AlOx) layer on Ni_3Al (111)*, Phys. Rev. B **74**, 045428 (2006). 2

[15] N. Henningsen, R. Rurali, K. J. Franke, I. Fernández-Torrente, and J. I. Pascual, *Trans to cis isomerization of an azobenzene derivative on a Cu(100) surface*, Appl. Phys. A **93**, 241 (2008). 3, 40, 45, 98

[16] N. Henningsen, K. J. Franke, I. F. Torrente, G. Schulze, B. Priewisch, K. Rück-Braun, J. Dokic, T. Klamroth, P. Saalfrank, and J. I. Pascual, *Inducing the rotation of a single phenyl ring with tunneling electrons*, J. Phys. Chem. C **111**, 14843 (2007). 39

[17] T. Huang, Z. Hu, A. Zhao, H. Wang, B. Wang, J. Yang, and J. G. Hou, *Quasi chiral phase separation in a two-dimensional orientationally disordered system: 6-nitrospiropyran on Au(111)*, J. Am. Chem. Soc. **129**, 3857 (2007).

[18] N. Katsonis, T. Kudernac, M. Walko, S. J. van der Molen, B. J. van Wees, and B. L. Feringa, *Reversible conductance switching of single diarylethenes on a gold surface*, Adv. Mater. **18**, 1397 (2006). 3

[19] A. Einstein, *An effective heuristic algorithm for the travelling-salesman problem*, Ann. Phys. **17**, 132 (1905). 8

[20] K. Siegbahn, *ESCA Atomic, Molecular and Solid State Structure Studied by Means of Electron Spectroscopy*, Almqvist and Wiksells, Uppsala (1967). 10

[21] C. R. Brundle and A. D. Baker, *Electron spectroscopy: Theory, Techniques and Applications*, volume 1, Academic Press, London . New York . San Francisco (1977). 12

[22] W. Domcke, L. S. Cederbaum, J. Schirmer, and W. von Niessen, *Negative shake-up energy in core ionization*, Phys. Rev. Lett. **42**, 1237 (1979). 13

[23] WM. J. Veigele, *Photon cross sections from 0.1 keV to 1 MeV for elements Z = 1 to Z = 94*, Atomic Data Tables **5**, 51 (1973). 14

[24] D. R. Penn, *Electron mean-free-path calculations using a model dielectric function*, Phys. Rev. B **35**, 482 (1987). 15

[25] L. G. Parratt, *Electronic band structure of solids by X-ray spectroscopy*, Rev. Mod. Phys. **31**, 616 (1959). 18, 54

[26] H. Rabus, D. Arvanitis, M. Domke, and K. Baberschke, *High resolution X-ray absorption spectroscopy of linear hydrocarbons adsorbed on noble metal surfaces*, J. Chem. Phys. **96**, 1560 (1992). 18

[27] H. Rabus, D. Arvanitis, and K. Baberschke, *The π^* resonance and its vibrational broadening of unperturbed and adsorbed C_2H_4 molecules*, Surface Science **269-270**, 270 (1992). 18

[28] M. N. Piancastelli, D. W. Lindle, T. A. Ferrett, and D. A. Shirley, *Reply to the comment on the relationship between shape resonances and bond lengths*, J. Chem. Phys. **87**, 3255 (1987). 19

[29] O. Karis, A. Nilsson, M. Weinelt, T. Wiell, C. Puglia, N. Wassdahl, N. Mårtensson andM. Samant, and J. Stöhr, *One-step and two-step description of deexcitation processes in weakly interacting systems*, Phys. Rev. Lett. **76**, 1380 (1996). 19

[30] J. Stöhr, *NEXAFS*, Springer-Verlag, Berlin (1992). 19, 77

[31] M. Schmidbauer, A. L. D. Kilcoyne, H.-M. Koeppe, J. Feldhaus, and A. M. Bradshaw, *Strong multi-electron excitations in the C 1s photoionization of CO and CO_2*, Chem. Phys. Let. **199**, 119 (1992). 19

[32] M. S. Banna and D. A. Shirley, *Molecular photoelectron spectroscopy at 132.3 eV. The second-row hydrides*, J. Chem. Phys. **63**, 4759 (1975). 23

[33] H. Fellner-Feldegg, U. Gelius, B. Wannberg, A. G. Nilsson, E. Basilier, and K. Siegbahn, *New developments in ESCA-instrumentation*, J. Electr. Spectr. **5**, 643 (1974). 23

[34] W. Kohn and L. J. Sham, *Self-consistent equations including exchange and correlation effects*, Phys. Rev. **140**, A1133 (1965). 32

[35] J. P. Perdew, K. Burke, and M. Ernzerhof, *Generalized gradient approximation made simple*, Phys. Rev. Lett. **77**, 3865 (1996). 33

[36] B. Hammer, L. B. Hansen, and J. K. Nørskov, *Improved adsorption energetics within density-functional theory using revised Perdew-Burke-Ernzerhof functionals*, Phys. Rev. B **59**, 7413 (1999). 33

[37] C. C. J. Roothaan, *New developments in molecular orbital theory*, Rev. Mod. Phys. **23**, 69 (1951). 34

[38] N. Godbout, D. R. Salahub, J. Andzelm, and E. Wimmer, *Optimization of gaussian-type basis sets for local spin density functional calculations. part i. boron through neon, optimization technique and validation*, Can. J. Chem. **70**, 560 (1992). 35

[39] W. Kutzelnigg, U. Fleischer, and M. Schindler, *NMR-Basic Principles and Progress*, volume 23, Springer-Verlag, Heidelberg (1990). 35

[40] A. Mattsson, I. Panas, P. Siegbahn, U. Wahlgren, and H. Akeby, *Model studies of the chemisorption of hydrogen and oxygen on Cu(100)*, Phys. Rev. B **36**, 7389 (1987). 35

[41] H. Ågren, V. Carravetta, O. Vahtras, and L. G. M. Pettersson, *Direct SCF direct static-exchange calculations of electronic spectra*, Theor. Chem. Acc. **97**, 14 (1997). 35

[42] P. O. Loewdin, *Advances in Quantum Chemistry*, Academic, New York (1972). 36

[43] J. C. Slater and K. H. Johnson, *Self-consistent-field Xα cluster method for polyatomic molecules and solids*, Phys. Rev. B **5**, 844 (1972). 36

[44] K. Hermann, *Computational Methods in Catalysis and Material Science*, Wiley-VCH, Weinheim (2009). 37

[45] M. Leetmaa, M. Ljundberg, A. Nilsson, and L. G. M. Pettersson, *Computational Methods in Catalysis and Material Science*, Wiley-VCH, Weinheim (2009). 37

[46] M. Cavalleri, K. Hermann, S. Guimond, Y. Romanyshyn, H. Kuhlenbeck, , and H.-J. Freund, *X-ray spectroscopic fingerprints of reactive oxygen sites at the MoO_3(010) surface*, Catal. Today **124**, 21 (2007). 38, 67

[47] A. Kausar, H. Nagano, T. Ogata, T. Nonaka, and S. Kurihara, *Photocontrolled translational motion of a microscale solid object on azobenzene-doped liquid-crystalline films*, Angew. Chem. Int. Edit. **48**, 2144 (2009). 39

[48] O. Sadovski, A. A. Beharry, F. Zhang, and G. A. Woolley, *Spectral tuning of azobenzene photoswitches for biological applications*, Angew. Chem. Int Edit. **48**, 1484 (2009). 39

[49] I. A. Banerjee, L. Yu, and H. Matsui, *Application of host-guest chemistry in nanotube-based device fabrication*, J. Am. Chem. Soc. **125**, 9542 (2003). 39

[50] Y. Wang, X. Ge, G. Schull, R. Berndt, C. Bornholdt, F. Koehler, and R. Herges, *Azo supramolecules on Au(111) with controlled size and shape*, J. Am. Chem. Soc. **130**, 4218 (2008). 39

[51] Philipp Schmidt-Weber, *Functionalisation of Surfaces Funktionalisierung von Oberflächen Isomerisation and Chirality of Adsorbed Molecules Isomerisation und Chiralität adsorbierter Moleküle*, Ph.D. thesis, Frei Universität Berlin (2007). 39, 45

[52] Z. Lei, A. Vaidyalingam, and P. K. Dutta, *Photochemistry of azobenzene in microporous aluminophosphate $AlPO_4^{-5}$*, J. Phys. Chem. B **102**, 8557 (1998). 40

[53] E. R. Talaty and J. C. Fargo, *Thermal cis–trans-isomerization of substituted azobenzenes: a correction of the literature*, Chem. Commun. **2**, 65 (1967). 43

[54] Ch. R. Crecca and A. E. Roitberg, *Theoretical study of the isomerization mechanism of azobenzene and disubstituted azobenzene derivatives*, J. Phys. Chem. A **110**, 8188 (2006). 43, 44

[55] P. Bortolus and S. Monti, *Cis-trans photoisomerization of azobenzene. solvent and triplet donors effects*, J. Phys. Chem. **83**, 648 (1979). 44

[56] M. Kasha, *Characterization of electronic transitions in complex molecules*, Discuss. Faraday Soc. **9**, 14 (1950). 44

[57] I. Conti, M. Garavelli, and G. Orlandi, *The different photoisomerization efficiency of azobenzene in the lowest n π^* and $\pi\pi^*$ singlets: The role of a phantom state*, J. Am. Chem. Soc. **130**, 5216 (2008). 44, 45

[58] L. Wang, W. Xu, C. Yi, and X. Wang, *Isomerization and electronic relaxation of azobenzene after being excited to higher electronic states*, J. Mol. Graph. **27**, 792 (2009). 44

[59] H. Rau and E. Lueddecke, *On the rotation-inversion controversy on photoisomerization of azobenzenes. Experimental proof of inversion*, J. Am. Chem. Soc. **104**, 1616 (1982). 45

[60] E. Mitscherlich, *Über das Stickstoffbenzid*, Ann. Phys. Chem. **108**, 225 (1834). 45

[61] H. Jain, *Comparison of photoinduced atom displacements in glasses and polymers*, J. Optoelec. Adv. Mater. **5**, 5 (2003). 45

[62] H. Gojzewskia, A. Richterb, D. Wróbela, A. Apostolukc, P. Siejaka, and P. Raimond, *Growth of thin polymer films containing side-chain azo-dye analyzed by atomic force microscopy*, Surf. Sci. **603**, 237 (2009). 45

[63] S. Furumi, M. Kidowaki, M. Ogawa, Y. Nishiura, and K. Ichimura, *Surface-mediated photoalignment of discotic liquid crystals on azobenzene polymer films*, J. Phys. Chem. B **109**, 9245 (2005). 45

[64] P. Gore and O. H. Wheeler, *Absorption spectra of aromatic azo and related compounds. III. Substituted azobenzenes*, J. Org. Chem. **26**, 3295 (1961). 46

[65] B. Priewisch and K. Rück-Braun, *Efficient preparation of nitrosoarenes for the synthesis of azobenzenes*, J. Org. Chem. **70**, 2350 (2005). 46

[66] S. Rangan, J.-J. Gallet, F. Bournel, S. Kubsky, K. Le Guen, G. Dufour, F. Rochet, F. Sirotti, S. Carniato, and V. Ilakovac, *Adsorption of benzonitrile on Si(001) 2x1 at 300 K*, Phys. Rev. B **71**, 165318 (2005). 48, 52

[67] Y. Dimitrova, *Theoretical study of the changes in the electronic structure of benzonitrile accompanying its conversion into a radical anion*, J. Mol. Struc. (Theochem) **362**, 23 (1996). 53, 64

[68] H. Fliegl, A. Köhn, C. Hättig, and R. Ahlrichs, *Ab initio calculation of the vibrational and electronic spectra of trans- and cis-azobenzene*, J. Am. Chem. Soc. **125**, 9821 (2003). 53, 59

[69] S. Carniato, V. Ilakovac, J.-J. Gallet, E. Kukk, and Y. Luo, *Hybrid density-functional theory calculations of near-edge X-ray absorption fine-structure spectra: Applications on benzonitrile in gas phase*, Phys. Rev. A **71**, 022511 (2005). 54

[70] J. Stöhr, *NEXAFS*, Springer-Verlag, Berlin (1992). 54

[71] A. Konopacka and Z. Pawelka, *A theoretical and experimental study of the conformational behavior of methyl 3-nitrobenzoate in vacuum, in various solvents, and in solid state*, J. Mol. Struc. **844-845**, 250 (2007). 58

[72] N. Sundaraganesan and B. Dominic Joshua, *Vibrational spectra and fundamental structural assignments from HF and DFT calculations of methyl benzoate*, Spectrochim. Act. A **68**, 771 (2007). 59

[73] A. P. Hitchcock and S. G. Urquhart, *Inner-shell spectroscopy of benzaldehyde, terephthalaldehyde, ethyl benzoate, terephthaloyl chloride, and phosgene: Models for core excitation of poly (ethylene terephthalate)*, J. Phys. Chem. **96**, 8736 (1992). 59

[74] H. Ishii, K. Sugiyama, E. Ito, and K. Seki, *Energy level alignment and interfacial electronic structures at organic/metal and organic/organic interfaces*, Adv. Mater. **11**, 605 (1999). 64

[75] E. Kawabe, H. Yamane, R. Sumii, K. Koizumi, Yukio Ouchi, K. Seki, and K. Kanai, *A role of metal d-band in the interfacial electronic structure at organic/metal interface: PTCDA on Au, Ag and Cu*, Org. Elect. **9**, 783 (2008). 65

[76] T. Ohta, T. Fujikawa, and J. Kuroda, *Core-electron spectra of monosubstituted benzenes obtained by the gas-phase X-ray photoelectron spectroscopy*, Bull. Chem. Soc. Jpn. **48**, 2017 (1975). 65

[77] C. Kolczewski, F. J. Williams, R. L. Cropley, O. P. H. Vaughan, A. J. Urquhart, M. S. Tikhov, R. M. Lambert, and K. Hermann, *Adsorption geometry and core excitation spectra of three phenylpropene isomers on Cu(111)*, J. Chem. Phys. **125**, 034701 (2006). 67

[78] T. Kagiya, Y. Sumida, and T. Inoue, *A measure of the electron-donating power and electron-accepting power of liquid organic compounds*, Bull. Chem. Soc. Jpn. **41**, 767 (1968). 68

[79] D. Menzel, *Photoelectron spectroscopy of adsorption layers*, Critical, Reviews in Solid State and Materials Sciences **7**, 357 (1978). 75

[80] T. Nakayama, K. Inamura, Y. Inoue, and S. Ikeda, *Adsorption of benzonitrile and alkyl cyanides on evaporated nickel and palladium films studied by [xps .* 75

[81] O. Gunnarsson and K. Schönhammer, *Plasmon effects on core level spectra of adsorbates*, Sol. St. Comm. **26**, 147 (1978). 82

[82] A. M. Bradshaw, W. Domcke, and L. S. Cederbaum, *Intrinsic and extrinsic plasmon coupling in x-ray photoemission from core states of adsorbed atoms*, Phys. Rev. B **16**, 1480 (1997). 82

[83] M. J. S. Dewar, *A review of π complex theory*, Bull. Soc. Chim. Fr. **18**, C71 (1951). 88

[84] J. Chatt and L. A. Duncanson, *Olefin co-ordination compounds. Part III. Infra-red spectra and structure: attempted preparation of acetylene complexes*, J. Chem. Soc. 2939 (1953). 88

[85] B. Hammer and J. K. Norskov, *Why gold is the noblest of all the metals*, Nature **376**, 238 (1995). 89

[86] G. A. Burdick, *Energy band structure of copper*, Phys. Rev. **129**, 138 (1965). 89

[87] M. F. Budyka and M. M. Kantor, *Thermolysis of azobenzene*, Russ. Chem. Bull. **42**, 1495 (1993). 91

[88] J. T. Hoeft, M. Polcik, M. Kittel, R. Terborg, R. L. Toomes, J. H. Kang, and D. P. Woodruff, *Photoelectron diffraction structure determination of Cu(100)c(2x2)-N*, Surf. Sci. **492**, 1 (2001). 98

[89] T. Lederer, D. Arvanitis, M. Tischer, G. Comelli, L. Tröger, and K. Baberschke, *Structural determination of c(2x2)N/Cu(100): A multiple-scattering surface-EXAFS study*, Phys. Rev. B **48**, 11277 (1992).

[90] S. M. Driver and D. P. Woodruff, *Nitrogen adsorption structures on Cu(100) and the role of a symmetry-lowering surface reconstruction in the c(2x2)-N phase*, Surf. Sci. **492**, 11 (2001). 98

[91] R. Gleiter and W. Schaefer, *Interactions between nonconjugated π-systems*, Acc. Chem. Res. **23**, 369 (1990). 101

[92] V. I. Minkin, *Photo-, thermo-, solvato-, and electrochromic spiroheterocyclic compounds*, Chem. Rev. **104**, 2751 (2004). 101

[93] John B. Flannery Jr., *Photo- and thermochromic transients from substituted 1',3',3'-trimethylindolinobenzospiropyrans*, J. Am. Chem. Soc. **90**, 5660 (1968). 102, 106

[94] R. Kiesswetter, N. Pustet, F. Brandl, and A. Mannschreck, *1',3',3'-trimethyl-6-nitrospiro[2h-1-benzopyran-2,2'-indoline]: its thermal enantiomerization and the equilibration with its merocyanine*, Tetrahedron: Asymmetry **10**, 4677 (1999). 102, 106

[95] X. Guo, D. Zhang, G. Yu, M. Wan, J. Li, Y. Liu, and D. Zhu, *Reversible photoregulation of the electrical conductivity of spiropyran-doped polyaniline*

for information recording and nondestructive processing, Adv. Mater. **16**, 636 (2003). 103

[96] H. Görner and A. K. Chibisov, *Complexes of spiropyran-derived merocyanines with metal ions thermally activated and light-induced processes*, J. Chem. Soc., Faraday Trans. **94**, 2557 (1998). 103

[97] G. Jiang, Y. Song, X. Guo, D. Zhang, and D. Zhu, *Organic functional molecules towards information processing and high-density information storage*, Adv. Mater. **20**, 2888 (2008). 103

[98] D. C. Magria, Th. P. Vancea, and A. Prasanna de Silva, *From complexation to computation: Recent progress in molecular logic*, Inorg. Chim. Act. **360**, 751 (2006). 103

[99] Y. Sheng, J. Leszczynski, A. A. Garcia, R. Rosario, D. Gust, and J. Springer, *Comprehensive theoretical study of the conversion reactions of spiropyrans: Substituent and solvent effects*, J. Phys. Chem. B **108**, 16233 (2004). 103, 104

[100] H. Görner, *Photoprocesses in spiropyrans and their merocyanine isomers: Effects of temperature and viscosity*, Chem. Phys. **222**, 315 (1997). 104

[101] H. Görner, *Photochemical ring opening in nitrospiropyrans: triplet pathway and the role of singlet molecular oxygen*, Chem. Phys. Lett. **282**, 381 (1998).

[102] N. Tamai and H. Miyasaka, *Ultrafast dynamics of photochromic systems*, Chem. Rev. **100**, 1875 (2000). 104

[103] H. Görner, *Photochromism of nitrospiropyrans: effects of structure, solvent and temperature*, Phys. Chem. Chem. Phys. **3**, 416 (2001). 105, 106

[104] Y. Sueishi, M. Ohcho, and N. Nishimur, *Kinetic studies of solvent and pressure effects on thermochromic behavior of 6-nitrospiropyran*, Bull. Chem. Soc. Jpn. **58**, 2608 (1985). 106

[105] S. Giordani and F. M. Raymo, *A switch in a cage with a memory*, Org. Lett. **5**, 3559 (2003). 107

[106] K. Sugiyama, H. Nakano, and K. Ohga, *Preparation and characterization of photoresponsive poly(methyl methacrylate) microspheres bearing phosphorylcholine-analogous and spirooxazine moieties*, Macromol. Chem. Phys. **195**, 3915 (1994). 107

[107] S. Bénard and P. Yu, *New spiropyrans showing crystalline-state photochromism*, Adv. Mater **12**, 48 (1999). 107

[108] K. Amimoto and T. Kawato, *Photochromism of organic compounds in the crystal state*, J. Photochem. Photobiol. C-Photochem. Rev. **6**, 207 (2005). 107

[109] M. Suzuki, T. Asahi, and H. Masuhara, *Photochromic reaction of microcrystalline 6-nitroindolinospiropyran studied by femtosecond diffuse reflectance spectroscopy*, Mol. Cryst. Liq. Cryst. **345**, 51 (2000). 107

[110] T. Asahi, M. Suzuki, and H. Masuhara, *Cooperative photochemical reaction in molecular crystal induced by intense femtosecond laser excitation: Photochromism of spironaphthooxazine*, J. Phys. Chem. A **106**, 2335 (2002). 107

[111] M. Karcher, C. Rüdt, C. Elsässer, and P. Fumagalli, *Switching of nonfunctionalized spiropyran thin films on single crystalline MgO(100)*, J. Appl. Phys. **102**, 084904 (2007). 107, 109, 117

[112] J. C. Ashley, *Inelastic interactions of low energy electrons with organic solids: Simple formulae for mean free paths and stopping powers*, *IEEE* Trans. Nucl. Sci. **NS-24**, 1454 (1980). 108

[113] Y. Futami, M. L. S. Chin, S. Kudoh, M. Takayanagi, and M. Nakata, *Conformations of nitro-substituted spiropyran and merocyanine studied by low-temperature matrix-isolation infrared spectroscopy and density-functional-theory calculation*, Chem. Phys. Lett. **370**, 460 (2003). 109

[114] C. C. Turci, St. G. Urquhart, and A. P. Hitchcock, *Inner-shell excitation spectroscopy of aniline, nitrobenzene, and nitroanilines*, Can. J. Chem. **74**, 851 (1996). 111

[115] M. Delamar, J. Aubard, J.-L. Albert, and J.-E. Dubois, *XPS study of a benzooxazolinic spiropyran and a related permanent merocyanine*, J. El. Spec. Rel. Phen. **28**, 289 (1983). 115, 116

[116] H. Ågren, B. O. Roos, P. S. Bagus, U. Gelius, P.-Å. Malmquist, S. Svensson, R. Maripuu, and K. Siegbahn, *Multiple excitations and charge transfer in the ESCA N1s (NO_2) spectrum of paranitroaniline. A theoretical and experimental study*, J. Chem. Phys. **77**, 3893 (1982). 116

[117] M. M. Chehimi and M. Delamar, *X-ray photoelectron spectroscopy of merocyanine dyes: VI. Shake up satellites in the nitro N1s spectra of some nitromerocyanine dyes*, J. El. Spec. Rel. Phen. **46**, 427 (1988). 116

[118] K. Roodenko, M. Gensch, J. Rappich, K. Hinrichs, N. Esser, , and R. Hunger, *Time-resolved synchrotron xps monitoring of irradiation-induced nitrobenzene reduction for chemical lithography*, J. Phys. Chem. B **111**, 7541 (2007). 118

[119] M. Chehimi and M. Delamar, *X-ray photoelectron spectroscopy of merocyanine dyes: III. Structure of the O1s line in the merocyanine 540 dye*, J. El. Spec. Rel. Phen. **43**, 307 (1987).

[120] G. Distefano, M. Guerra, D. Jones, A. Modelli, and F. P. Colonna, *Experimental and theoretical study of intense shake-up structures in the XPS spectra of nitrobenzenes and nitrosobenzenes*, Chem. Phys. **52**, 389 (1980).

[121] A. Laforgue, T. Addou, and D. Bélanger, *Characterization of the deposition of organic molecules at the surface of gold by the electrochemical reduction of aryldiazonium cations*, Langmuir **21**, 6588 (2005). 118

[122] M. Piantek, G. Schulze, M. Koch, K. J. Franke, F. Leyssner, A. Krüger, C. Navío, J. Miguel, M Bernien, M. Wolf, W. Kuch, P. Tegeder, and J. I. Pascual, *Reversing the thermal stability of a molecular switch on a gold surface: Ring-opening reaction of nitrospiropyran*, J. Am. Chem. Soc. **131**, 12729 (2009). 119, 121, 122

[123] T. Bucko, J. Hafner, and L. Benco, *Adsorption and vibrational spectroscopy of co on mordenite: Ab initio density-functional study*, J. Phys. Chem. B **109**, 7245 (2005). 122

[124] T. V. W. Janssensa, B. S. Clausena, B. Hvolbækb, H. Falsigc, C. H. Christensenc, Th. Bligaardb, and J. K. Nørskov, *Insights into the reactivity of supported au nanoparticles: combining theory and experiments*, Top. Catal. **44**, 15 (2005). 126

List of Publications

2009

- M. Piantek, J. Miguel, A. Krüger, C. Navío, M. Bernien, D. K. Ball, K. Hermann, and W. Kuch, *Temperature, surface, and coverage-induced conformational changes of azobenzene derivatives on Cu(001)*, J. Phys. Chem. C, in press.

- M. Piantek, G. Schulze, M. Koch, K. Franke, F. Leyssner, A. Krüger, C. Navío, J. Miguel, M. Bernien, M. Wolf, W. Kuch, P. Tegeder, and J. I. Pascual, *Reversing the thermal stability of a molecular switch on a gold surface: ring-opening reaction of nitro-spiropyran*, J. Am. Chem. Soc. **131**, 12729.

- J. Miguel, J. Sánchez-Barriga, D. Bayer, J. Kurde, B. Heitkamp, M. Piantek, F. Kronast, M. Aeschlimann, H. A. Dürr, and W. Kuch, *Time-resolved magnetization dynamics of cross-tie domain walls in permalloy microstructures*, J. Phys.: Condens. Mater. **21**, 496001.

- J. Miguel, R. Abrudan, M. Bernien, M. Piantek, C. Tieg, J. Kirschner, and W. Kuch, *Magnetic domain coupling study in single-crystalline Fe/CoO bilayers*, J. Phys.: Condens. Mater. **21**, 185004.

- M. Bernien, J. Miguel, C. Weis, M. E. Ali, J. Kurde, B. Krumme, M. P. Panchmatia, B. Sanyal, M. Piantek, P. Srivastava, K. Baberschke, P. M. Oppeneer, O. Eriksson, W. Kuch, H. Wende, *Tailoring the nature of magnetic coupling of Fe-porphyrin molecules to ferromagnetic substrates.*, Phys. Rev. Lett. **102**, 047202.

2008

- M. Piantek, J. Miguel, M. Bernien, C. Navío, A. Krüger, B. Priewisch, K. Rück-Braun, and W. Kuch, *Adsorption of carboxymethylester-azobenzene on copper and gold single crystal surfaces*, Appl. Phys. A **93**, 261.

- Y. Luo, M. Piantek, J. Miguel, M. Bernien, W. Kuch, and R. Haag, *In-situ formation and detailed analysis of imine bonds for the construction of conjugated aromatic monolayers on Au(111)*, Appl. Phys. A **93**, 293.

- R. Abrudan, J. Miguel, M. Bernien, C. Tieg, M. Piantek, J. Kirschner, and W. Kuch, *Structural and magnetic properties of epitaxial Fe/CoO bilayers on Ag(001)*, Phys. Rev. B **77**, 014411.

2007

- M. Bernien, X. Xu, J. Miguel, M. Piantek, P. Eckhold, J. Luo, J. Kurde, W. Kuch, K. Baberschke, H. Wende, and P. Srivastava, *Fe-porphyrin monolayers on ferromagnetic substrates: Electronic structure and magnetic coupling strength*, Phys. Rev. B **76**, 214406.

- H. Wende, M. Bernien, J. Luo, C. Sorg, N. Ponpandian, J. Kurde, J. Miguel, M. Piantek, X. Xu, P. Eckhold, W. Kuch, K. Baberschke, P. M. Panchmatia, B. Sanyal, P. M. Oppeneer, and O. Eriksson, *Substrate-induced magnetic ordering and switching of iron porphyrin molecules*, Nature Mater. **6**, 516.

Acknowlegments

I want to thank Prof. Dr. Wolfgang Kuch for supervising this thesis. I am thankful for all the dicussions, scientific advices and for benefiting from his experience in experimental methodology. I deeply appreciated the freedom to apply my own ideas, to start collaborations, and to realize the first scientific ventures.

I would like to express my gratitude to Prof. Dr. Klaus Hermann for his guidance through the field of quantum-chemical simulations and his interest in my work. I really enjoyed the pleasantly inspiring discussions, and I am grateful for the shared knowledge and experience, not only in theoretical physics.

Furthermore, I would like to thank the people of AG Pascual, specially Gunnar Schulze, Dr. Nils Henningsen, Prof. Dr. Katharina Franke, and Prof. Dr. Nacho Pascual, for the intensive collaboration and the inexhaustible inspiration. The mutual interest was always a motivation to me.

My personal thank goes to Dr. Jorge Miguel. I enjoyed the exciting sessions of creative writing and for extending of my vocabulary, not only of English language. Special thanks also for moral support during the last years. Thank you, Jorge!

Matthias Bernien - the second petty officer. I am still amazed remembering the never-ending stream of ideas leaving his head. Fighting around, against, and with our experimental set-up was always a pleasure with him.

Alex Krüger and Dr. Cristina Navío are thankfully mentioned for the beamtimes we spent together.

Dr. Philipp Schmidt-Weber and Dr. Thorsten Kampen are gratefully thanked

for their start-up aid at the beamline and the thousands of tips helping us to get experienced at BESSY.

Of course, I would also like to thank all the participating people who helped to make this work to what it is:

Birgitt Zada and Dr. Willy Mahler for the beamline support,

Uwe Lipowsky, for the permanent critical view on technical issues,

the people from ZEDAT and and ZEDV, for the support in computation, and

the people from the workshop of the Institute of Experimental Physics.

Vor allem aber möchte ich meiner Frau Eva für ihre Geduld, ihr uneingeschränktes Verständnis und die aufgebrachte Unterstützung in den letzten drei entbehrungsvollen Jahren danken.